Synthetic Macro-Fibers for Mitigating Distresses in Thin Concrete Pavements

A THESIS

SUBMITTED TO THE FACULTY OF THE GRADUATE SCHOOL

OF THE UNIVERSITY OF MINNESOTA

BY

Souvik Roy

IN PARTIAL FULFILLMENT OF THE REQUIREMENTS

FOR THE DEGREE OF

MASTER OF SCIENCE

Dr. Manik Barman

July, 2021

Acknowledgements

I would like to acknowledge the endless support provided by my advisor, Dr. Manik Barman during the course of this thesis work. The amount of knowledge and suggestions conveyed by him in the last two years has been essential for this study.

I would also like to acknowledge the time and support extended by my committee members, Prof. Mihai Marasteanu, Dr. Michael Greminger and Dr. Somayeh Nassiri.

I highly appreciate the financial support provided by MnDOT for my research and coursework.

I would also like to thank Amarjeet Tiwari for his contribution and help in this research work. A special thanks to Dr. Heena Dhasmana and my friends Jared Munch, Corey Crick, Alieu Kamara, Giselle Irankunda, Austin Janson and Caitlin Graeber for their constant support.

Dedication

I would like to dedicate this thesis to my parents, Shyamal Kumar Roy and Krishna Roy for their constant love and support.

Abstract

Application of Fiber Reinforced Concrete (FRC) in constructing concrete pavement overlays and new concrete pavements is gaining more attention. However, there has been limited research on quantifying the performance benefits of fiber and its dosage in concrete pavements, specifically in thin concrete pavements. The present study focused on determining the influence of synthetic macro-fibers in keeping the joint performance high for a longer duration of pavement service life and in mitigating thin concrete pavement distresses such as transverse joint faulting and fatigue cracking. Field data was collected from fiber reinforced in-service test sections at the MnROAD test facility, located on I-94 westbound, 35 miles north-west of the twin cities metropolitan area, Minnesota. Field data included, falling weight deflectometer (FWD), environmental strain, transverse joint faulting, international roughness index (IRI), and crack survey data. It was found that joint performance was significantly affected by the inclusion of fibers. High fiber dosage resulted in greater LTE, lower differential displacement, and lower loaded-side displacement. A faulting prediction equation was proposed on the basis of faulting data and statistical relationships. A relationship was also established between the joint faulting and IRI. The distress data analysis indicated that fatigue cracking may not be the dominant distress of the thin fiber reinforced pavements, but the transverse joint faulting is.

Table of Contents

List of Tables

List of Figures

1. Introduction

1.1. General

Transportation agencies always seek innovations or improvements in pavement designs to economize the pavement structures. Thin (5 to 7 in. thick) and ultra-thin (<5 in. thick) concrete pavements are some of the potential innovative designs for the low traffic volume roads. These are usually constructed without dowel bars because of the thickness limitations and are sometimes reinforced with structural fibers to achieve enhanced post-crack and joint performance (Harrington et al. 2014). Incorporation of structural fibers has a positive impact in improving the performance of thin and ultra-thin concrete pavements (Roesler et. al 2008).

Previous studies (Roesler et al. 2008, Vandenbossche et al. 2013) have showed that structural fibers contribute to the post-crack performance of concrete. However, most of these studies were based on laboratory tests and without field validated pavement performance and distress data. The above-mentioned limitation is probably one of the reasons why the fibers' contribution in mitigating distresses is avoided in the present available mechanistic-empirical design procedures for the ultra-thin and thin concrete overlays.

The goal of the present study was to determine the contribution of structural synthetic fibers in the performance of thin concrete pavements. The study investigated the effect of fiber reinforcement on the distresses and joint performance of thin concrete pavements constructed at grade. Field data was collected from an existing fiber reinforced concrete test section at the Minnesota Road Research Facility (MnROAD). MnROAD, which is the property of the Minnesota Department of Transportation (MnDOT), is the largest cold climate pavement test section in the country. MnROAD has different types of pavement test sections on seven miles of the interstate highway on I-94 westbound near Otsego, northwest of the Twin Cities metropolitan area, Minnesota. The present study used the distress and performance data from Fiber Reinforced Concrete (FRC) test cells that were constructed in the year 2017 (referred to as 'test cells' in this thesis) as a part of the National Road Research Alliance (NRRA) funded long-term research study on fiber reinforced concrete. These test cells consisted of both ultra-thin and thin concrete pavements constructed on the granular base layer and thin concrete overlays constructed on an existing concrete pavement. A total of eight cells were constructed but fiber dosages were varied only in the thin (5-6 in. thick) concrete pavement cells, which

are Cell 506, 606, 706, and 806. This thesis thereby considered the data only from the aforementioned four cells. The synthetic macro-fiber, alternatively known as synthetic structural fiber, was used in these cells. These cells were also instrumented with various sensors to determine the structural responses under environmental and live traffic loads. The distress data, performance data, various sensor data, and several non-destructive test data collected from the test cells were analyzed in this thesis. An effort was made to identify and quantify the contribution of structural fibers in mitigating different common distresses in thin concrete pavements.

1.2. Objectives and Scope of the Study

In this thesis, the distresses and performance of the non-fiber and fiber-reinforced companion field sections were studied for three years from the date of construction. The specific objectives of the study are listed below.

1. To identify the contribution of synthetic macro-fibers in improving concrete pavement joint performance.

2. To quantify the benefits of synthetic macro-fibers in mitigating transverse joint faulting and to develop a faulting prediction equation for thin concrete pavements.

3. To identify the effect of fibers in limiting pavement surface roughness and to establish a relationship between pavement roughness and joint faulting for fiber-reinforced thin concrete pavements.

4. Studying the benefits of fiber reinforced concrete in mitigating fatigue cracks in thin pavements.

1.3. Thesis Organization

This thesis consists of six chapters. They are summarised as follows:

Chapter 1: Introduction, research objectives, and scope of the study.

Chapter 2: Literature review on thin concrete pavements and overlays, distresses in thin concrete pavements, concrete pavement roughness and joint performance, pavement sensors, macro-fiber reinforced concrete pavements and a summary of the literature review.

Chapter 3: MnDOT field section details, traffic details, sensor data analysis procedure, distress surveys and pavement responses, description of the overall research methodology.

Chapter 4: Representation and analysis of structural responses like joint performance, environmental strain and associated studies on sub-layer voids and pavement temperature-LTE (Load Transfer Efficiency) relationship.

Chapter 5: Representation of distress data (transverse joint faulting and fatigue cracking), identifying faulting predictor variables for MnROAD test cells and development of a faulting prediction equation, crack percentage vs. traffic data for the test cells.

Chapter 6: Conclusions and recommendations based on the findings from this work and identifying the future work prospects.

2. Literature Review

This chapter consists of different literatures reviewed during the course of this thesis work. In the beginning, a brief background is provided about various concrete pavement classification, thin and ultra-thin concrete pavement overlays. Next, various load related distresses on such pavements are described in accordance to the present federal and state standards. After that, pavement roughness measurement and concrete pavement joint performance studies are discussed. Recent development in the field of pavement instrumentation and analysis procedure of different pavement sensor data is then presented. At last, the application of macro-fibers and relevant design procedure for fiber reinforced concrete pavements are discussed. A summary of the literature review is provided at the end of the chapter. An effort has been made to emphasize on the specific literature studies that are relevant to the objectives of this study. Furthermore, several other previous studies have been cited in this thesis in different chapters at relevant places and not included in this chapter to avoid repetition.

2.1. Concrete Pavements and Overlays

Conventional jointed plain concrete pavements (JPCP) are constructed with 7 to 14 in. thick slabs, depending on the level of traffic, environmental conditions, and supporting layers (AASHTO 1993, Cervantes and Roesler 2009). The ultra-thin and thin pavements are 3 to 7 in. thick and are intended for low-volume roads. The popularity of the use of fibers in ultra-thin and thin concrete overlays invoked the interest in constructing the new pavements with FRC as well. MnDOT constructed such pavements at the MnROAD test facility as part of the experimental study (Deusen et al., 2018) to identify the possibility of large-scale construction of such pavements for low-volume roads. The concrete overlays are constructed either on the old asphalt layer or on the old cement concrete pavement. Concrete overlays without any bonding at the interface are known as Unbonded Concrete Overlay (UBOL) (Smith et al. 2002). Unbonded concrete overlays are usually 5 in. or more in thickness, while the bonded overlays can be as thin as 3 in. Bonded overlays on asphalt are known as Whitetopping or Bonded Concrete Overlay of Asphalt (BCOA). Figure 2-1 shows a descriptive image of each of the above-mentioned concrete pavement types.

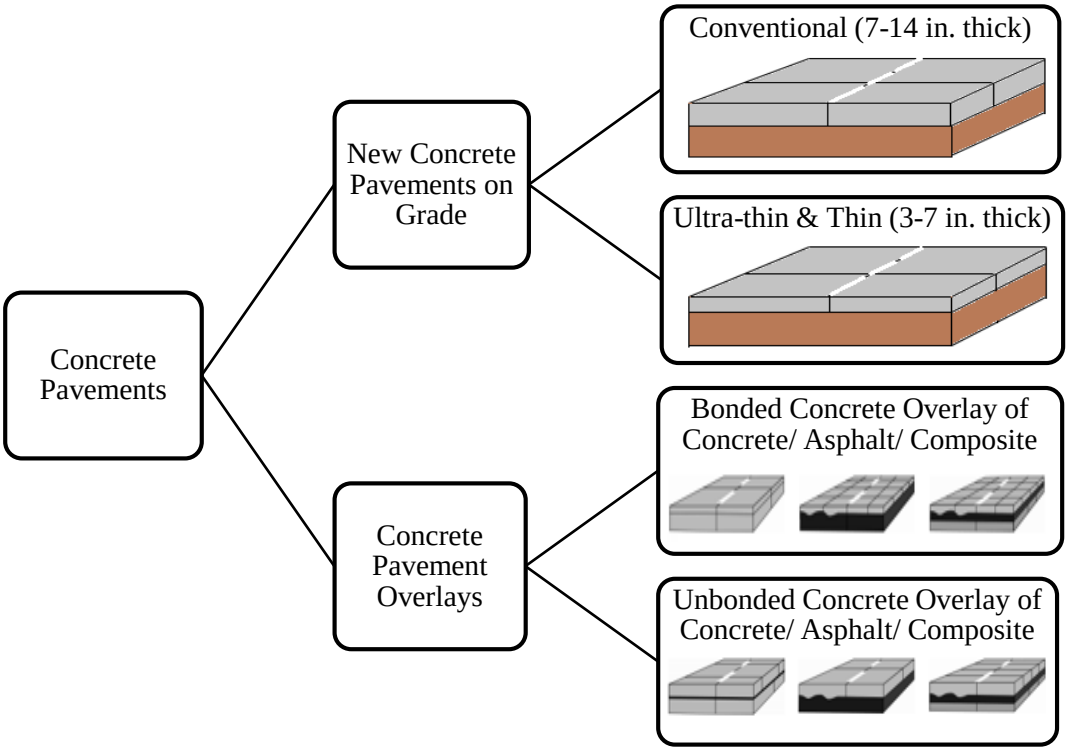

Figure 2-1: Types of concrete pavements (Overlays image courtesy: Harrington, 2008).

The present study is based on thin concrete pavements constructed on unbonded base layer at the MnROAD test facility. Though these cells were exposed to interstate traffic, the cells were designed for low volume traffic. Thus this study can be considered as an accelerated load study.

2.2. Distresses in Concrete Pavements and Overlays

According to Federal Highway Administration (FHWA) distress identification manual (Miller & Bellinger, 2003) and MnDOT pavement distress identification manual (2011), the major distresses identified in Jointed Plain Concrete Pavements (JPCP) are transverse joint faulting, panel fatigue cracking (transverse cracks), durability or D-cracking, and transverse or longitudinal joint spalling. The joint faulting and fatigue cracks are structural distresses and are dependent on the pavement design, traffic, and environmental loads and thus considered in the mechanistic-empirical design of the concrete pavements.

2.2.1. Joint Faulting

Transverse joint faulting is defined as the difference in elevation between two adjacent concrete pavement slabs. Repeated heavy axle loads crossing transverse joints create the potential for joint faulting. Excessive deflections at slab edge and corner that cause erosion and pumping of fines from beneath the leave slab result in faulting. Eroded fines then deposit under the approach slab. The rate of progression of transverse joint faulting increases significantly when a pavement exhibits a combination of poor load transfer across the transverse joints or cracks, heavy axle loads, free moisture beneath the pavement, and erosion and pumping of the supporting base, subbase, or subgrade material from underneath the slab or treated base (Khazanovich et al. 2004).

A difference of 0.04 in. (1 mm) and higher in elevation across a transverse joint is considered as notable joint faulting, and anything less than that is surface roughness and is usually not considered for faulting calculation. Figure 2-2 shows how MnDOT measures transverse joint faulting.

Figure 2-2: Transverse joint faulting in concrete pavements (MnDOT, 2011).

Generally, in the case of joint faulting, the approach slab of a concrete pavement goes up, and the leave slab settles down. But sometimes, the leave slab remains at a higher elevation from the approach slab. This is known as negative faulting (as shown in Figure 2-3). While the negative faulting is usually minimal and avoided, Tsai & Wu (2019) considered negative faulting values in addition to positive faulting to compute a parameter known as Faulting

Index (FI). Faulting index is a measure to represent the average faulting in a concrete pavement. According to Tsai & Wu (2019), negative faulting is rare, but it can cause serious safety issues in concrete pavements and thus, it should not be ignored entirely while analyzing joint faulting.

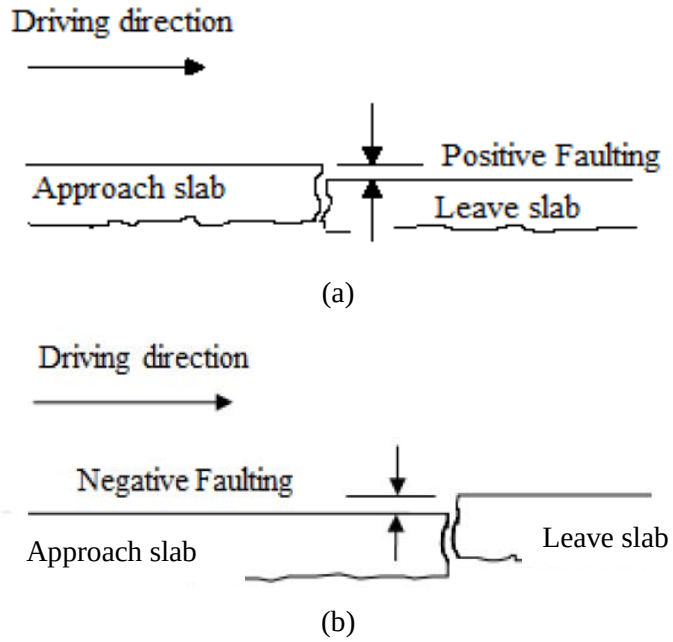

Figure 2-3: (a) Conventional or positive joint faulting (b) Negative joint faulting (Negative faulting image courtesy: Tsai et al. 2016).

2.2.2. Fatigue Cracking

Fatigue cracking of concrete pavement results from repeated application of traffic and environmental loads. In the conventional JPCP, the fatigue cracks are usually mid-slab transverse cracks. Figure 2-4 shows concrete pavement slab cracking as represented in MnDOT's pavement distress identification manual (2011). Both traffic and environmental induced stresses and the location of the critical stresses are important to determine the exact reason of cracking (Khazanovich & Yu, 2001). A cracked panel is identified with one or more cracks greater than or equal to 2 feet (0.6 m) in length (MnDOT, 2011).

Figure 2-4: Concrete Pavement Slab Cracking (MnDOT, 2011).

The above-mentioned distresses also occur in thin and ultra-thin concrete pavements and overlays; however, the fatigue crack is not always the mid-slab transverse crack. Additionally, corner cracks, slab migration, and slab shattering (in ultra-thin concrete pavements) can occur as well in such pavements (Vandenbossche and Barman 2010, Barman et al. 2018 and 2021).

2.2.3. Other Distresses

Concrete pavements may also experience distresses due to freeze and thaw cycles, scaling due to de-icing salts, or subgrade pumping (Delatte 2008). Reflective cracking may be observed in UBOL if the interlayer (separating layer of asphalt or nonwoven geotextile between overlay and existing concrete slab) does not provide sufficient separation between the overlay and the existing concrete layer (Sachs et al. 2016). Vandenbossche and Barman (2010) also stated that reflective transverse cracks occur in whitetoppings when the stiffness of the concrete layer is low relative to the stiffness of the asphalt layer.

2.3. Joint Faulting Models

The present study developed a faulting prediction equation. Therefore relevant literature on the transverse joint fauilting was reviewed and included in this chapter. The present mechanistic-empirical design guide for JPCP (NCHRP, 2003) documents all the existing joint

faulting predicting models accepted and practiced over the past two decades. Table 2-1 shows the transverse joint faulting models and the significant faulting predictor variables considered in these models. Equivalent standard axle loads (ESALs), PCC slab thickness, modulus of subgrade reaction, and transverse joint spacing are some of the variables, which were included in almost all these models. Hence, it can be stated that these variables need to be studied to develop any future faulting predicting equations.

Table 2-1: Variables considered in joint faulting models in different studies (NCHRP, 2003).

Variable	**SHRP P-020 (1984)**	**RPPR (1997)**	**ACPA (1994)**	**NAPCOM (1997)**	**LTPP Data Analysis (1997)**	**PaveSpec 3.0 (2000)**
Age	X	X				
80-kN (18-kip) ESALs	X	X			X	X
Axle load repetitions			X	X		
Drainage type	X	X				X
AASHTO drainage coefficient, C_d		X		X	X	
PCC slab thickness		X	X	X	X	X
PCC modulus of elasticity		X		X	X	X
Modulus of subgrade reaction (k-value)	X	X	X	X	X	X
Base type		X		X	X	X
Shoulder type	X	X		X	X	X
Transverse joint spacing	X	X	X	X	X	X

Variable	SHRP P-020 (1984)	RPPR (1997)	ACPA (1994)	NAPCOM (1997)	LTPP Data Analysis (1997)	PaveSpec 3.0 (2000)
Dowel diameter	X	X			X	X

2.4. Pavement Roughness

Distresses in concrete pavements reduce pavement performance and increases rider discomfort. International Roughness Index (IRI) is a widely accepted measure to represent pavement roughness (Janisch, 2015). The IRI simulates the total anticipated vertical movement of a standard vehicle accumulated over the length of the section. The IRI is typically reported in units of in./mile i.e., vertical inches of movement per mile traveled. MnDOT rates the pavement using a parameter called riding quality index (RQI), which has a range of 0.0 to 5.0, with 0.0 being very poor ride quality and 5 being very good. Janisch in his study developed a relationship between RQI and IRI. The following Equation 1 was proposed by Janisch (2015) to convert RQI to IRI for concrete pavements.

$$RQI = 6.634 - (0.353) * (\sqrt{IRI}) \qquad \text{(Equation 1)}$$

2.5. Joint Performance

The joint load transfer efficiency (LTE) is a common measure of joint performance, and it is the ratio of the slab deflections at the unloaded side and the loaded side and is expressed as a percentage. Figure 2-5 gives an idea about concrete pavement joint load transfer efficiency. A poor load transfer leads to higher deflection for the loaded slab and negligible deflection in the unloaded slab, as shown in Figure 2-5 (a). Figure 2-5 (b) shows that better load transfer is achieved when the loaded and unloaded slab deflects at almost same magnitude.

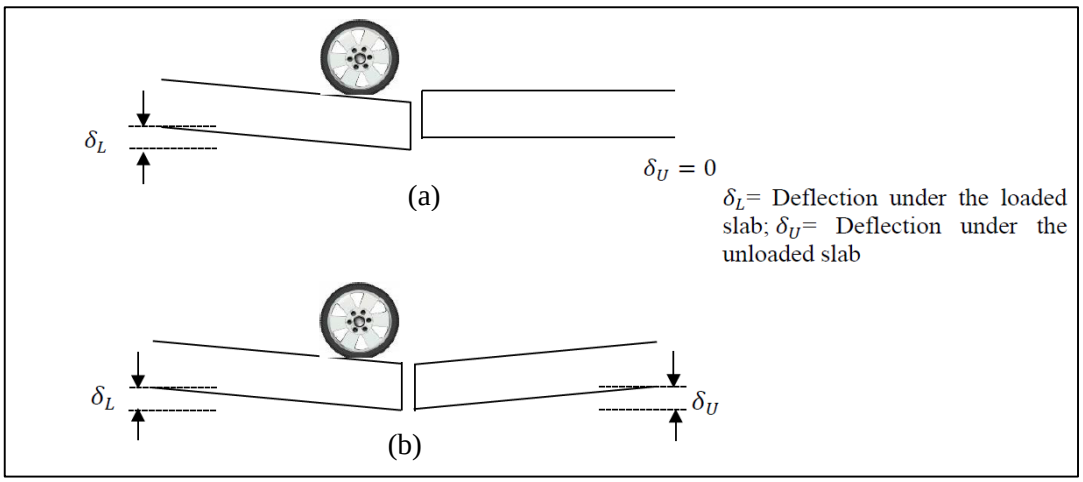

Figure 2-5: Schematic diagram explaining (a) poor LTE (b) high LTE (Barman, 2014).

Better joint performance means better load transfer between two adjacent concrete pavement slabs. LTE values above 70% are considered good, 50% to 70% - fair, and below 50% are poor (Papagiannakis and Masad, 2008). Colley and Humphrey (1967) observed that load transfer is developed either by interlocking action of the aggregate particles (aggregate interlock) at the faces of the joint or by a combination of aggregate interlock and mechanical devices like dowel bars. The Falling Weight Deflectometer (FWD) test is a well-known field test to investigate load transfer efficiency between two adjacent concrete pavement slabs. Vandenbossche (2007) evaluated field load transfer by FWD test in her study. It was observed that the LTEs measured for the doweled slabs were not affected by slab temperature gradient. However, LTEs measured for the unrestrained slabs were greatly affected by the presence of a temperature gradient. This study also showed that temperature gradients affect the interpretation of FWD data for rigid pavements when joint performance is evaluated and voids are detected.

The presence of voids underneath concrete pavement slabs play a significant role in joint load transfer. Ideally, more voids result in a poor joint performance. Crovetti and Darter (1985) proposed a method to investigate the presence of voids underneath concrete pavement slabs using FWD test results. As shown in Figure 2-6, FWD-measured corner deflections were plotted against the applied loads in this procedure. In such a plot, if the intercept of a deflection line (at zero load) is two mils or below, it is assumed that the chance of voids underneath the pavement slab is low.

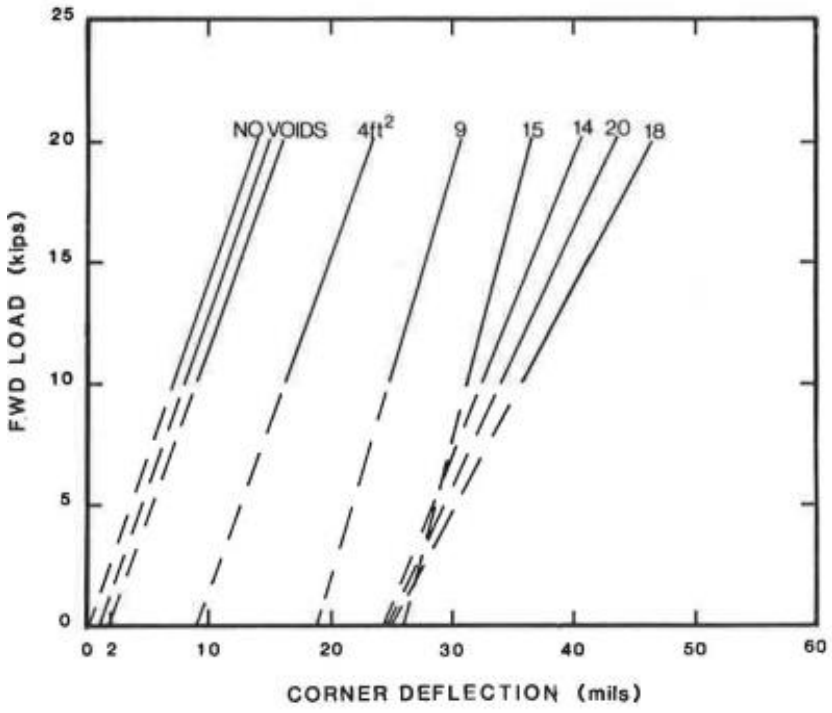

Figure 2-6: Use of FWD test data conducted at different load level to identify possible presence of voids (Crovetti and Darter, 1985).

2.6. Pavement Response Measurement

Previous research studies showed that pavement sensors/instrumentation could monitor different pavement responses upon loading (Weinmann et al. 2004, Vandenbossche et al. 2012). Sensors are installed in pavement while construction and are used to measure environmental strain, dynamic strain, deflections, temperature, etc. Wells et al. (2006) studied the built-in construction gradient and early-age slab deterioration in an instrumented test section constructed on S.R.-22 in Murrysville, Pennsylvania. For an example, Figure 2-7 shows the sensor plan of the studied test section.

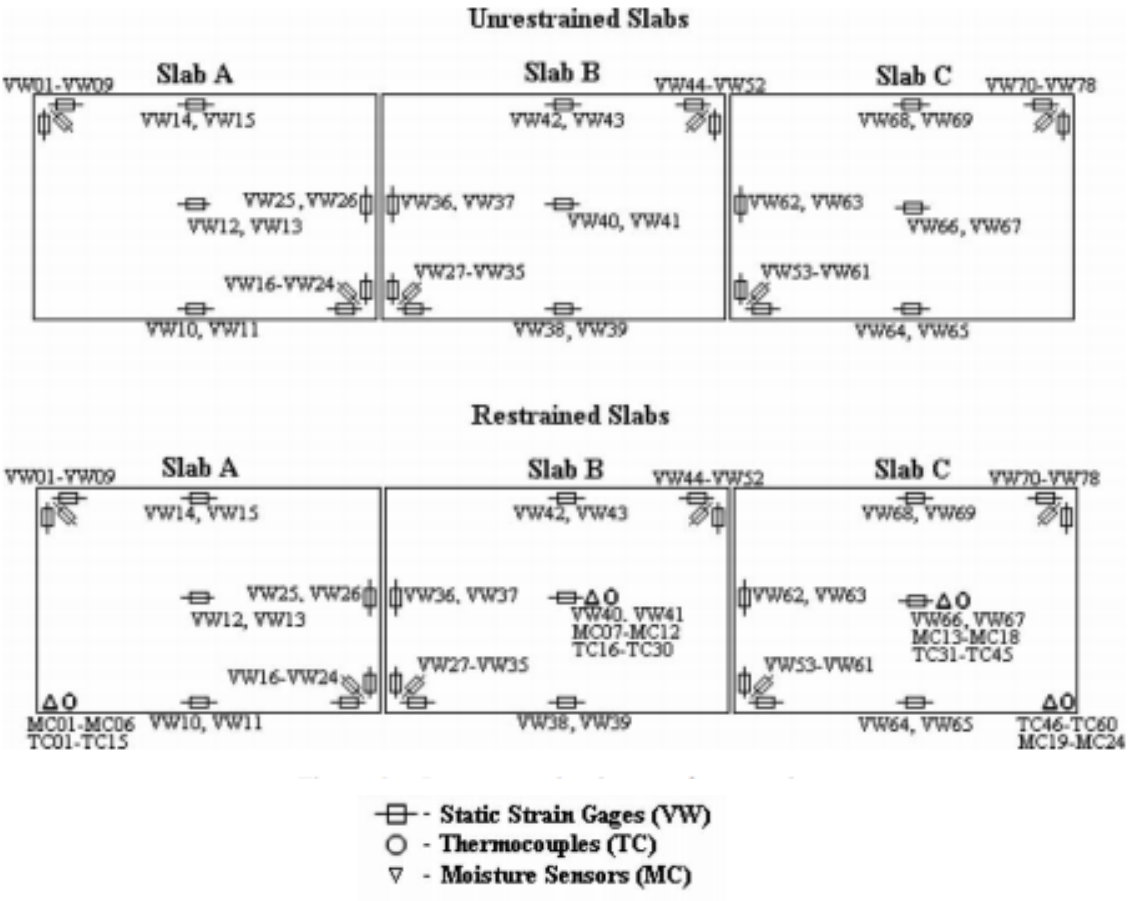

Figure 2-7: Instrumentation layout of test section in Murrysville, Pennsylvania (Wells et al. 2006).

The Minnesota Department of Transportation (MnDOT) started instrumenting their experimental accelerated pavement test section, MnROAD, between the years 1997-2007. Vibrating Wire (VW) strain sensors were installed in this phase which revealed the daily and seasonal expansion and contraction behavior of concrete pavement slabs (Burnham et al. 2020). VW sensors are made of a pre-tensioned wire which is within a protective steel tube with the wire anchored at flanges on either end of the steel tube. A resin encapsulated electro-mechanical exciter/reader is also externally attached to the steel tube. With the expansion and contraction of the concrete slab, under the effect of temperature change, the tension in the wire also changes. As a result, the frequency that the wire vibrates at is also changed. (Deusen et al., 2018).

Asbahan & Vandenbossche (2011) studied the effects of temperature and moisture gradients on slab deformation using VW strain gauge data. The difference in the strain values at the top

and bottom VW sensors of the slabs were used to calculate slab curvature using the following equation:

$$\rho = - \frac{\varepsilon_t - \varepsilon_b}{D(1 + \varepsilon_t + \varepsilon_b)} \qquad \text{(Equation 2)}$$

Where,

ρ = slab curvature (positive values indicate upward curvature) in units 1/m.

ε_t = strain measured by the top sensor of the slab at the time of interest.

ε_b = strain measured by the bottom sensor of the slab at the time of interest.

D = Distance between the top and bottom of the slab where strain is calculated in m.

2.7. Macro/Structural Fibers in Concrete Pavements

The first commercial steel fiber reinforced concrete pavement was constructed in the August of 1971 at Ashland, Ohio, but research on steel fiber reinforced concrete initiated back in the 1950s (ACPA, 2003). Steel fibers and synthetic fibers have been the two primary types of fibers used in concrete pavements initially. However, as research progressed, steel/synthetic fiber blends (ACPA 2003) were also experimented in concrete pavements. Although, steel fibers are known to increase the residual strength and ductility of concrete, they can decrease the workability when used in increased volume (Birley et al., 2018).

Synthetic fibers can be broadly classified into two major categories: macro or structural fibers and micro or non-structural fibers (Barman and Hansen, 2018). Macro fibers have load-bearing capacity. As this study deals with only macro fibers, the emphasis is only given to these fibers; also, 'fiber' in this study is referred to as the 'macro fiber.' Figure 2-8 shows a picture of a macro-fiber used in MnROAD Cells 94 and 95 (Barman, 2014).

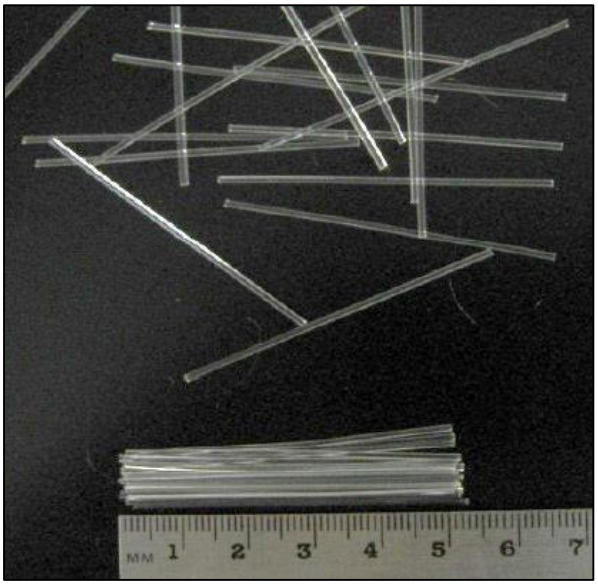

Figure 2-8: Macro Fibers (Barman, 2014).

There is no field-validated correlation between the fiber property and fatigue life of thin concrete pavements. The majority of researchers found that the inclusion of fibers may benefit the fatigue performance of concrete. However, the quantitative nature of this benefit is yet to be determined accurately (Lee and Barr, 2003). Earlier numerical analysis results indicated that FRC increases the fracture energy and residual load capacity of concrete pavements (Evangelista et al., 2009). Unlike Plain Cement Concrete (PCC), macro fiber reinforced concrete has post-crack performance (ACI 544.1R, 2009) and improved load transfer efficiency (LTE) (Barman, 2014; Barman et al., 2018; Roesler et al., 2019). Figure 2-9 shows the distinctly different responses of PCC and FRC under flexural load. It can be observed that the PCC undergoes brittle failure; whereas, the FRC offers post-crack performance, which may lead to prolonged fatigue life and reduced maintenance cost when used in pavements.

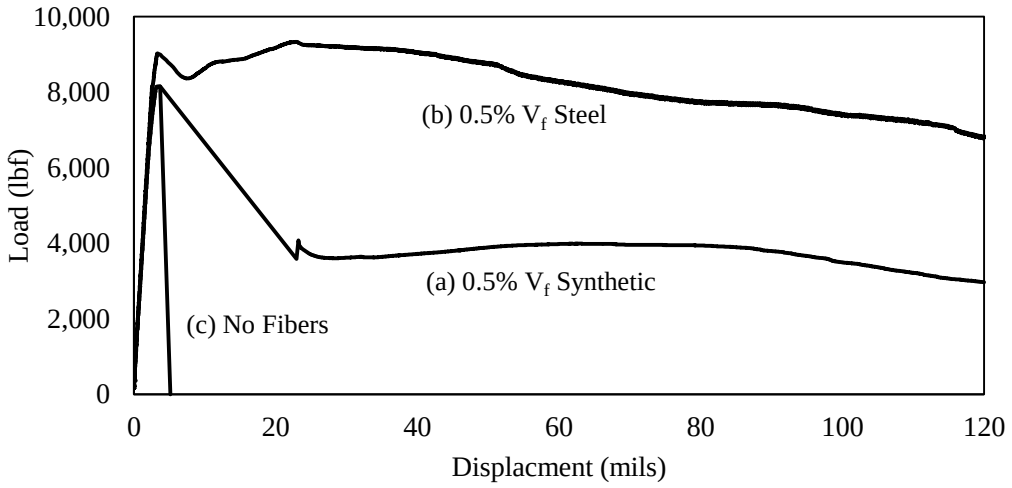

Figure 2-9: Load vs. Displacement curves for PCC and FRC (Barman and Hansen, 2018).

The inclusion of macro fibers in concrete pavements has been accounted for in a couple of previously available design procedures. Roesler et al. (2008) incorporated the contribution of fibers in the Illinois Center for Transportation (ICT) ultra-thin whitetopping design procedure. Extensive laboratory tests were conducted to quantify the benefits of applying fibers in ultra-thin concrete pavement overlays. Different fiber types (straight synthetic, crimped synthetic, two hooked end steel, and two crimped steel fibers) and fiber dosages (0.19 to 1.56 percent by volume) were considered in that study for a given level of performance (equivalent flexural strength and roughness). The Residual Strength Ratio, RSR (R_{150}^{150}) was proposed to characterize the performance of FRC in any concrete mixture used for ultra-thin whitetopping designs. R_{150}^{150} was computed as the ratio of the post-peak flexural strength of the FRC mixture (determined by ASTM C1609 test) at a net deflection of 0.12 in. (3 mm) to the concrete Modulus of Rupture (MOR). In the ICT design procedure, the residual strength (RS) of the FRC mixture is added to the MOR to account for the contribution of the fibers. Vandenbossche et al. (2013) later adopted the same procedure for accounting for the fibers' contribution in the BCOA-ME design procedure. BCOA-ME procedure was developed at the University of Pittsburgh through a pooled fund study that is recently used by many transportation agencies for designing thin and ultra-thin BCOAs.

2.8. Summary

Concrete pavements may be constructed newly or on any existing pavement surface (overlays). The common distresses in such pavements are joint faulting, fatigue cracking, etc. Such distresses are responsible for the pavement roughness, which can be represented in terms of International Roughness Index (IRI). Concrete pavement transverse joints are responsible for transferring loads from one slab to another. Joint load transfer efficiency is a good measure of the joint performance of concrete pavements. FWD test is a good tool to measure joint performance. Recently, various instrumentations are used for monitoring structural responses of the concrete pavement. Such pavement sensors can measure field strains and various other structural responses of the concrete pavements.

Thin and ultra-thin concrete pavements are often reinforced with structural fibers to reduce pavement distresses like transverse joint faulting, fatigue cracking, slab migration, etc. However, because of the lack of companion field sections and field-validated performance difference between the PCC and FRC pavements/overlays, it is difficult to quantify the benefits of fibers and to estimate how much more life can be achieved from the thin and ultra-thin pavements/overlays when reinforced with macro fibers. Two design procedures are presently available, which consider the inclusion of fiber reinforcement in thin and ultra-thin concrete overlays. They are ICT ultra-thin whitetopping design procedure and BCOA-ME design procedure. Both designs indirectly consider the benefits of fiber reinforcement by artificially increasing the MOR of concrete. But the MOR does not actually increase with the addition of the most commonly used synthetic fibers in the concrete mix. A more scientific approach to design such fiber-reinforced thin or ultra-thin concrete pavements will be by quantifying and considering the contribution of fibers directly in terms of mitigating pavement distresses, such as joint faulting, fatigue cracking, or improving the road performance like International Roughness Index (IRI) values. Field study with live traffic is necessary to account for the contribution of fibers to develop a mechanistic-empirical design procedure for fiber-reinforced thin concrete pavements and overlays.

3. Research Methodology and Data Collection

This chapter outlines the overall research methodology adopted in this thesis work, including a discussion on the test cells and their properties and design. Next, the traffic load details for the test cells are provided. Following that, the instrumentation of the field section relevant to this thesis is discussed, and the sensor data analysis procedure is illustrated. Finally, joint performance, joint faulting, and fatigue cracking data collection and analysis procedures are described.

3.1. Description of the Test Cells

The Minnesota Department of Transportation (MnDOT) constructed seven fiber reinforced concrete (FRC) test cells (Cell 139, 239, 705, 805, 506, 606, 706, and 806) and one Plain Cement Concrete (PCC) control cell (Cell 506) in the year 2017 at the MnROAD test facility. As mentioned earlier, the scope of this thesis only included the thin concrete test cells, which were Cells 506, 606, 706, and 806. Figure 3-1 (a) identifies the location of MnROAD and (b) shows an aerial view of the MnROAD test facility. The locations of the test Cells 506-806 and Cells 705 and 805 (beyond the scope of this thesis work) at the high volume section of the MnROAD test facility are shown in Figure 3-2. Table 3-1 presents a summary of the designs and materials used in these test cells. Cells 506 through 806 were constructed as thin concrete pavement on an 11 in. thick MnDOT class 5Q un-stabilized gravel base. All the four test cells were designed as 6 ft. x 6 ft. plan dimension and 5 in. thickness. However, Cell 606 was 6 in. thick due to a construction error. The test cells mainly varied in fiber content (0% to 0.75% by volume fraction).

(a)

(b)

Figure 3-1: (a) Location of MnROAD test facility on Google Map (b) Aerial photographic view of MnROAD test cells (Courtesy: Joy Powell, EQW, 2018).

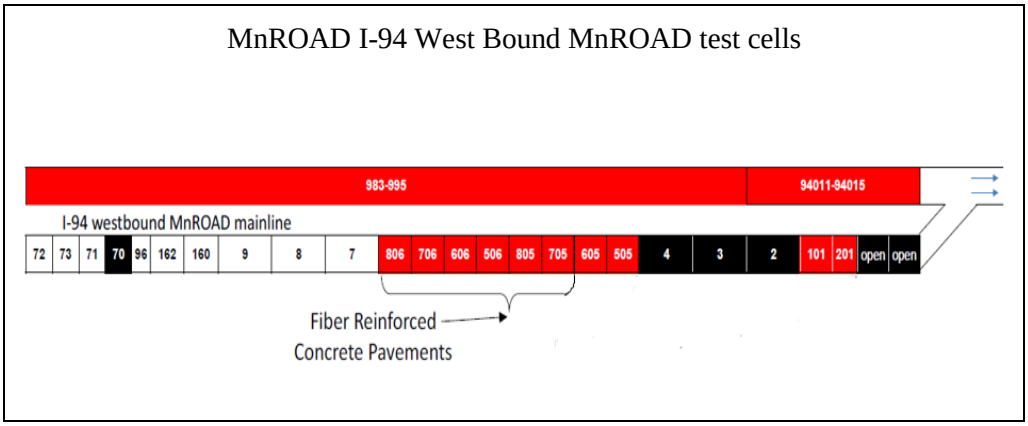

Figure 3-2: Location of the 2017 FRC test cells at the MnROAD test facility (MnDOT, 2018).

Table 3-1: Summary of the test cells.

Cell number	Total Length (ft.)	Type of concrete/ fiber dosage*	No. of Slab Panels
506	144	Plain concrete/ No fiber (Control)	96
606	138	FRC/ standard	92
706	138	FRC/ enhanced	76
806	138	FRC/ high	88

** Fiber dosages: standard (5 lbs./cy) - corresponding to 20% residual strength ratio (ASTM C1609); enhanced (8 lbs./cy)- corresponding to 30% residual strength ratio (ASTM C1609); high (11.66 lbs./cy) – corresponding to 0.75 fibers volume fraction.*

Figure 3-3 gives a better understanding of the cross-sectional details of the four MnROAD test cells (Cell 506-806). In this figure, the FRC layer thickness for Cell 606 can be seen as 5 in. planned but during construction, it was accidentally cast as 6 in. thick as mentioned earlier. All the four cells varied in fiber dosages and were supported underneath by 11 in. class 5Q aggregate base layer, 3 in. existing aggregate base layer, and existing subgrade layer of A-6 clay loam.

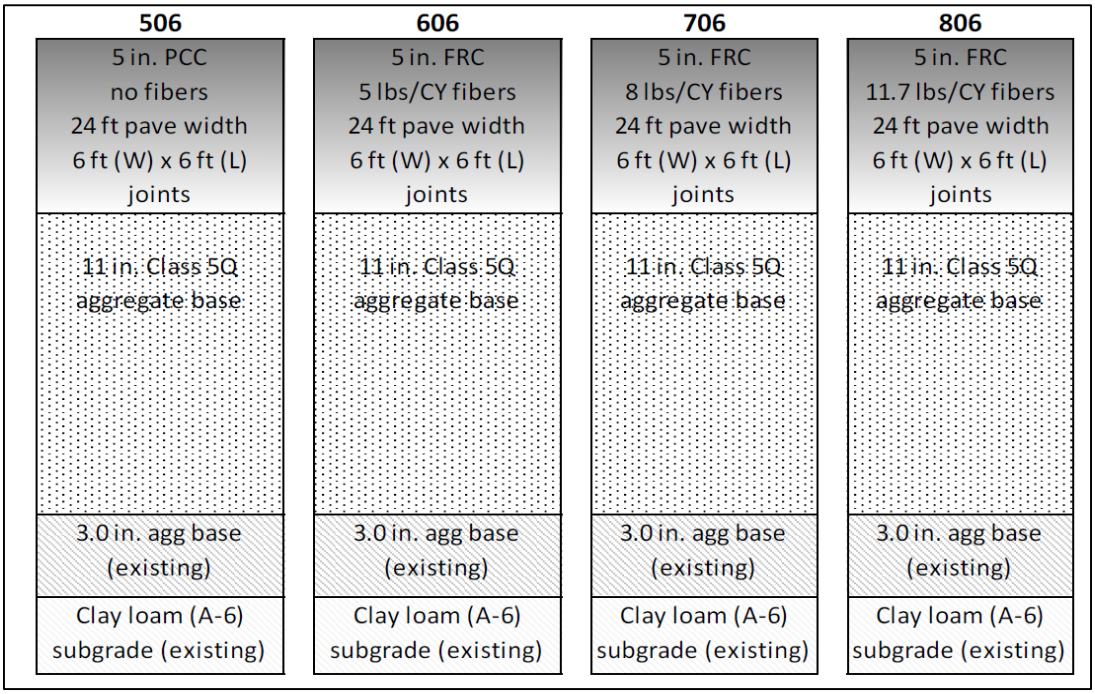

Figure 3-3: Planned section details of the test Cells 506-806 (Deusen et al. 2018).

Table 3-2 shows the paving dates and times of the different cells. Figure 3-4 shows a photograph of the fibers used in all the FRC cells. Table 3-3 represents the concrete mixture-related information for the test cells.

Table 3-2: Paving dates and times of MnROAD 2017 test cells.

Cell	Date	Approximate Time
506	6/26/2017	9:20:00 AM
606	6/27/2017	9:15:00 AM
706	6/29/2017	8:45:00 AM
806	6/30/2017	8:00:00 AM

Figure 3-4: Photograph of the Forta Ferro fibers used in MnROAD 2017 FRC test cells.

Table 3-3. Mix designs for FRC test cells (includes control mix with no fibers)

Mix/Cell	Air (%)	Water (lbs)	Cement (lbs)	Fly ash (lbs)	Fly ash (%)	W/C Ratio	FA #1 (lbs)	CA #1 (lbs)	Fibers (% of conc. vol.)	Fiber Dosage (lbs./cy)	Slump range (in.)
MR-3A21FC/ 506	7.0	239	400	170	30	0.42	1222	1798	0	0	0.5-3
MR-3A21F1/ 606		248	413	177			1204	1773	0.33	5	
MR-3A21F2/ 706		252	420	180			1196	1761	0.52	8	
MR-3A21F3/ 806		258	430	185			1184	1743	0.75	11.66	

Table 3-4 presents the test results of beams prepared at the project site for the ASTM C1609 test. The average 28-day residual strength for the concrete used in Cells 606, 706, and 806 were 124, 156, and 254 psi, respectively. The 28-day MORs for Cell 506, 606, 706, and 806

were 650, 635, 675, and 680 psi, respectively. The static modulus of elasticity was found to be higher in Cell 506 (no fibers) compared to the FRC test cells.

Table 3-4: Measured properties of concrete used in the FRC test cells.

Cell	Hardened concrete properties			
	28-day MOR (psi)	28-day residual strength (psi)	28-day RSR (%)	28-day static modulus of elasticity ($x10^6$ psi)
506	650	-	-	5.4
606	640	124	19.4	4.3
706	680	156	23.0	4.72
806	680	254	37.4	4.61

3.2. Traffic Load

Cells 506 through 806 were constructed on the westbound I-94 mainline section of MnROAD (two lanes of diverted interstate type traffic). Unfortunately, MnROAD test cells are not equipped with any cost-effective sensor that will record the Equivalent Standard Axle Loads (ESAL) directly (Peterson, 2011). However, MnROAD has a Weigh-In-Motion (WIM) sensor that is able to record vehicle types, approximate weight, speed, and numerous other data from the year 1994. This data was later used to estimate the number of ESALs on MnROAD for a given year. The average number of vehicles per day on the mainline was approximately 27,000, which translates to approximately 1 million ESALs per year.

3.3. Sensor Data

MnROAD 2017 FRC research cells were instrumented with four different types of sensors: joint opening, dynamic strain gauge, vibrating wire strain gauge, and temperature sensors (thermocouples). However, only the vibrating wire strain gauge data was relevant for this thesis and is described in the following sub-section. While reporting the vibrating wire strain data, thermocouple data was used to represent the slab temperature at various depths. However, the thermocouple data was not utilized individually in this thesis to generate any stand-alone research findings and thus not discussed in detail. However, details about all the MnROAD pavement sensors can be found in the MnROAD construction report (Deusen et

al., 2018) and Barman et al. (2020) in detail. The sensor layout plan for all four cells is attached in Appendix A. The sensors were installed at various depths along the pavement cross-section with various offsets from the centreline of the pavement.

3.3.1. Vibrating Wire Sensors

Environmentally induced strain responses were measured by vibrating wire (VW) strain gauges. The trends of this strain were investigated with respect to fiber dosage and pavement design features. A photograph of a vibrating wire sensor as used in this study is shown in Figure 3-5. Data was collected every 15 minutes throughout the three years of service considered in this study. The raw data from this type of sensors were converted to estimate the environmental strain that was exerted on the concrete as a result of the change in moisture state, temperature and temperature gradient, freezing of underlying layers, and joint locking. MnDOT has an established procedure for converting the raw vibrating wire data into a meaningful strain. One of the important steps in the vibrating wire data analysis procedure is to determine the initial strain value, which corresponds to the first reading when the concrete has hardened sufficiently to fully engage the sensor, and the temperature difference between the nearby top and bottom temperature sensors is approximately '0'. The initial strain value serves as the baseline value for subsequent readings. In order to determine the above-mentioned initial strain value, temperatures at the top and bottom of the slab and the raw frequency data are plotted together. Using such plots, the time of the first 0-temperature gradient is determined, after the raw frequency data started proper cycling; the corresponding strain at this time is considered as the initial strain value.

Figure 3-5: Photograph of a vibrating wire sensor.

3.3.2. Slab Curvature

Environmental strain is responsible for the concrete pavement slabs to curl up or down. Using the VW strain gauge data, this slab curvature or deformation was computed for the test cells to identify the effects of fibers on environmental strain-induced slab curvature. (Equation 2), as discussed earlier in Section 2.5, was used to calculate slab curvature for the test cells. The unit of slab curvature is 1/ft and the top and bottom longitudinal strain sensors were considered for calculating the slab curvatures at different times of the day. The distance between the top and bottom strain sensors was 3.7 in. The slab curvature values thus calculated were later plotted with respect to the date of strain measurement for Cells 506-806.

The purpose of calculating the slab curvature values from the VW sensor strain data in this study was to investigate whether the macro-fiber and its dosage effect the joint performance of the thin concrete test cells. LTE values and corresponding slab curvature values were plotted for the test cells to compare the effect of macro-fibers on the variation of slab curvature.

3.4. Joint Performance

The Falling Weight Deflectometer (FWD) test was used to determine joint performance. MnDOT uses a trailer-mounted device, as shown in Figure 3-6 that operates by dropping a weight on the pavement and measuring the resulting pavement deflections. The joint load transfer efficiency was calculated as the ratio of the deflections at the unloaded side and the loaded side and expressed as a percentage. The differential displacement was calculated by computing the arithmetic difference between the loaded-side deflection and unloaded-side deflection. The loaded-side displacement was the displacement of the pavement slab under FWD load. In this thesis work, the Load Transfer Efficiency (LTE), Differential Displacements (DD) and Loaded-side Displacements (LD) were measured for the MnROAD test cells throughout the three years of study in all different seasons. Further, the LTE results were used to study the presence of void underneath slabs and determine the pavement temperature-LTE relationship.

Figure 3-6: MnDOT Falling Weight Deflectometer device (Picture Courtesy: Manik Barman, 2020).

3.4.1. Void Study with FWD data

Crovetti and Darter (1985), in their study, investigated the presence of voids underneath concrete pavement slabs using FWD test results. As shown earlier in Figure 2-6, FWD-

measured deflections were plotted against the applied loads for the MnROAD test cells. If the intercept of a deflection line (at zero load) was two mils or below, then it was assumed that the chance of voids present is low. This study was conducted to identify the influence of the macro-fibers in reducing the probability of voids present underneath the concrete pavement slab. One exception in the present study was the use of slab deflections along the wheel path at the transverse joint instead of corner deflections. This modification was made because Cells 506-806 were shorter in plan dimensions (6 ft. x 6 ft.) when compared to conventional concrete pavement slabs. Also, it may be noted that the deflection data collected at the leave slab with the load on the leave slab was used for the void detection analysis because of the probability of more voids present under the leave slabs.

The deflection intercept values were calculated for different seasons for all the cells and were used to determine a factor, 'void index (VI),' to quantify the influence of fibers on the void accumulation underneath the slab, especially at the wheel path-transverse joint intersection. This void index depends on the amount of FWD detected voids present under slabs, with 5 being the best condition with no voids and 0 being the worst condition with excessive voids underneath the slab. Table 3-5 presents the proposed scale of VI for different ranges of deflection-intercepts. This scale was used to determine the VI for all the cells at different seasons using their respective deflection intercepts.

Table 3-5: Scale of the proposed void index.

VI	Voids possibility	Deflection
5	Nil	<2 mils
4	Very less	2-4 mils
3	Less	4-8 mils
2	Moderate	8-12 mils
1	Severe	12-16 mils
0	Very Severe	<16 mils

3.4.2. Pavement Temperature-LTE relationship

The load transfer behavior of fiber reinforced concrete is dictated by the aggregate interlock and dowel action of the fibers. When the temperature was high in the summertime, the crack width closed, and the LTE increased. The exact opposite occured in winter, but the frozen

base and subbase then played a supporting role in transferring the wheel loads. During the spring-thaw season, the joint width remained wide, and the weak support conditions of the granular base resulted in low LTE.

The pavement temperature data was recorded by MnDOT with a surface infrared camera while performing FWD tests. The data was then compared with corresponding LTE values for Cells 506-806, and the effect of fiber reinforcement was studied.

3.5. Transverse Joint Faulting

Transverse joint faulting is referred to as the vertical elevation difference between two adjacent pavement slabs (MnDOT, 2011). In the majority of joint faulting cases, the leave slab goes down, and the approach slab goes up. An example of transverse joint faulting is shown in Figure 3-7, which was observed in Cell 506. MnDOT measured joint faulting at ten different transverse joints in each cell (Cell 506-806). A modified Georgia DOT style fault-meter (Stone, 1991) was used for such measurements. It was mentioned earlier that the surface texture depth for concrete pavements is usually around 0.04 in. or 1 mm on average; therefore, any faulting readings below 1 mm may not be indicating any notable faulting. Faulting for each cell was the average of all the faulting readings taken in a cell.

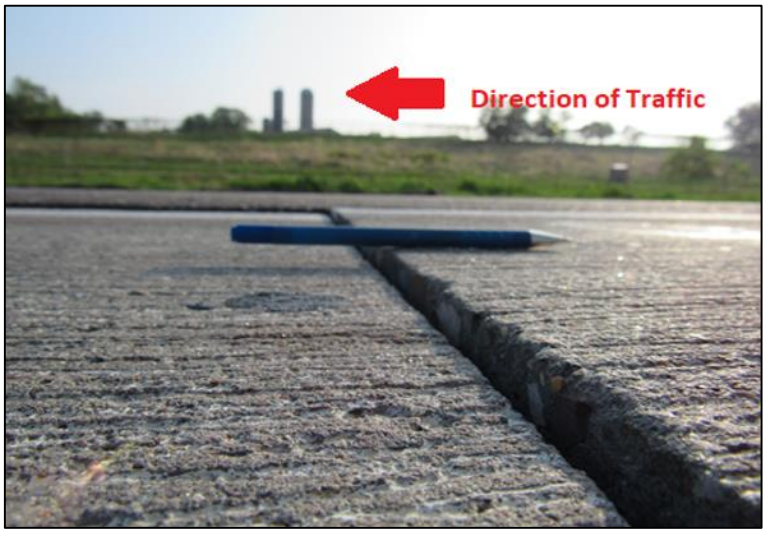

Figure 3-7: Faulting in Cell 506 (no fibers).

N.B.- Faulting is exaggerated due to the broken corner of the leave slab.

3.5.1. Faulting Prediction Equation

Once faulting data was collected, it was plotted with respect to time and ESAL to understand how faulting was related to them and other predictor variables. Apart from traffic, other material properties were also considered while developing the faulting prediction equation in accordance with Table 2-1. Such material properties are discussed as follows:

3.5.1.1. Concrete Mix Design Properties

The concrete mix design properties for all the four MnROAD test cells have already been summarised in Table 3-3. The residual strength values for the cells were also reported previously in Table 3-4. All these values were considered while developing the faulting prediction equation for the test cells.

3.5.1.2. Base Layer Properties

Base materials used in the test cells (Cell 506-806) were not tested under the scope of this study. Resilient modulus values for similar base materials were collected from MnDOT pavement design manual (2007). Table 3-6 shows the resilient modulus values for different types of base and subbase materials for different seasons. Resilient modulus results for MnDOT Class 5 aggregates were used for this study.

Table 3-6: MnDOT base/subbase layer resilient modulus values for various aggregate class (MnDOT, 2007).

Mn/DOT Material Classification	Granular Equivalent (G.E. Value)	Resilient Modulus by Season									
		Early Spring		Late Spring		Summer		Fall		Winter	
		MPa	ksi	MPa	ksi	MPa	ksi	MPa	ksi	MPa	ksi
CLASS 7 (Mn/DOT Spec. 3138)	1.0	62	9	124	18	207	30	228	33	350	50
CLASS 6 (Mn/DOT Spec. 3138)	1.0	71	10	141	20	236	34	259	38	350	50
CLASS 5 (Mn/DOT Spec. 3138)	1.0	62	9	124	18	207	30	228	33	350	50
CLASS 4 (Mn/DOT Spec. 3138)	0.75	58	8.3	115	16.7	192	27.8	211	30.6	350	50
CLASS 3 (Mn/DOT Spec. 3138)	0.75	58	8.3	115	16.7	192	27.8	211	30.6	350	50
SELECT GRANULAR (Mn/DOT Spec. 3149.2B2)	0.5	58	8.3	115	16.7	192	27.8	211	30.6	350	50
GRANULAR (Mn/DOT Spec. 3149.2B1)	NA	35	5.1	70	10.2	117	17.0	129	18.7	350	50

3.5.1.3. Subgrade / Sublayer Properties

The subgrade layer properties were characterized using the combined modulus of subgrade reaction (k_{comb}). As the granular subbase and subgrade support varies with seasons, mainly because of the subbase strength associated with the change in moisture content, different k_{comb} values were assigned for different seasons. The ACPA static k_{comb} calculator was used to estimate the k_{comb} for different seasons. The thickness of the subbase layer and subgrade resilient modulus were the input for the estimation of k_{comb}. A screenshot of the webpage related to the ACPA static k_{comb} calculator is shown in Figure 3-8. Combined modulus of subgrade reaction values were calculated for different seasons. The k_{comb} values for the late spring, summer and fall seasons were 304, 551 and 637 psi/in. respectively. Later, these values were utilized in developing the faulting prediction equation.

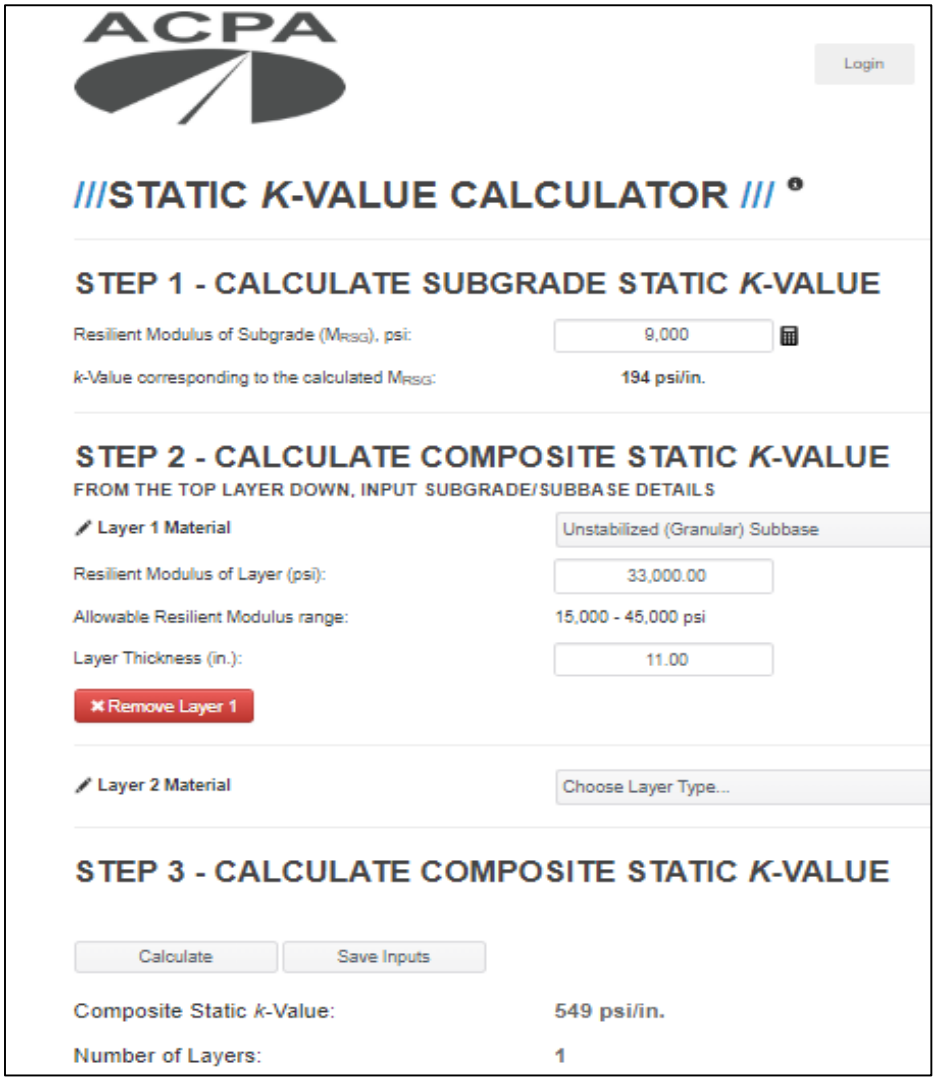

Figure 3-8: Example of ACPA static k-value calculator.

3.5.2. Faulting Index

As discussed earlier, faulting values below 0.04 in. (1 mm), which includes negative faulting, were not considered significant and the joints were not considered faulted according to MnDOT. However, in this study, a parameter called “Faulting Index” was developed for the FRC test cells under consideration which considered positive as well as negative faulting values. The following (Equation 3) was used to compute the Faulting Index (FI) for each cell in this study:

$$FI = \frac{F_{abs}}{N_{measured}} * N_{total} \qquad \text{(Equation 3)}$$

Where,

FI = Faulting Index of a particular MnROAD cell, in.

F_{abs} = Summation of the absolute values of all the faulting measurements by the modified Georgia Fault-meter in each cell, in.

$N_{measured}$ = No. of joints where faulting was measured. (10 nos. for each of the Cells 506-806.)

N_{total} = Total number of transverse joints in each of the Cells 506-806. Cell 506, 606, 706 and 806 had 25, 24, 23 and 23 nos. of transverse joints respectively.

3.5.3. FI – IRI Relationship

FI/mile was calculated as an approximate estimate of the FI for one mile stretch of a similar thin concrete pavement. This was developed to compare the FI with pavement roughness parameter, International Roughness Index (IRI), which is in the unit of in. /mile. FI/mile was calculated by the following (Equation 4):

$$FI/mile = \frac{(FI * 5280)}{Total\ length\ of\ the\ Cell} \qquad \text{(Equation 4)}$$

The total length for each test cell was mentioned in Table 3-1. The pavement roughnesses for the four MnDOT test cells were measured in terms of the International Roughness Index (IRI). The (Equation 1) as mentioned in section 2.4 was used to back-calculate the limiting or threshold values of IRI for RQI values 0.0 to 5.0 and are given in the following Table 3-7.

Table 3-7: RQI and IRI rating scale.

Verbal Rating	RQI	IRI (in./mile)
Very good	4.1 - 5.0	20 - 55
Good	3.1 - 4.0	56 - 105
Fair	2.1 - 3.0	106 - 172
Poor	1.1 - 2.0	173 - 255
Very Poor	0.0 – 1.0	256 - 353

3.6. Fatigue Cracking

MnDOT surveyed distresses such as cracks, spalling and documented them periodically. Such survey records are presented in Table 3-8, which provides the dates of the crack surveys and the corresponding equivalent standard axle loads (ESAL) at that time. An example of a cracked slab panel at the MnROAD field section is shown in Figure 3-9. Distress surveys were conducted by visually observing and documenting the distresses on MnDOT's distress survey sheets. An example of such a distress survey sheet by MnDOT is presented in Figure 3-10, which notes the distresses until March 2020. Color-coded distress survey summary plots were drawn from such survey sheets and are presented in Chapter 5.

Figure 3-9: Transverse and Diagonal Cracks Observed in Cell 506 (October, 2019).

Table 3-8: Distress survey dates by MnDOT

Cell	Construction dates in 2017	Distress survey Dates in 2018/ ESALs	Distress survey dates in 2019 / ESALs	Distress survey dates in 2020/ESALs
506	Jun 26	Mar 14/ 750K	Mar 19/ 1,800K; Oct 25/ 2,400K	Mar 5/2700K
606	Jun 27	Mar 14/ 750K	Mar 19/ 1,800K; Oct 25/ 2,400K	Mar 5/2700K
706	Jun 29	Mar 14/ 750K	Mar 19/ 1,800K; Oct 25/ 2,400K	Mar 5/2700K
806	Jun 30	Mar 14/ 750K	Mar 19/ 1,800K; Oct 25/ 2,400K	Mar 5/2700K

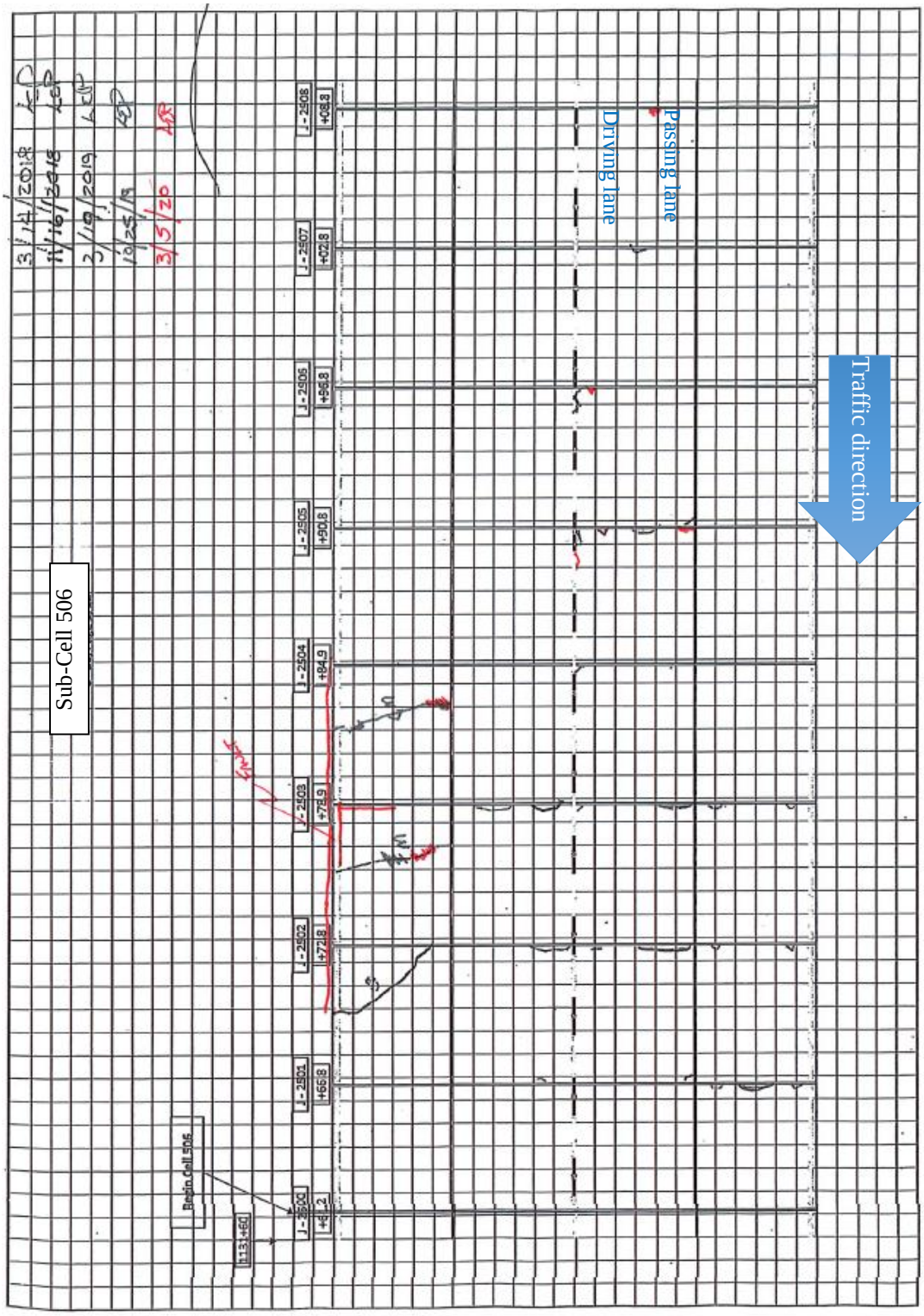

Figure 3-10: Example of a Distress Survey Sheet for Cell 506; Courtesy-MnDOT.

The crack data analysis was conducted in this thesis work with the limited available crack data for the test cells. A parameter called “Crack Percentage” was calculated, which was expressed as the percentage of the total cracked slabs on a given date for a particular test cell

to the total number of slabs for that cell. Once this crack percentage was calculated for all the test cells, crack percentage with respect to ESAL was plotted and the figures were discussed.

3.7. Summary

In this chapter, various research methodologies and data collection relevant to this thesis work were discussed. The four MnROAD thin concrete pavement cells (Cell 506-806) varied in fiber dosage. The test cells were exposed to 1 million ESAL per year even though they were designed for low traffic volume. Of the various pavement sensors installed in the test cells, only vibrating wire sensors were under the scope of this study. VW sensor data was utilized to evaluate environmental strain induced slab curvature using (Equation 2) and slab curvature-LTE relationship was established. The joint performance data was used to identify the presence of voids underneath the test cells according to Crovetti and Darter (1985) study. A parameter called void index was proposed with a scale of 0 to 5; 5 being no voids and 0 being high probability of voids. Next, distress data (joint faulting and fatigue cracking) collection and analysis procedure was presented. Variables affecting transverse joint faulting were identified to be traffic load, concrete mix design, base modulus, and subgrade modulus. A parameter called "Faulting Index" was defined as average faulting in test cells considering both positive and negative faulting values. (Equation 1) was used to convert RQI values to IRI values and the procedure to establish a relationship of FI with IRI was discussed. Fatigue crack percentage was calculated as the ratio of no. of slabs cracked to the total no. of slabs of a given test cell, expressed in percentage. An effort was made in this chapter to draw a path towards the accomplishment of the objectives of this thesis as provided in section 1.2.

4. Pavement Structural Responses

This chapter presents the results and discussion of the pavement structural responses like load transfer efficiency, differential displacements, loaded side displacement and associated studies like determining the presence of voids underneath concrete pavement slab and pavement temperature-LTE relationship. This chapter also discusses the trends of environmental strains as recorded with the VW sensors for the test cells. Later, these static environmental strains were used to compute slab curvature. Finally, the effect of synthetic macro-fibers' addition in thin concrete pavements were discussed with the help of slab curvature - LTE relationship.

4.1. Joint Performance

The results of the FWD test conducted at selected transverse joints for the years 2017, 2018, 2019 and 2020, were used to study the load transfer efficiency (LTE), differential displacement (DD) and loaded-side displacements (LD) for all the four test cells (Cell 506-806). Passing lanes of all the test cells were missing September 2017 data and thus not reported in this thesis.

4.1.1. Load Transfer Efficiency

Figure 4-1 through Figure 4-8 show the LTE of all the test cells. The LTE results clearly reveals the contribution of structural fibers in keeping the LTE high. For Cell 506 (plain concrete), even though the FWD test conducted on the driving lane in September 2017 (year of construction) showed the range of LTEs between 75 and 85%, the LTE afterwards significantly decreased overall. Surprisingly, the FWD tests conducted during the April and June 2019, showed relatively higher LTE at all the three joints considered. The LTE in the passing lane of Cell 506 was always low, with a maximum of around 50%. The reason behind this may be that the absence of fibers in this cell resulted in reduced load transfer and the aggregate interlock between the transverse joints was unable to provide enough load transfer. The 2020 FWD test results showed a considerable and steady decrease in LTE for Cell 506.

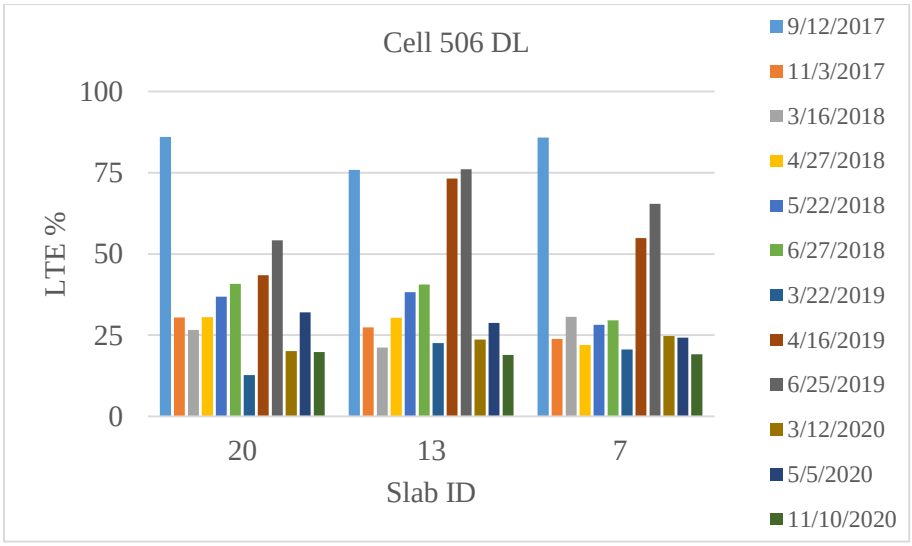

Figure 4-1: LTE of Cell 506 driving lane.

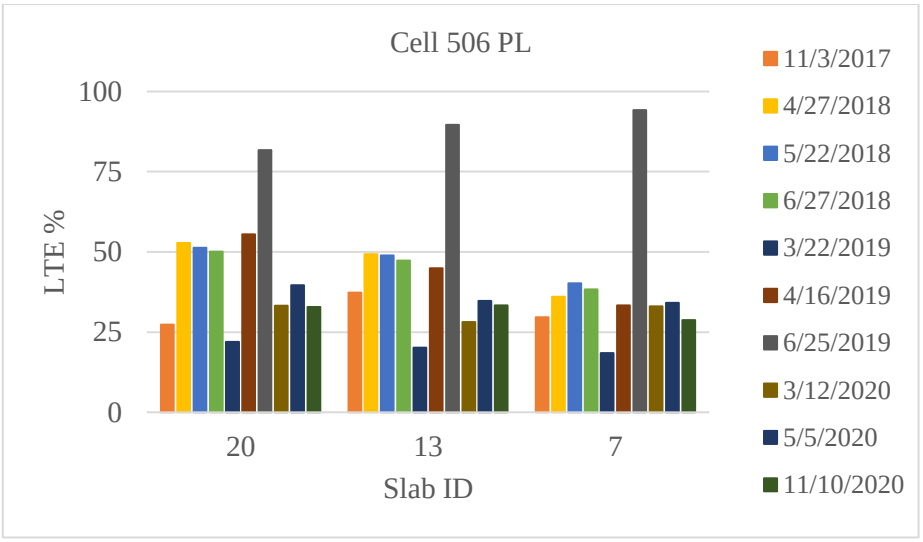

Figure 4-2: LTE of Cell 506 passing lane.

The LTE results of Cell 606 (5 lbs./cy fiber), which was 6-in. thick, were at or above 90% when measured in September 2017, except for one joint in the passing lane which always showed a low LTE (around 25 to 50%). The LTE for this cell dropped significantly over time. The FWD tests conducted on Cell 606 during the third year of service showed a gradual decrease in LTE for all the joints. The LTE in the passing lane also dropped significantly except for the slab ID 18 which showed a very high LTE throughout. The exact reason behind

this is not completely understood but it may be a combined effect of higher fiber count at the joint and thicker slab of Cell 606.

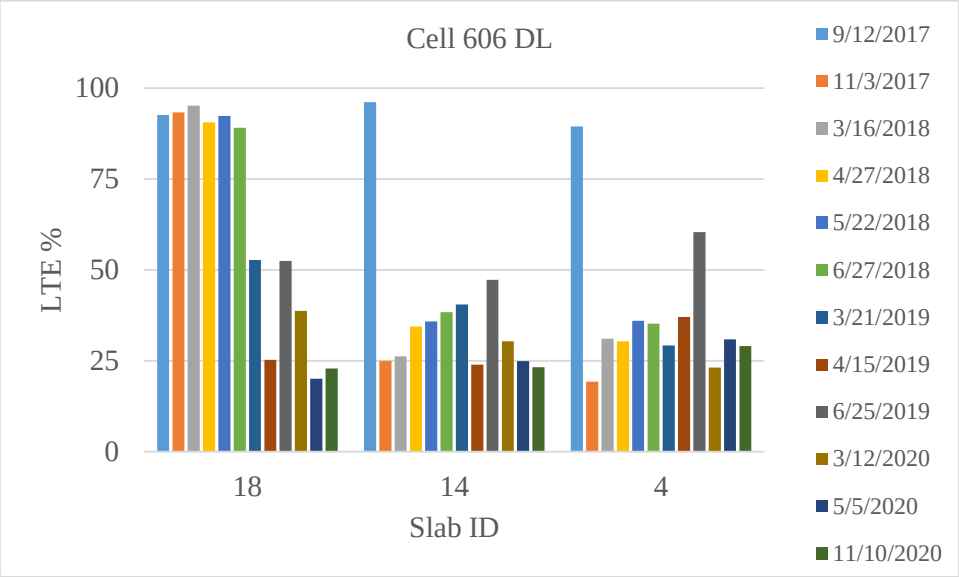

Figure 4-3: LTE of Cell 606 driving lane.

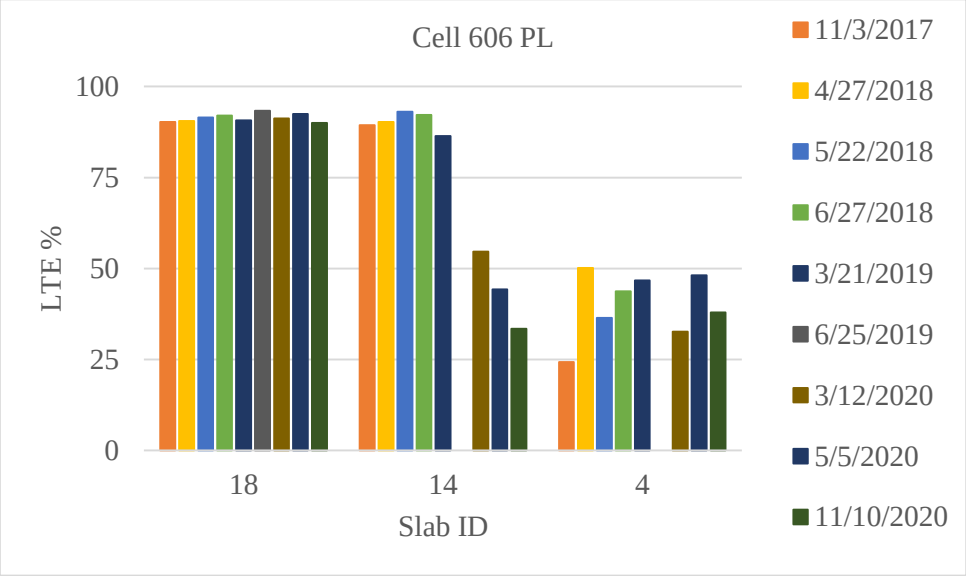

Figure 4-4: LTE of Cell 606 passing lane.

The LTE of Cell 706, which was 5-in. thick and contained 8 lbs./cy fibers, was initially high at three joints (at the driving lane) out of the total six joints (driving and passing lane)

measured. However, when measured at later dates (during the summer of 2019), these joints exhibited 40 to 56% LTE. The LTE values decreased afterwards to an average of 30% during the year 2020.

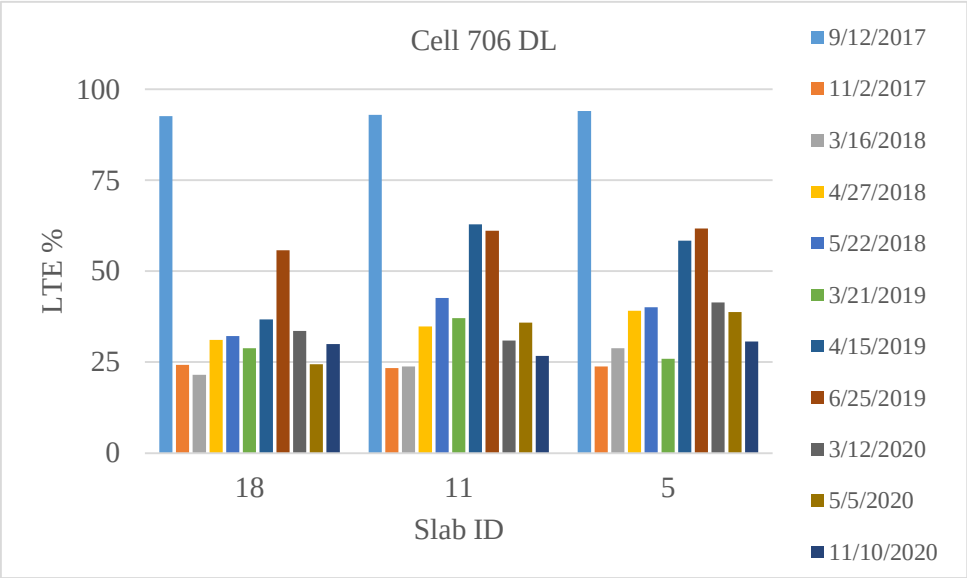

Figure 4-5: LTE of Cell 706 driving lane.

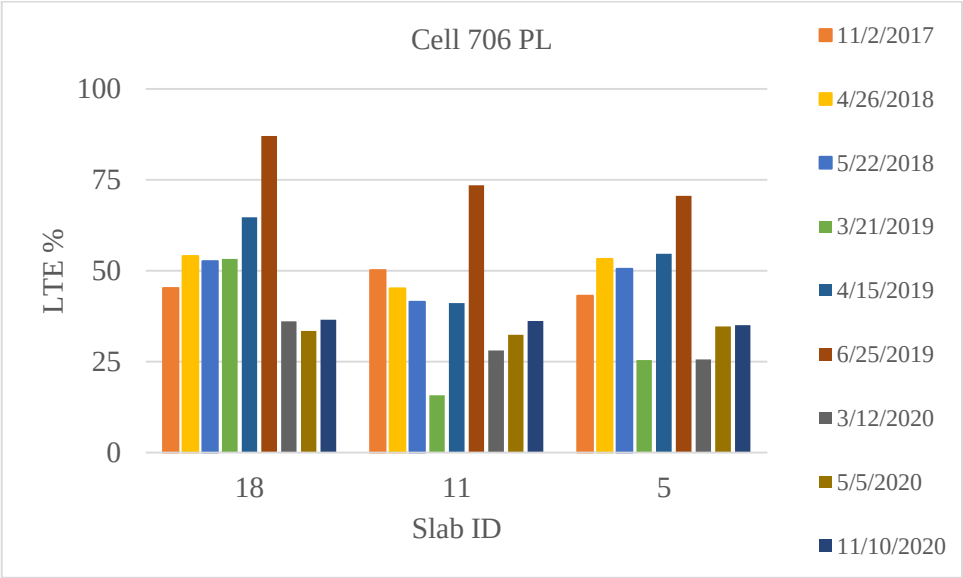

Figure 4-6: LTE of Cell 706 passing lane.

Cell 806, which was 5-in. thick and contained 11.66 lbs./cy of fibers, consistently exhibited the highest LTE among all the cells, until 2019. Notably, all the joints were able to maintain a very good LTE between 88 to 94% throughout the first two years of service life. The higher LTE of this cell helped in keeping the faulting (discussed in Chapter 5) to the lowest among all the four cells. Third year data for Cell 806 showed that for the driving lane, the LTE decreased overall to an average of 30%. However, the passing lane LTE showed an average value of 90%, which was significantly higher when compared to all the other cells. The dramatic decline in the LTE values for the Cell 806 driving lane indicates that the contribution of fibers and/ or aggregate interlock have significantly reduced after approximately 2.5 million ESALs.

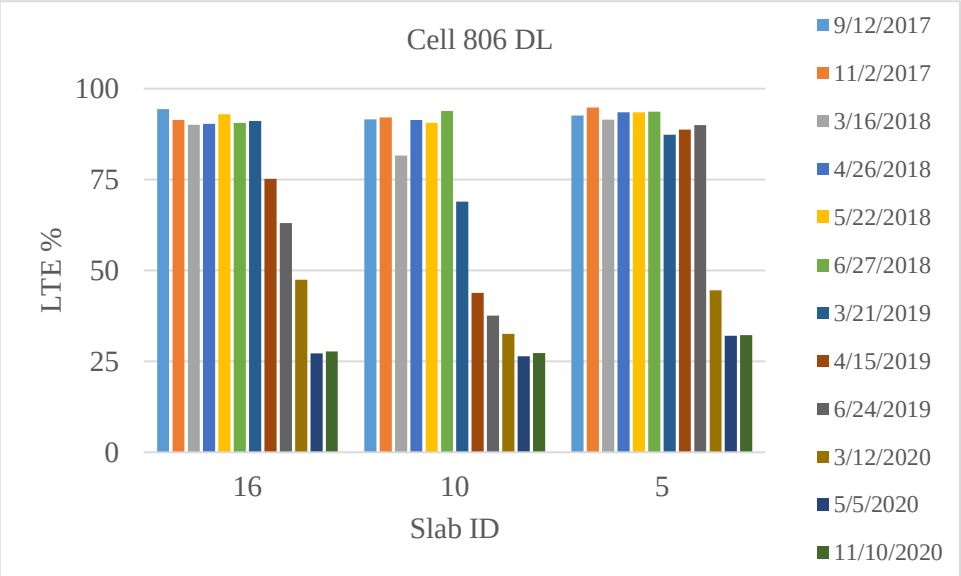

Figure 4-7: LTE of Cell 806 driving lane.

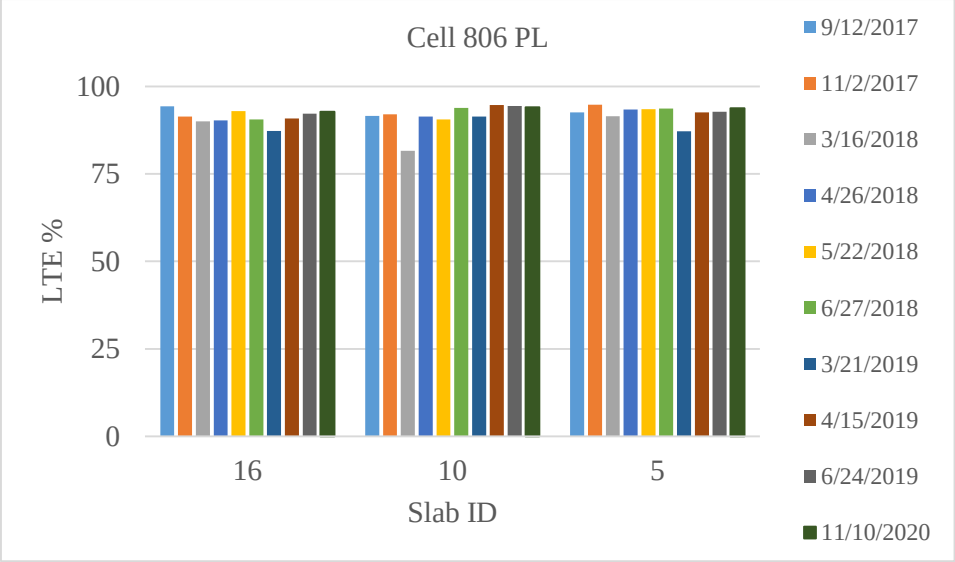

Figure 4-8**:** LTE of Cell 806 passing lane.

Figure 4-9 shows the LTE vs ESAL relationship for the test cells in the driving lane. The LTE value for each test cell was the average of all the slabs where FWD test was conducted. The secondary X-axis represents the corresponding age of the test cells in months. It can be seen in this figure that initially during the first year of study, the LTE values for all the cells were high (between 80-95%). Post two years of service, the Cell 806 with maximum fiber dosage exhibited approximately 70% LTE and Cell 506 with no fibers showed approximately 40% LTE. This represents the fact that addition of macro-fibers in thin concrete pavements is helping in keeping the joint performance higher. The drastic decrease in LTE of the test cells after two years is a result of the type of loading. Although the test cells were constructed only 5-in. thick (6-in. for Cell 606), they were exposed to interstate traffic (I-94 westbound) which created an accelerated loading condition. In reality, such thin test cells should be constructed for low volume roads and in that case, the drop in LTE values may not be this drastic.

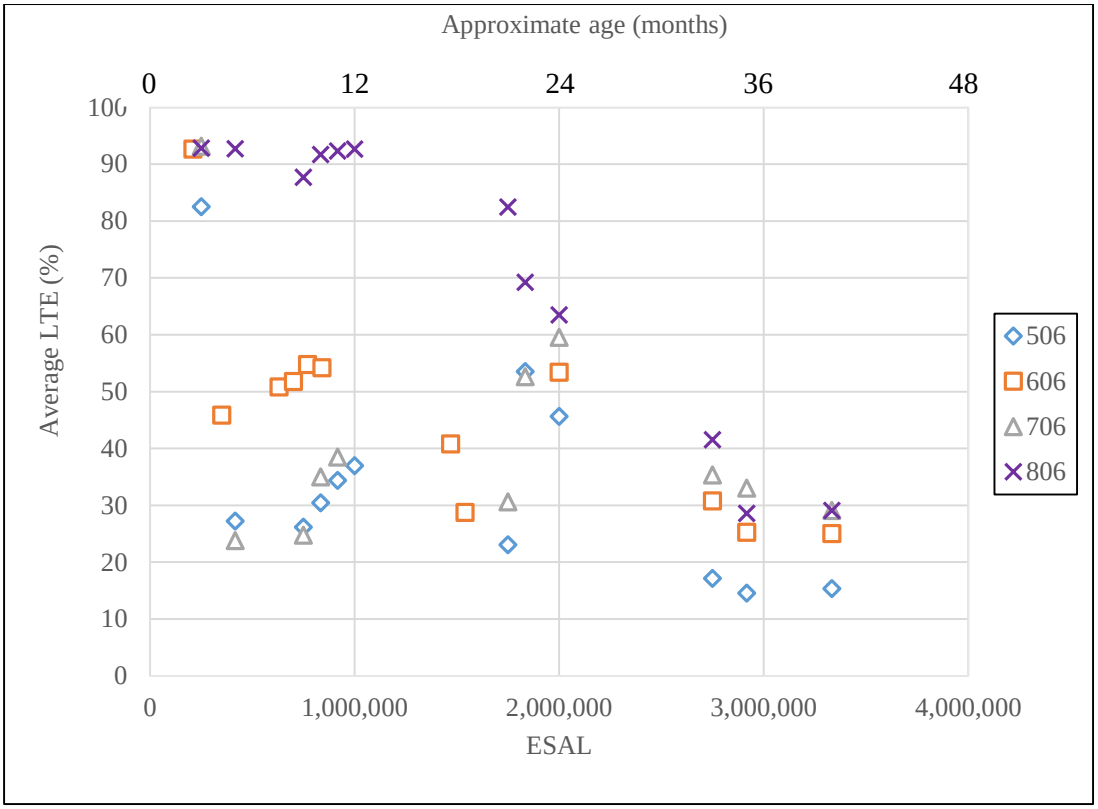

Figure 4-9**:** Average LTE vs ESAL for the test cells in driving lane.

4.1.2. Differential Displacement

The contribution of fibers in joint performance can also be seen in the differential displacement plots for Cell 506 through 806 as shown from Figure 4-10 to Figure 4-17. The driving lanes of Cells 506, 606 and 706 exhibited higher differential displacements than that of Cell 806. Cell 506 showed hgher differential displacement initially, but then deacreased with traffic and then again increased in the year 2020. With the highest fiber dosage, the driving lane of Cell 806 had neglegible differential displacement compared to other cells, until spring of 2020 when it started increasing with the traffic. This was expected and matches with the LTE observations. The passing lane of Cell 806 showed negligible differential displacement throughout.

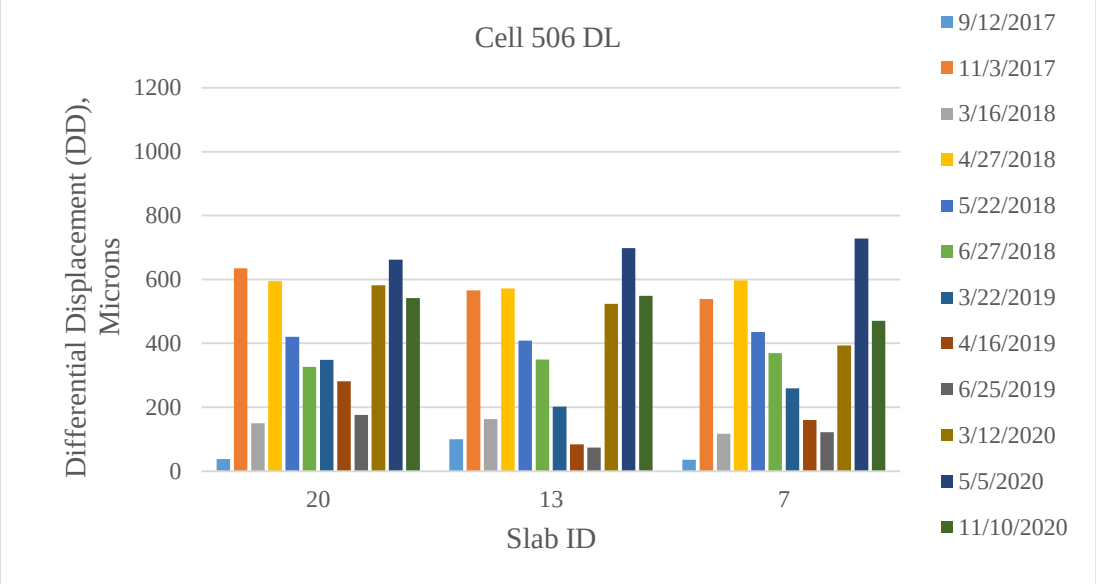

Figure 4-10: Differential displacement of Cell 506 driving lane.

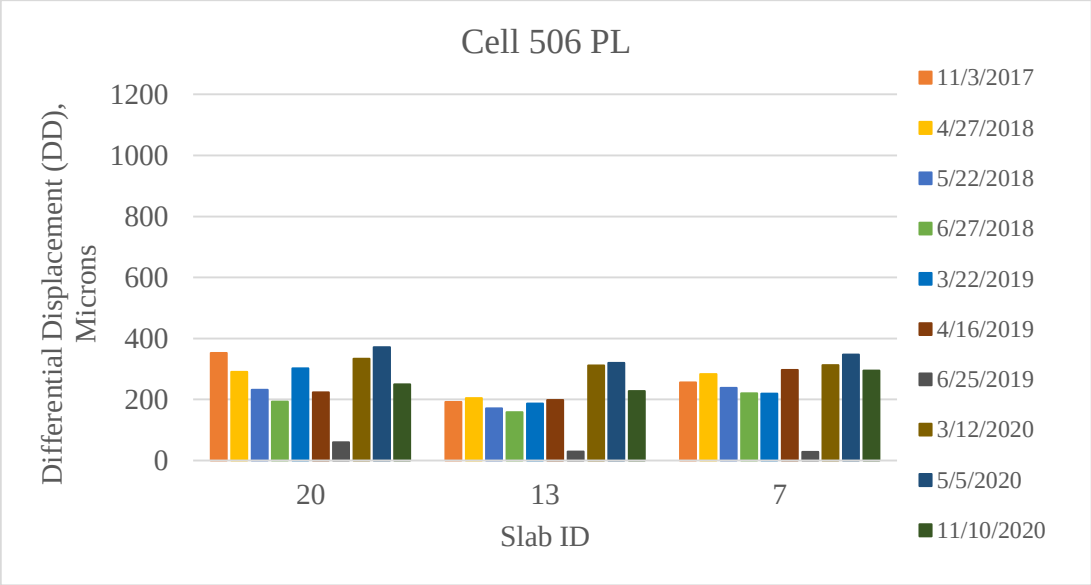

Figure 4-11. Differential displacement of Cell 506 passing lane.

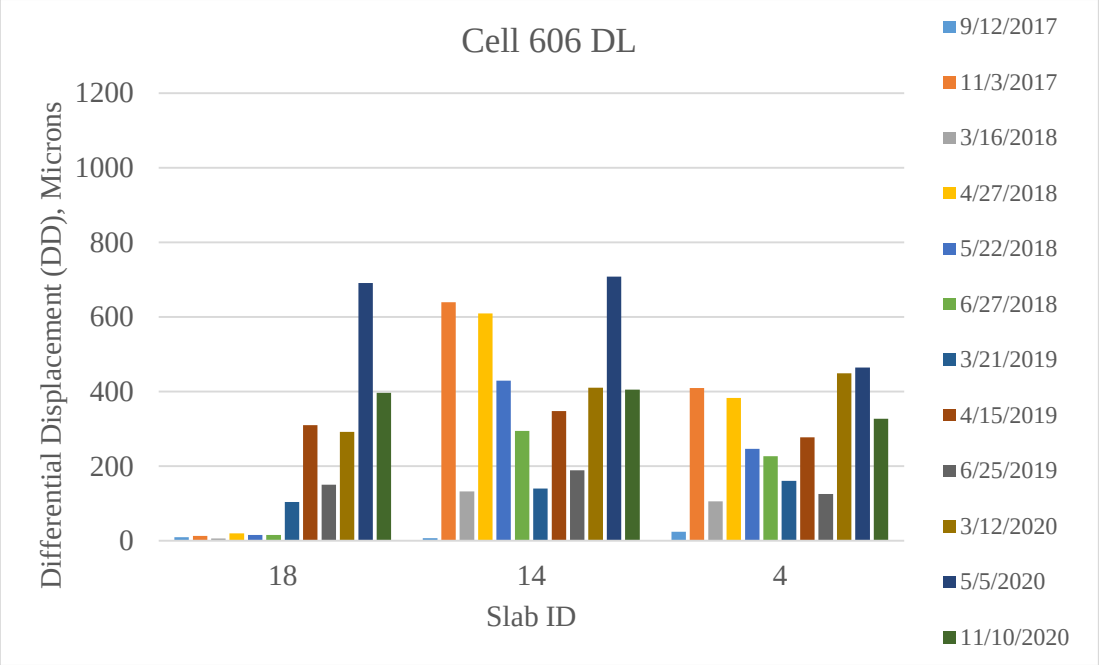

Figure 4-12. Differential displacement of Cell 606 driving lane.

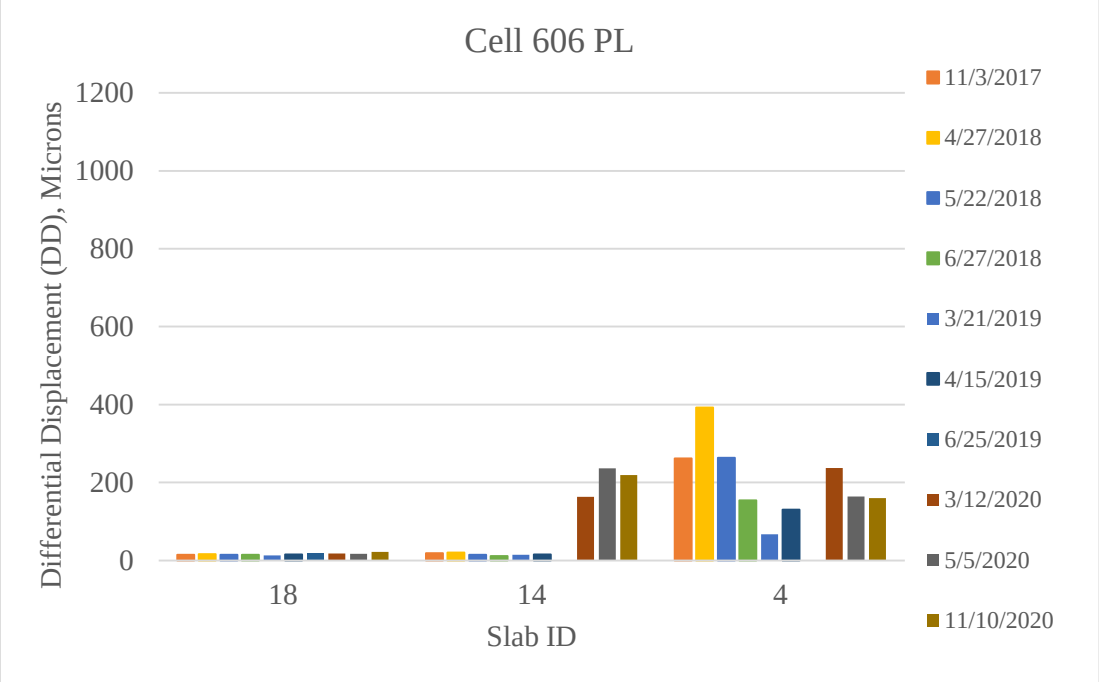

Figure 4-13. Differential displacement of Cell 606 passing lane.

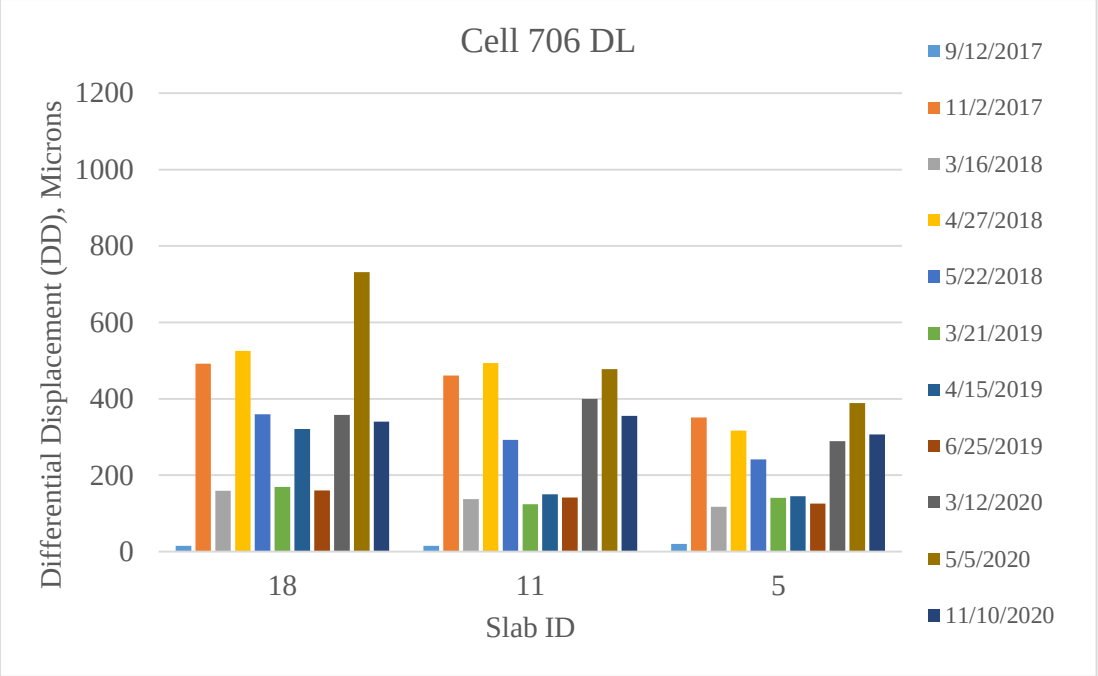

Figure 4-14. Differential displacement of Cell 706 driving lane.

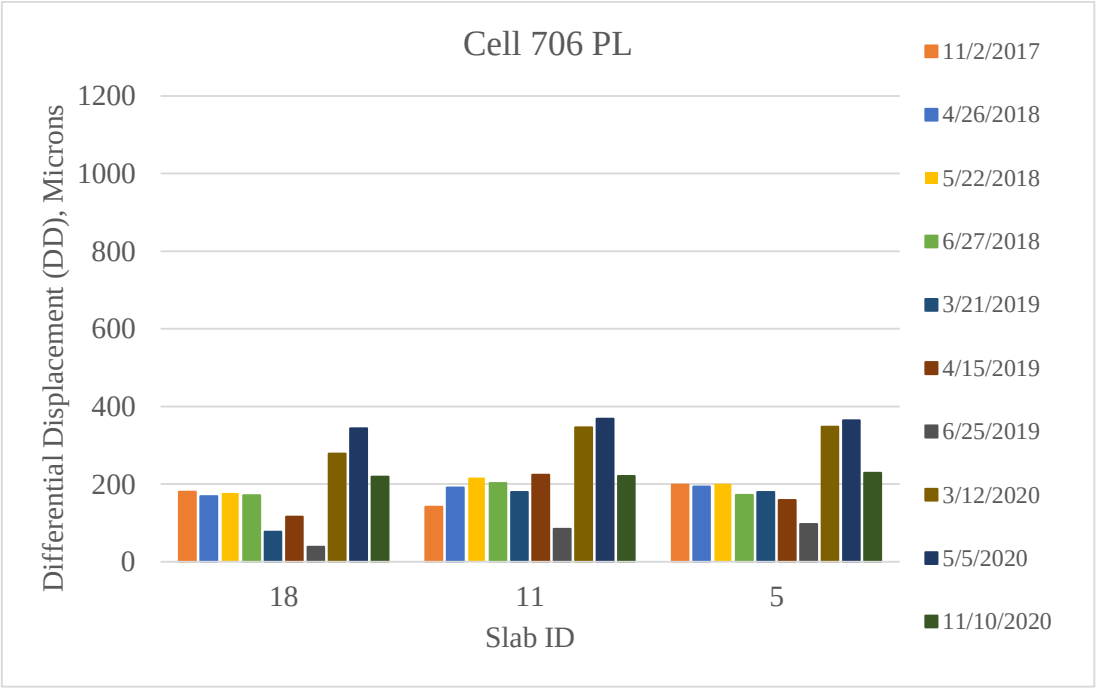

Figure 4-15. Differential displacement of Cell 706 passing lane.

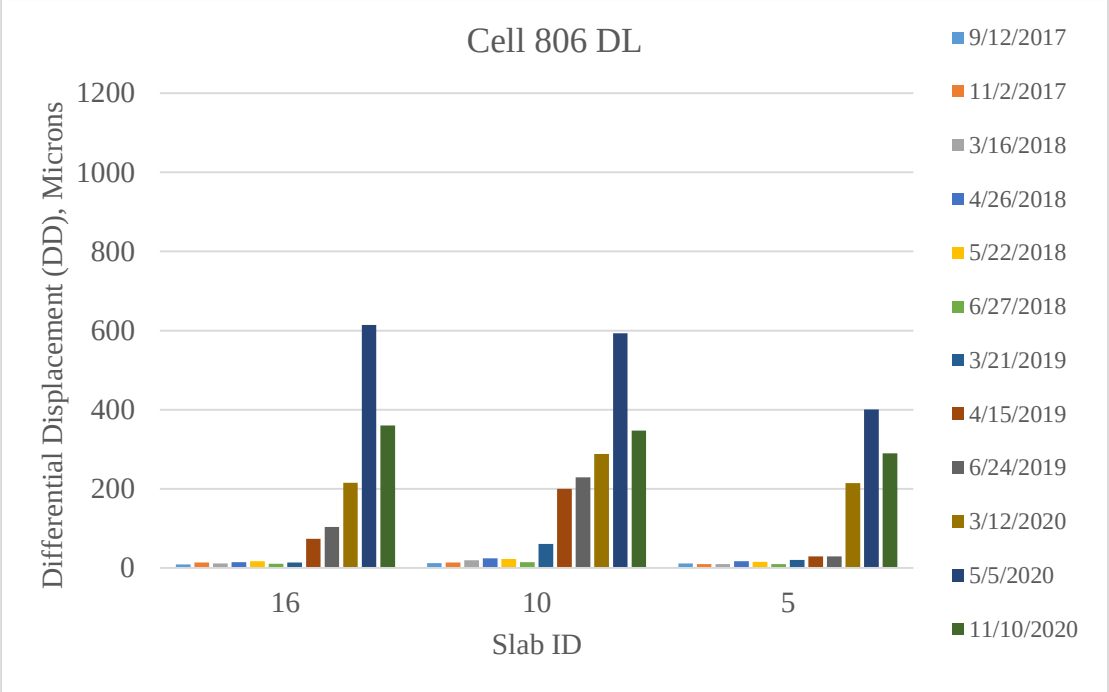

Figure 4-16. Differential displacement of Cell 806 driving lane.

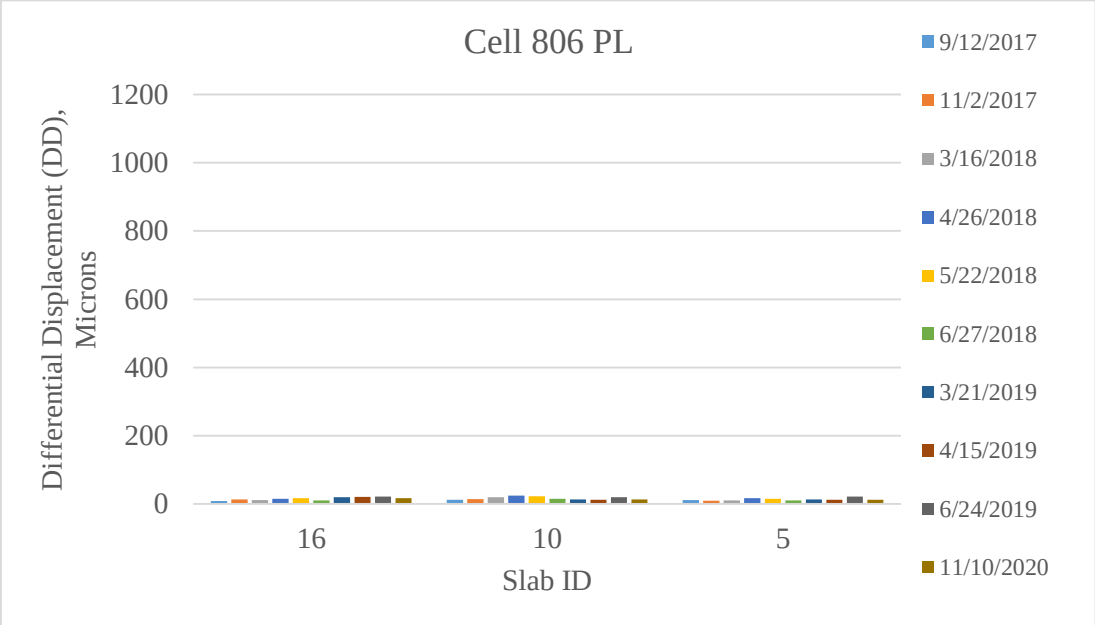

Figure 4-17. Differential displacement of Cell 806 passing lane.

Figure 4-18 shows the average differential displacement vs ESALs for all the test cells in driving lane. The secondary X-axis here shows the age of the test cells in months. Cell 806 with the highest fiber dosage showed the least differential displacement of all the test cells. This trend continued throughout the study period and by end of three years and 3 million

ESALs, three fiber reinforced test cells (Cell 606, 706 and, 806) showed differential displacement of about 350 microns and Cell 506 with no fibers showed a greater differential displacement of 500 microns.

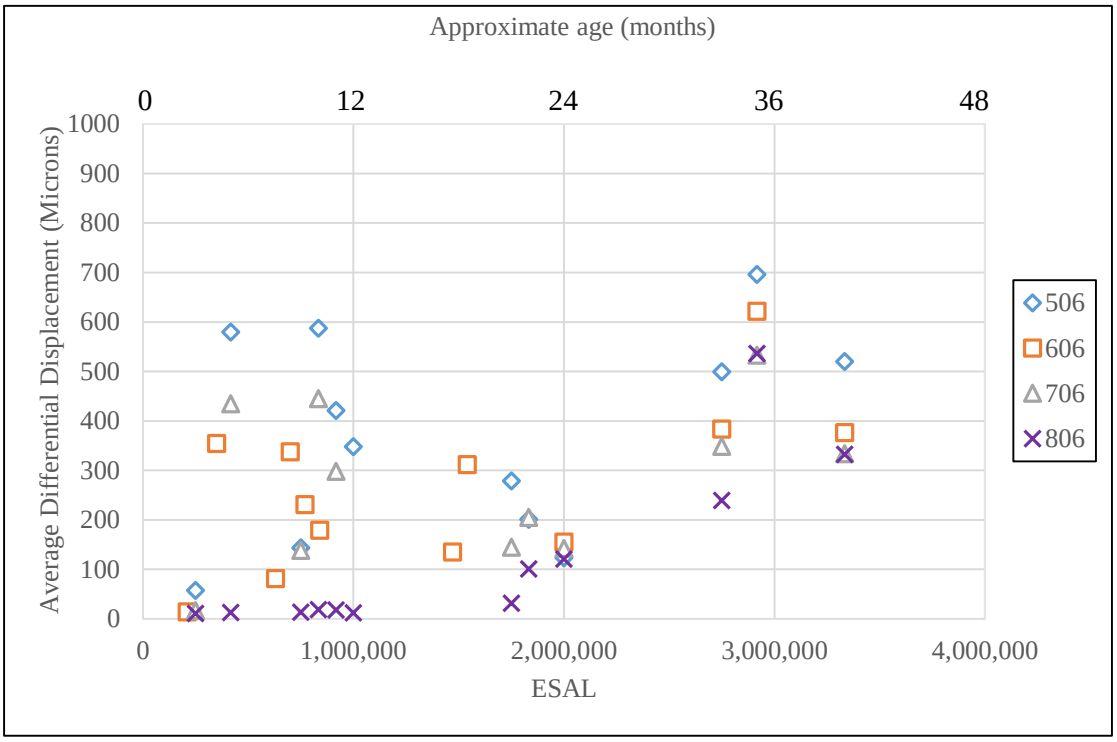

Figure 4-18. Average differential displacement vs. ESAL for the test cells in driving lane.

4.1.3. Loaded-side Displacement

The loaded-side displacement of Cells 506 through 806 as shown from Figure 4-19 to Figure 4-26 also showed that the Cell 806 performed better than the other three cells initially until approximately 2.5 million ESALs. The 2020 FWD data (beyond 2.5 million ESALs) indicates that all four cells had similar loaded-side displacement, with Cell 506 (no fiber) slightly higher than the other three. Overall, it can be stated that the notable influence of fibers was observed until 2.5 million ESALs, afterwhich, the PCC and FRC behaved similarly weak.

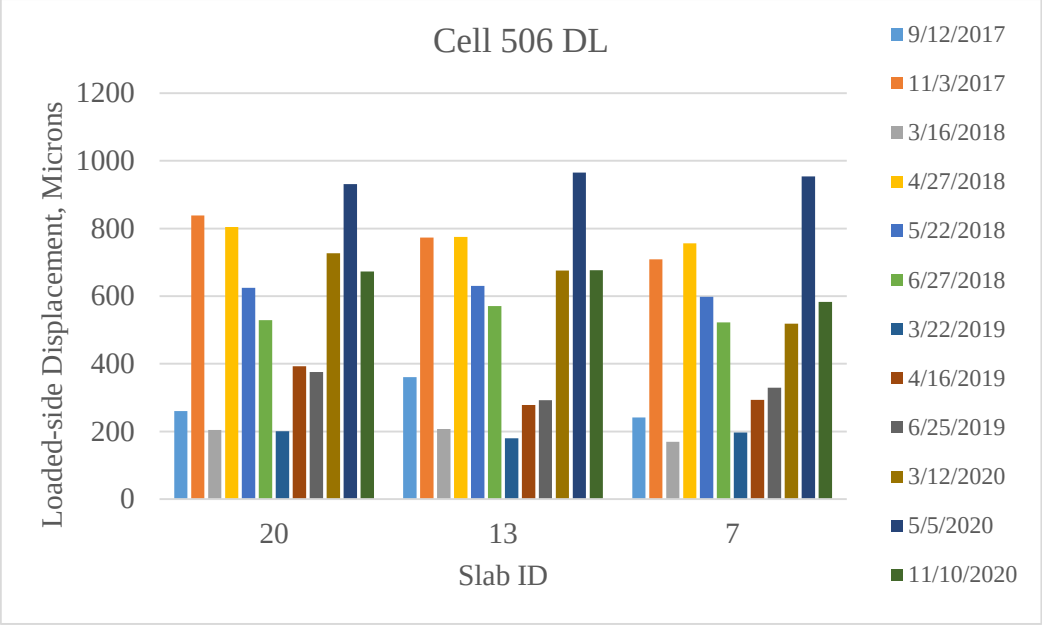

Figure 4-19. Loaded-side displacement of Cell 506 driving lane.

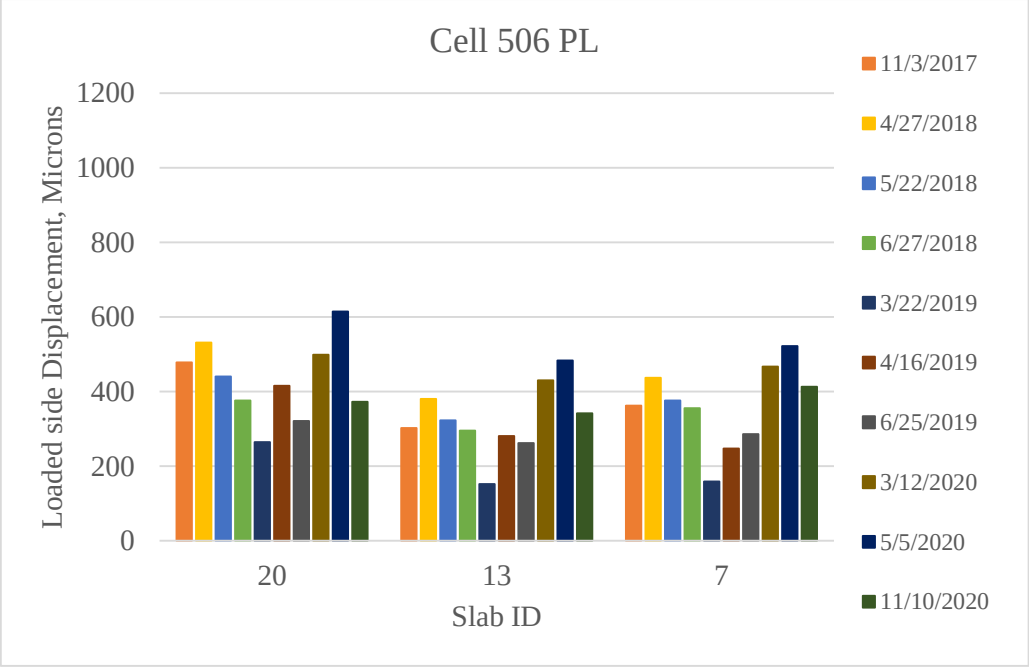

Figure 4-20. Loaded-side displacement of Cell 506 passing lane.

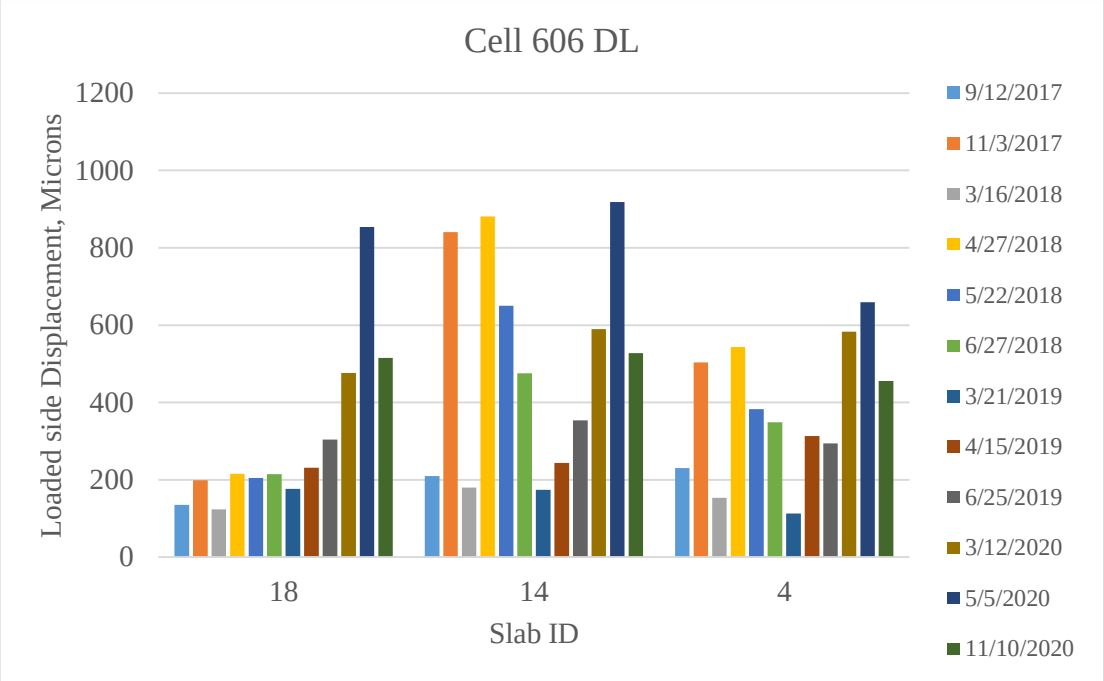

Figure 4-21. Loaded-side displacement of Cell 606 driving lane.

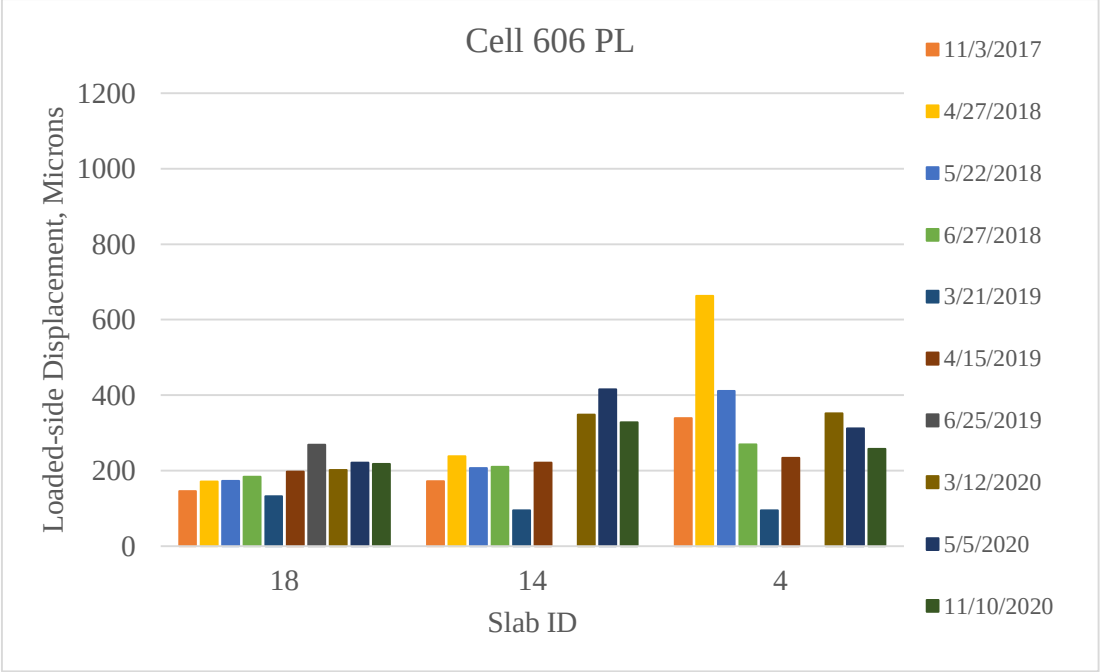

Figure 4-22. Loaded-side displacement of Cell 606 passing lane.

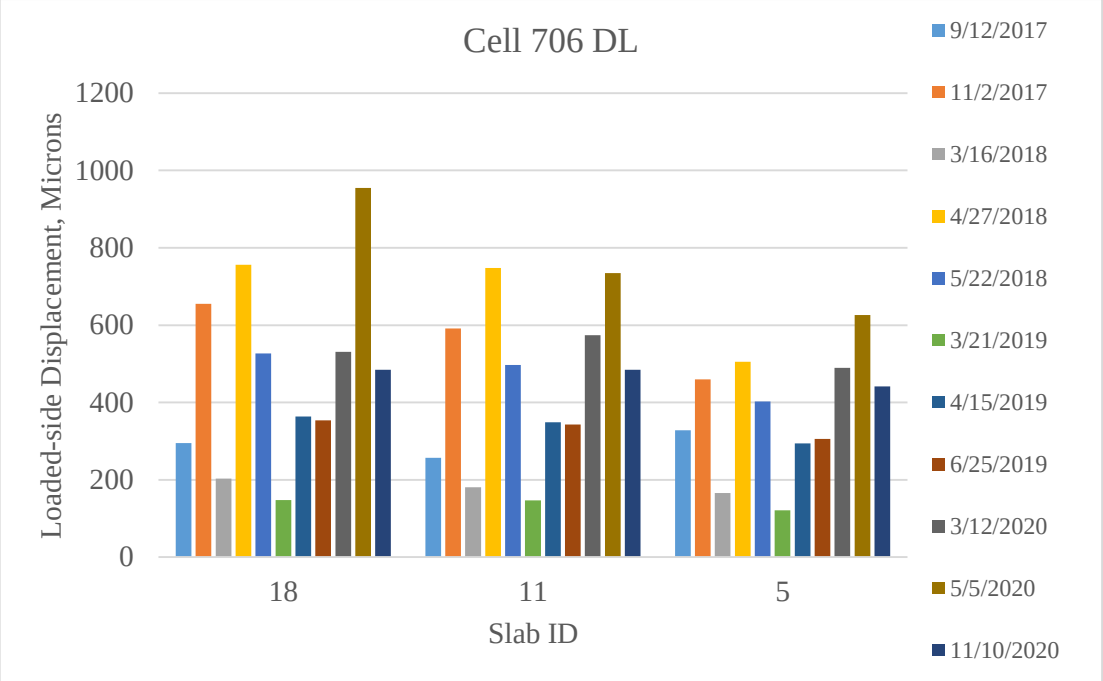

Figure 4-23. Loaded-side displacement of Cell 706 driving lane.

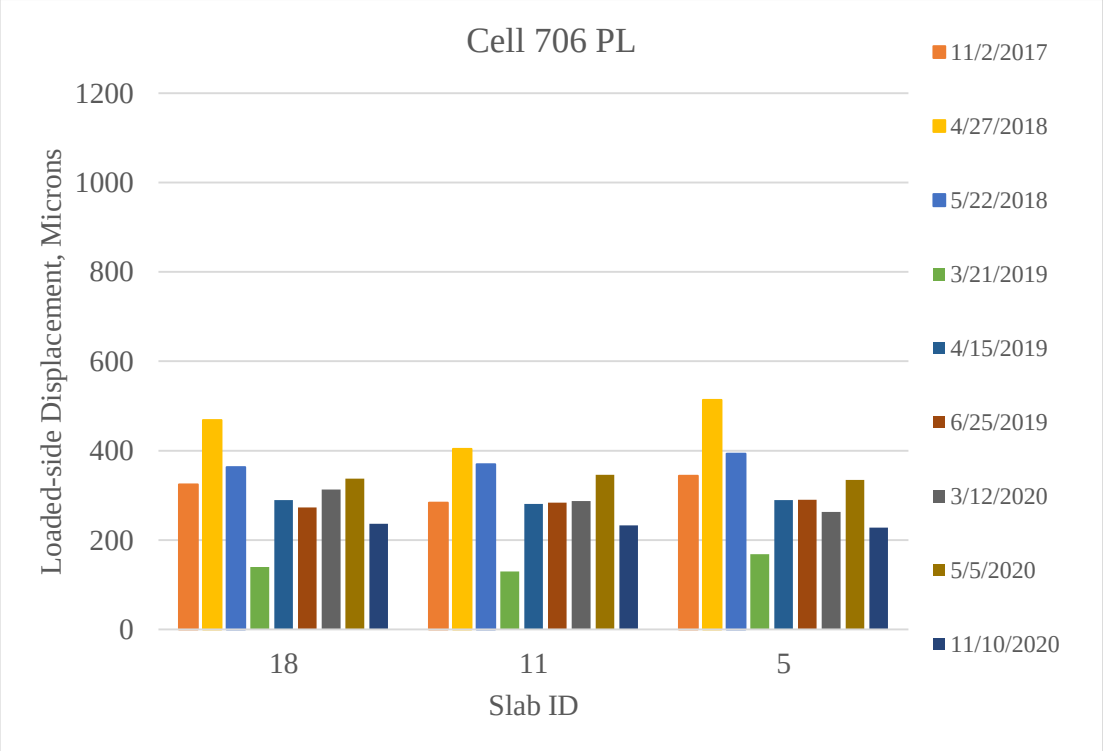

Figure 4-24. Loaded-side displacement of Cell 706 passing lane.

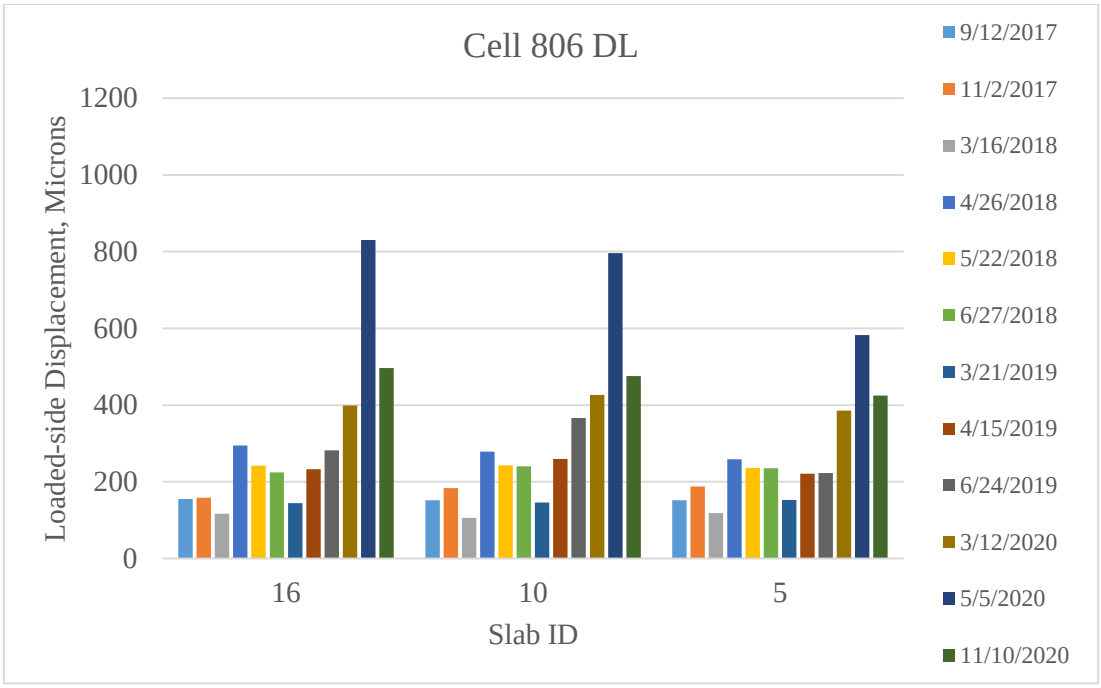

Figure 4-25. Loaded-side displacement of Cell 806 driving lane.

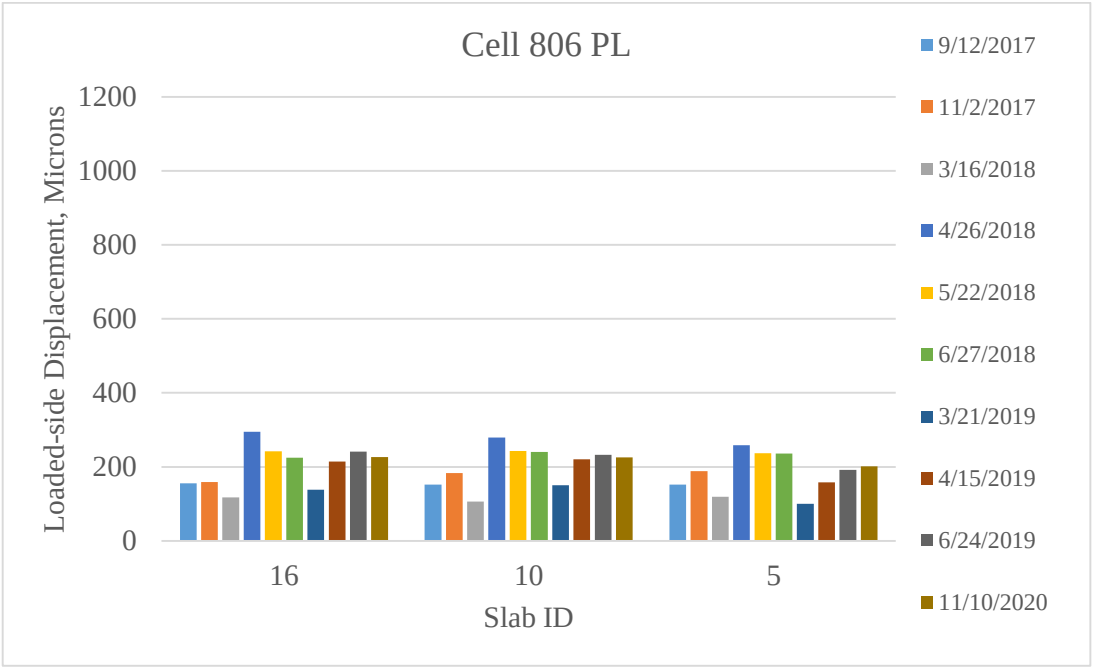

Figure 4-26. Loaded-side displacement of Cell 806 passing lane.

Figure 4-27 shows the loaded-side displacement vs ESAL for the test cells in driving lane. Just like LTE and differential displacement, this plot also shows that fibers are beneficial for better joint performance as the loaded-side displacement is less in the fiber reinforced cells

(Cell 606, 706 and 806) compared to the plain cement concrete cell (Cell 506). Cell 806 with maximum fiber dosage showed a trend of lowest loaded-side displacement throughout the study period.

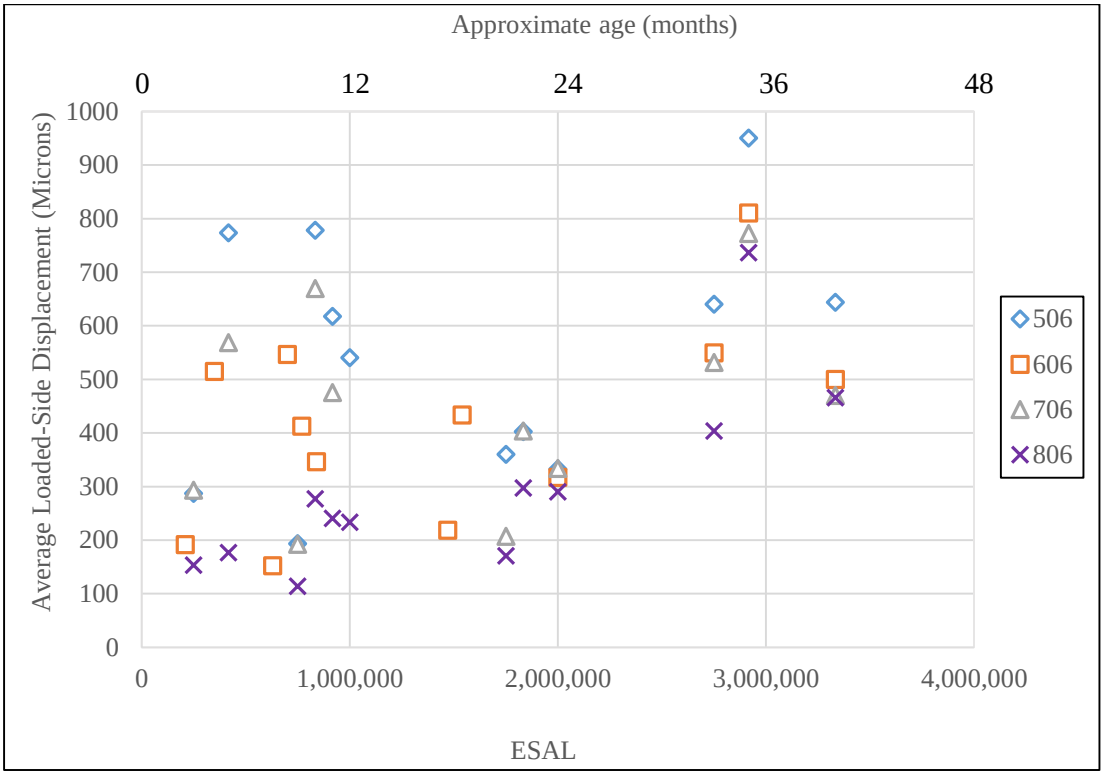

Figure 4-27. Average loaded-side displacement vs ESALs for the test cells in driving lane.

4.1.4. Presence of Voids Study under FRC Slab Panels

The procedure used for determining the presence of voids is presented in section 3.4.1. Figure 4-28 (a) and (b) compare the deflection vs. FWD applied load at a slab in Cell 506 (plain concrete cell) and Cell 806 (highest fiber dosage), respectively. Deflections were measured at different seasons for both the cells. While it appears that the deflection intercept determined for the spring-thaw times were relatively higher than the other seasons for both the cells, Cell 506 had higher values than Cell 806. Figure 4-29 summarizes the deflection intercept for all the thin MnROAD pavement cells (Cell 506-806) for various slab and test dates.

The comparison of Void Index (VI) values between Cells 506-806, as given in Table 4-1, indicates that the higher fiber volume in Cell 806 was able to significantly protect this cell from void (FWD detected) formation underneath the slab. The results for the Cells 506, 606

and 706 indicate that these cells seem to have significant FWD detected voids underneath their slabs. As a result, the LTE of these slabs were lower compared to Cell 806.

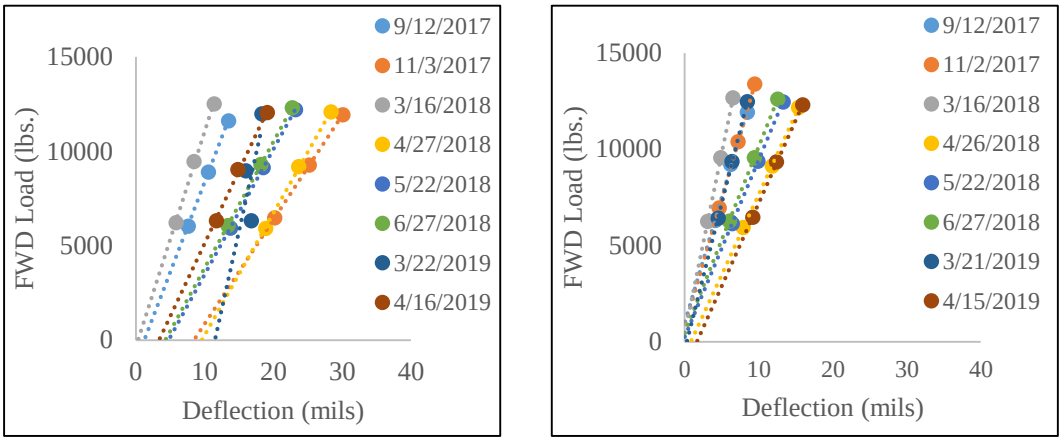

(a) (b)

Figure 4-28: FWD deflection vs load for (a) Cell 506 (b) Cell 806.

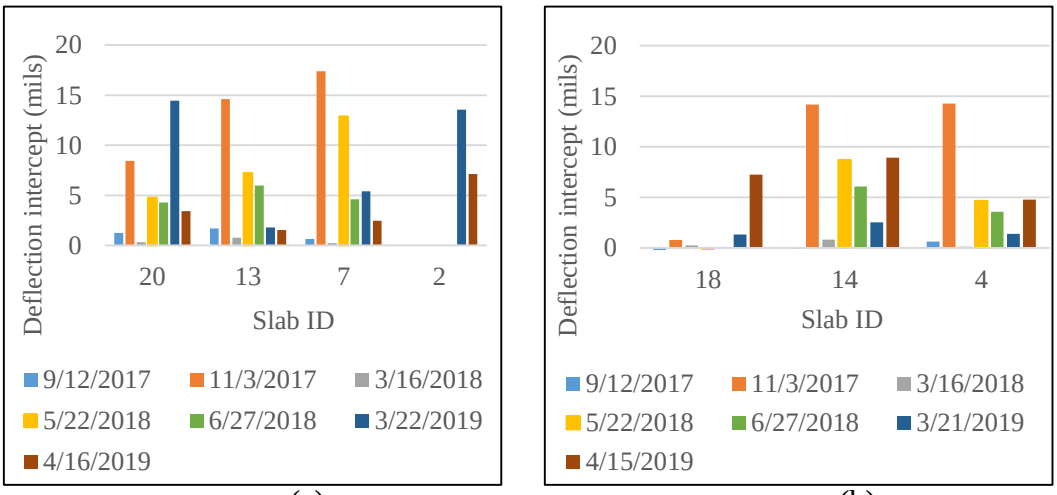

(a) (b)

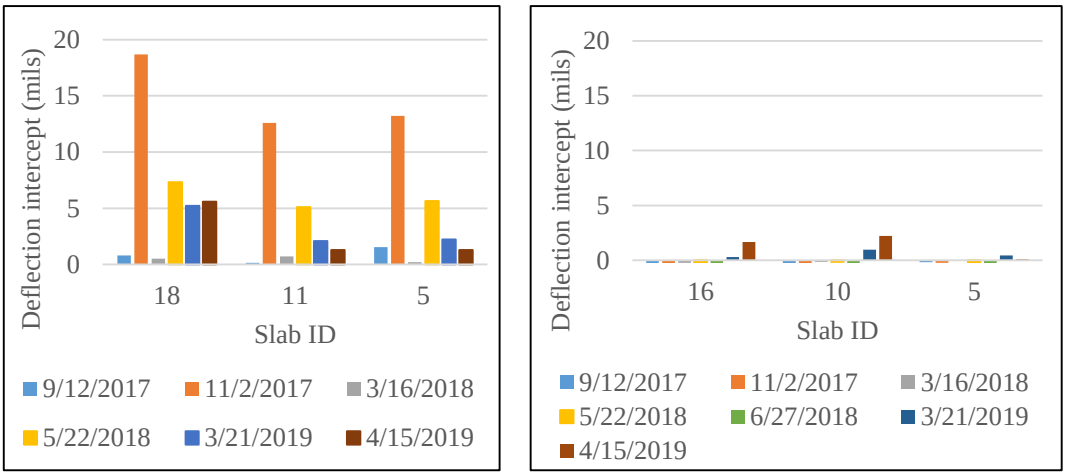

(c) (d)

Figure 4-29: Deflection values under variable FWD load stresses for test Cells (a) 506 (b) 606 (c) 706 and (d) 806.

Table 4-1: Void index values for different cells at different seasons.

	Void Index (VI) values				
Cell	Fall 2017	Spring 2018	Summer 2018	Fall 2018	Spring 2019
506	0	0	0	-	0
606	1	1	1	-	1
706	0	0	-	-	0
806	5	5	5	-	4

4.1.5. Pavement Temperature - LTE relationship

Figure 4-30 shows that the LTE measured for almost all the cells increased when the pavement surface temperature increased. It also shows the influence of fibers on the LTE vs. temperature relationship. Cell 806 experienced the least change in LTE with respect to temperature, indicating the contribution of fibers toward increasing load transfer through dowel action in the wider cracks at low temperatures. The fibers also increased the aggregate interlock by keeping the joints less wide. LTE variation was more pronounced for the Cell 506 (plain concrete). The slope of the LTE vs. temperature line for Cell 706 was also sharp, which indicates the greater influence of the temperature. The exact reason for Cell 706's low joint performance is not known; however, the data indicates that the joints considered for the FWD test probably experienced damages because of the higher loaded-side displacement,

differential displacement, and presence of voids underneath at very early age. The slope of Cell 606 is very similar to Cell 806. The reason behind this may be that the Cell 606 being 1 in. thicker, compensated the effect of higher fibers in Cell 806.

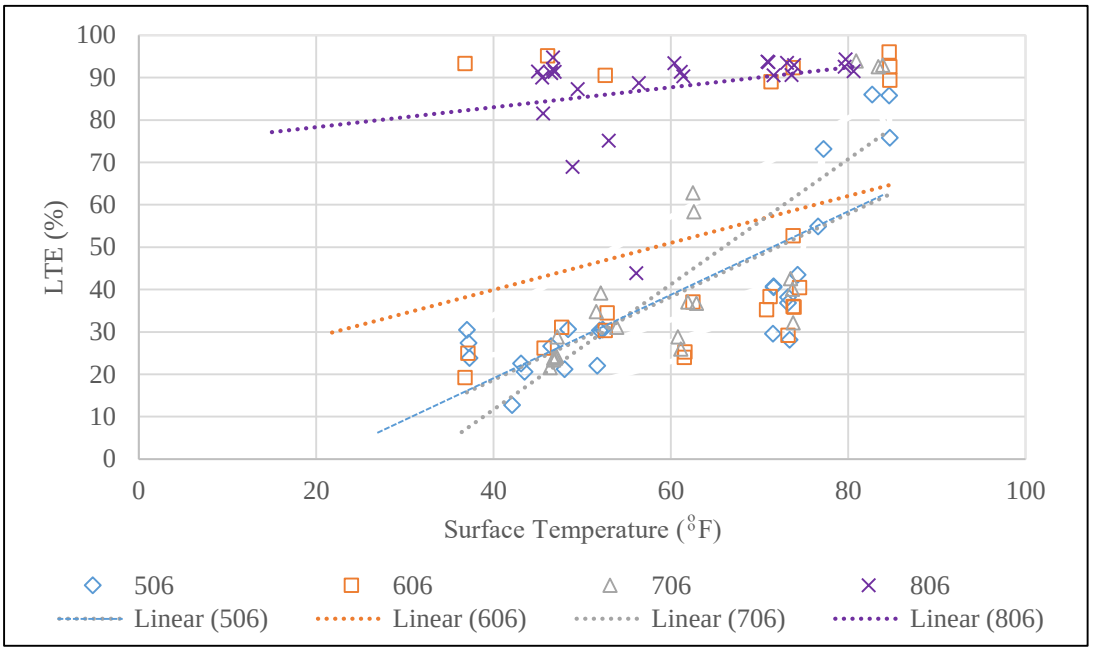

Figure 4-30: LTE vs. Pavement surface temperature for Cells 506, 606, 706 and 806.

4.2. Environmental Strain

Cells 506-806 had four VW sensors installed in each one of them. Two of the sensors were in the transverse direction in one slab and the other two in the longitudinal direction in an adjacent slab. Figure 4-31 through Figure 4-34 show the environmental strains computed for these cells, including the slab temperature. The strain values have showed a correlation with the slab temperature, and values were high during the winter months as anticipated. The longitudinal bottom sensor experienced the maximum amount of environmental strain for Cell 506. Cell 606 and 706 experienced less environmental strain overall. Cell 806 transverse and longitudinal top sensors experienced the maximum negative strain when compared with the other three cells.

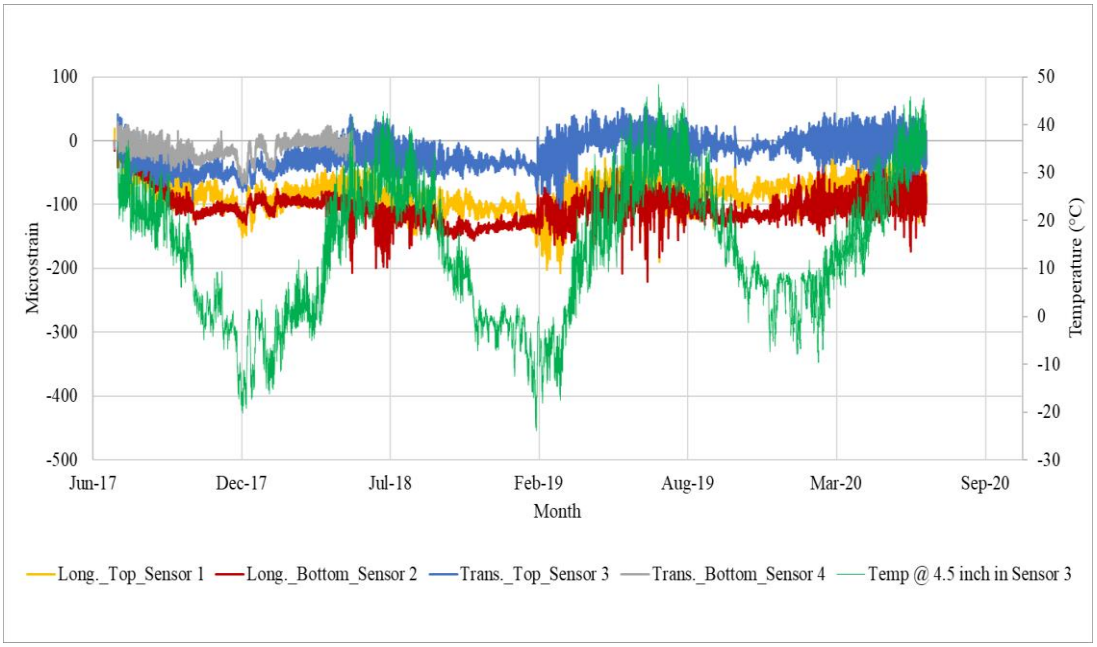

Figure 4-31: Environmental strains and slab temperature for Cell 506.

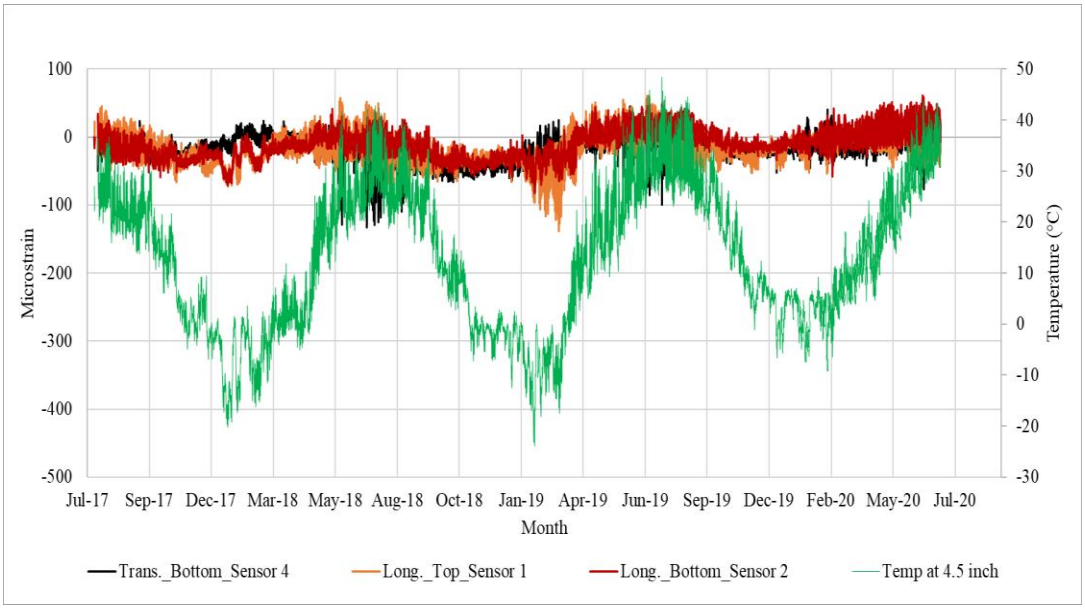

Figure 4-32: Environmental strains and slab temperature for Cell 606.

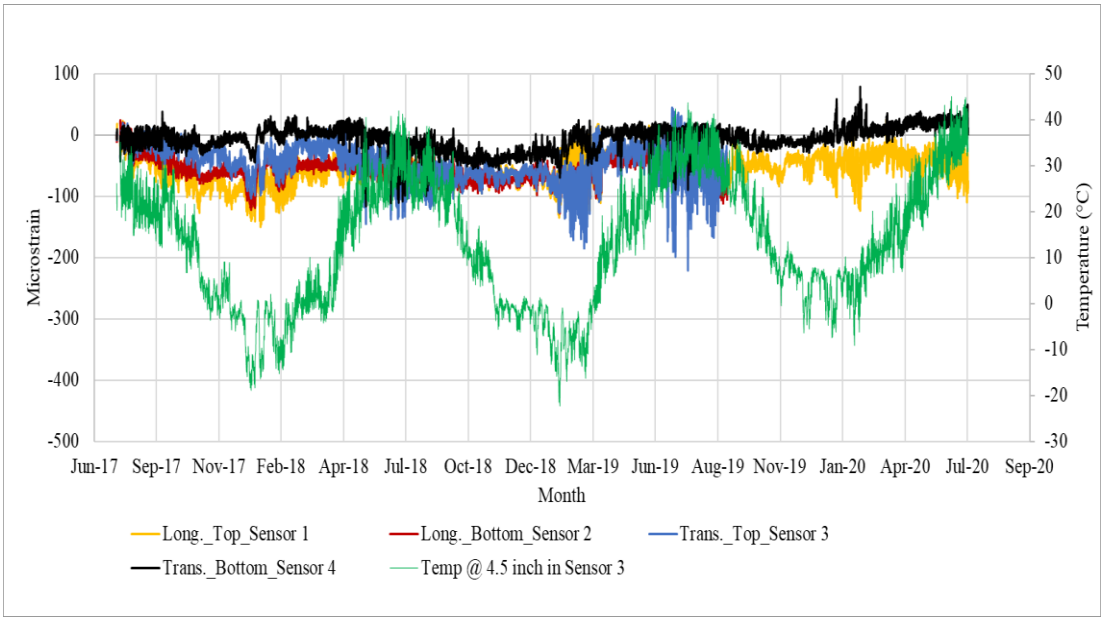

Figure 4-33: Environmental strains and slab temperature for Cell 706.

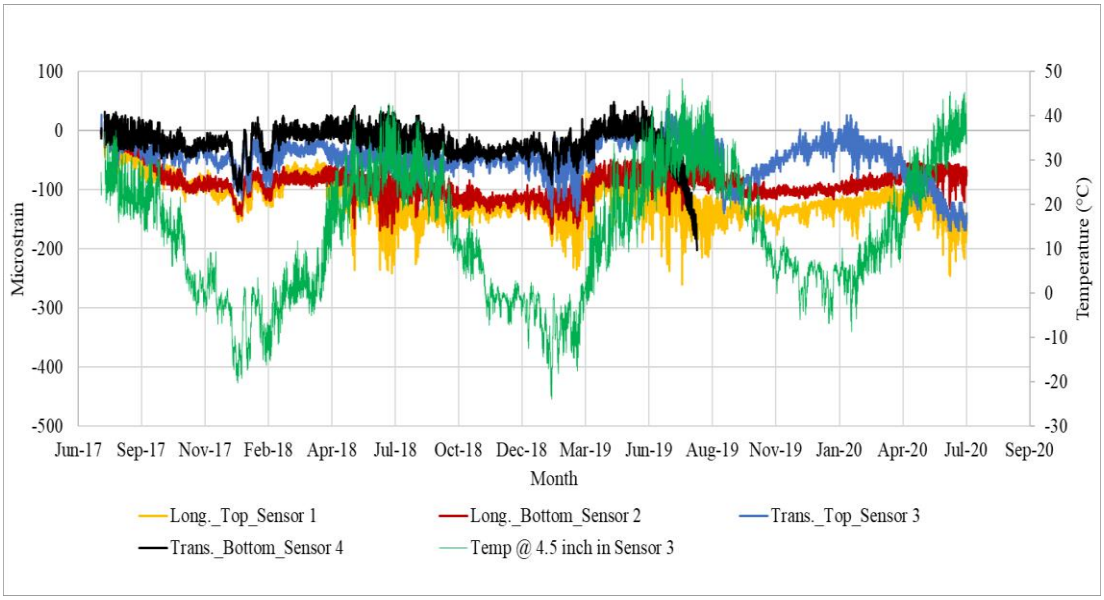

Figure 4-34: Environmental strains and slab temperature for Cell 806.

4.3. Slab Curvature

The slab curvatures for Cells 506-806 were computed using the above mentioned environmental starins employing the (Equation 2) as described in section 2.6. Figure 4-35 to Figure 4-38 show the slab curvature of the test cells for the three year service period.

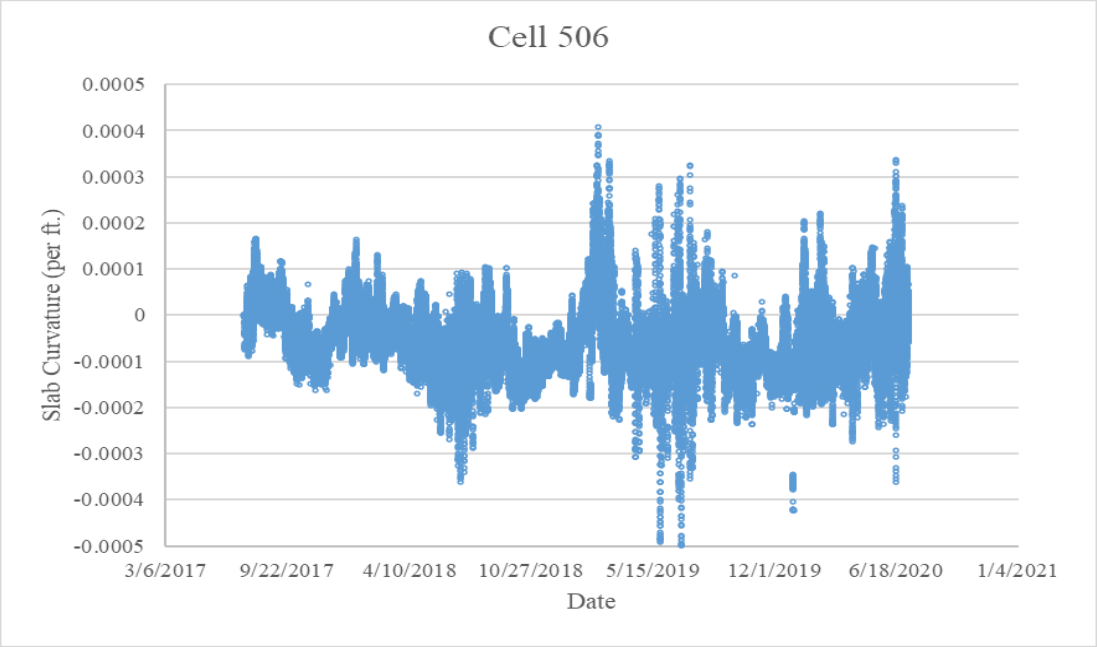

Figure 4-35: Seasonal variation of slab curvature for Cell 506.

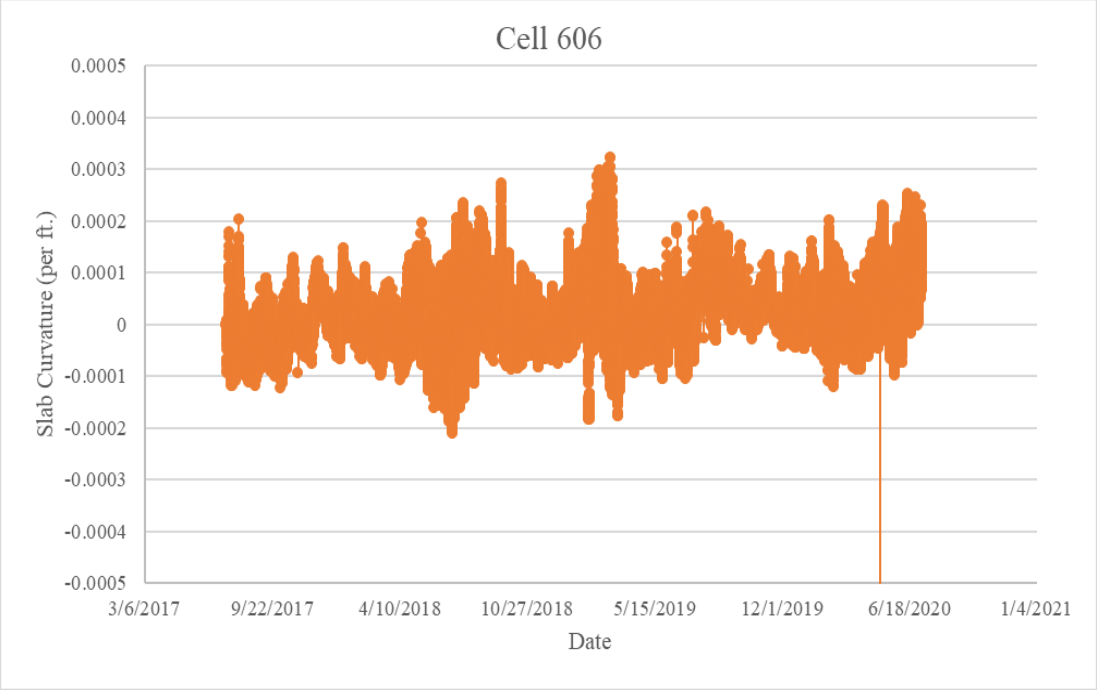

Figure 4-36: Seasonal variation of slab curvature for Cell 606.

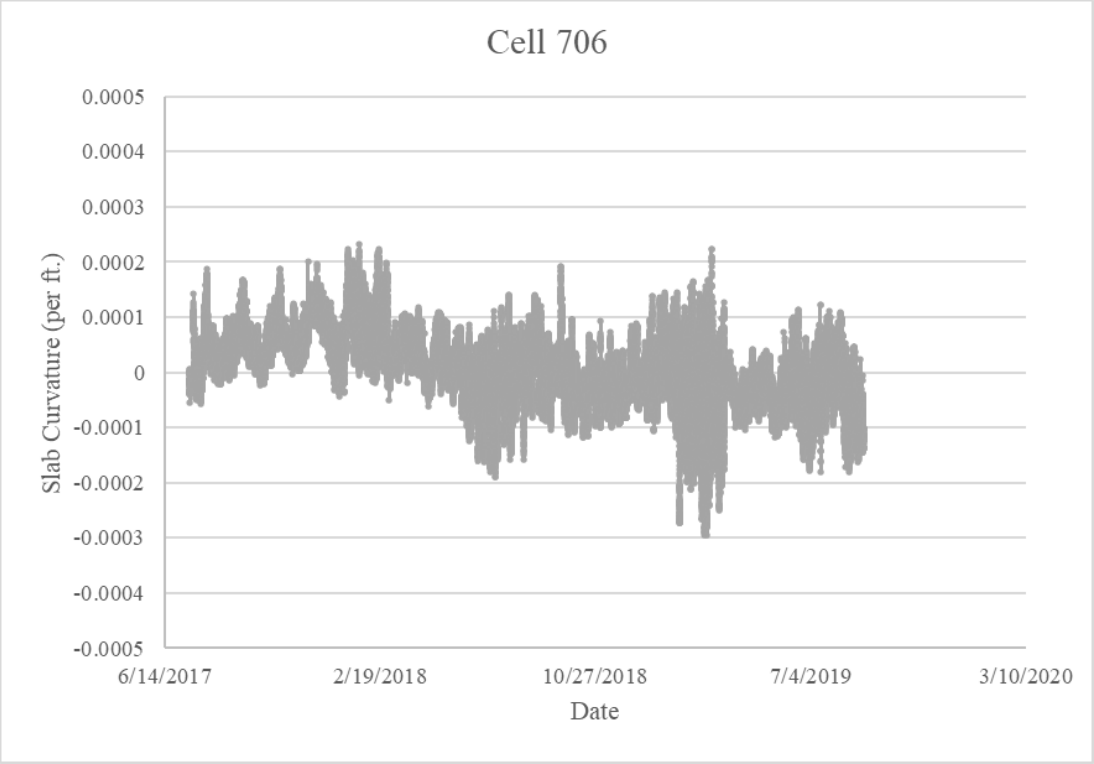

Figure 4-37: Seasonal variation of slab curvature for Cell 706.

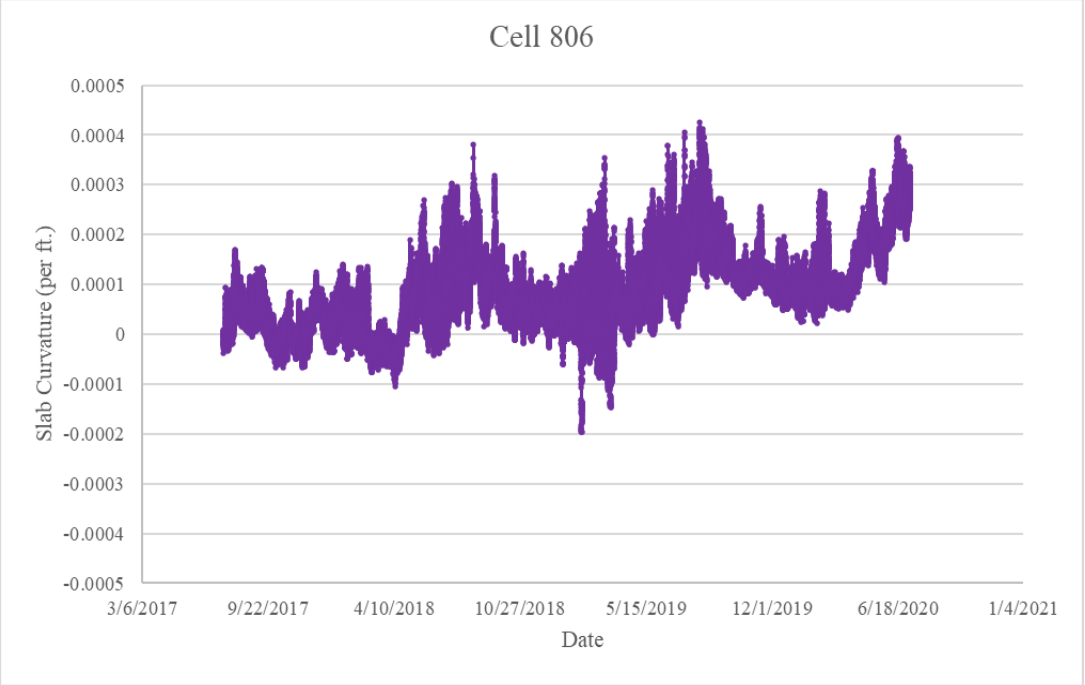

Figure 4-38: Seasonal variation of slab curvature for Cell 806.

Cell 506 recorded maximum positive (upward) slab curvature of 0.00041/ft during the winter of 2018 and the maximum negative (downward) slab curvature of -0.0005/ft during the summer of 2019. This observation is justified because cold winter nights are supposed to create greater upward slab curvature and warm summer days will result in downward slab curvature.

Cell 606 recorded maximum positive (upward) slab curvature of 0.00032/ft. during the winter of 2018 or early 2019 and the maximum negative (downward) slab curvature of -0.00022/ft. during the summer of 2018. Cell 706 recorded maximum positive curvature of 0.00023/ft. during the winter of 2017 and the maximum negative curvature of -0.0003/ft. during the summer of 2019. Cell 806 observed the maximum positive and negative slab curvatures of 0.00043/ft. and -0.0002/ft. during the winter and spring of 2019 respectively.

Daily and seasonal temperature variation causes slab curling/warping. Comparing the curvature plots among Cells 506-806, it may be noted that as the fiber dosage increased from Cell 506 (no fiber) to Cell 806 (11.66 lbs. of fiber/cy of concrete), the daily variation of slab curvature decreased. In other words, fiber dosage showed an inverse relationship with environmental strain induced slab curvature. For this study, the effects of built-in curl and moisture gradient on slab curvature was not considered. As a result, any strong conclusion may not be drawn at this stage and further analysis is required. Having said that, it should be noted that the macro-fibers used in this study probably affected the rate of change of slab curvature with daily and seasonal temperature variation. The fibers seem to have provided restrain to the slab curling due to temperature which is clear when compared between the slab curvature plots for non fiber Cell 506 and FRC cells. Less slab curvature results in reduced pavement stress, pavement unevenness and hence less discomfort to road users.

4.3.1. LTE - Slab Curvature Relationship

Figure 4-39 shows the LTE vs. slab curvature relationship for the test cells. The slab curvatures only for the dates and times of the FWD tests were included for this analysis. Figure 4-39 shows that Cell 806, having the highest fiber dosage of all the test cells, underwent the least variation in slab curvature. It also consistently exhibited the highest LTE among all the test cells. On the other hand, Cell 506 (no fiber) experienced the largest variation in slab curvature and also the LTE was very low. This plot is a good indication that the macro-fibers in the test cells helped in limiting the slab curvature, resulting in better joint performance, or vice-versa.

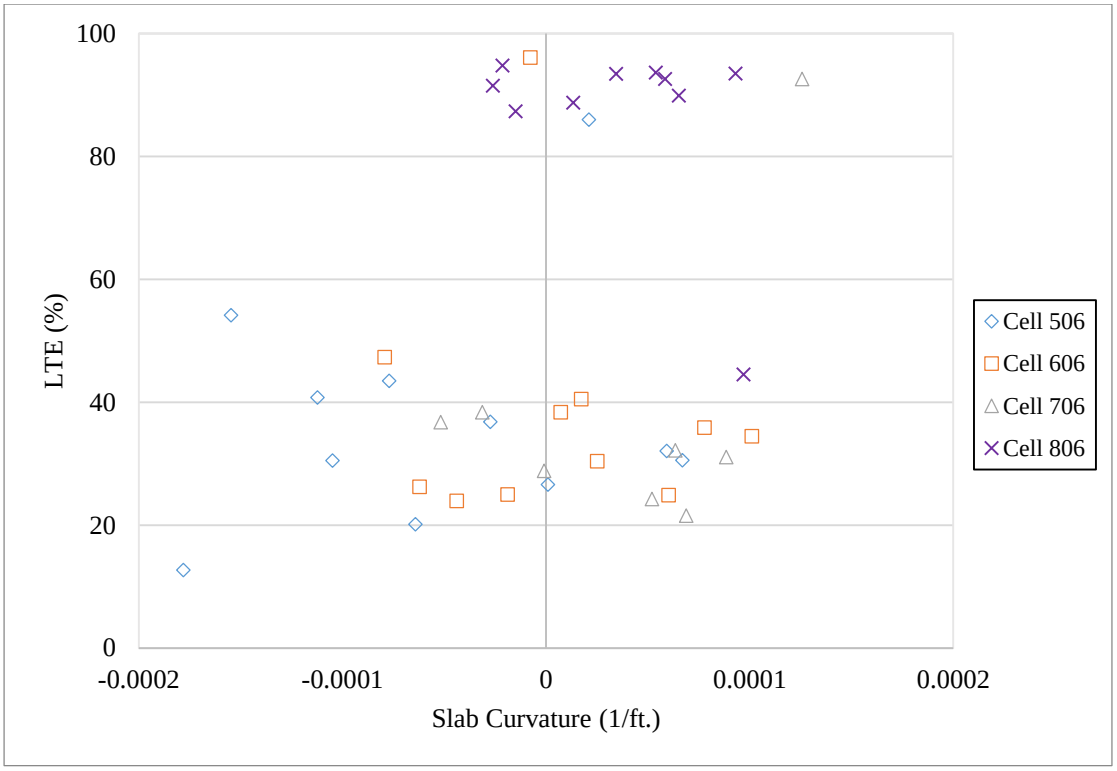

Figure 4-39: LTE vs slab curvature for the test cells.

4.3.2. Displacement – Slab Curvature Relationship

The slab curvature result also explains the reason for more voids in Cell 506, 606 and 706 and the least probability of voids in Cell 806 as reported in section 4.1.4. Figure 4-40 shows the relationship between the deflection under the test cells and slab curvature variation; the strain data and the FWD data used for the analysis were collected at the same time. Loaded-side displacement values along the wheel path were used as the deflection values for this plot. As can be seen in this figure, greater curvatures in the Cells 506, 606, and 706 is related to higher deflections in each of those cells. The less variation in slab curvatures in Cell 806 agree with the lower deflections in this cell. Based on the abovementioned observations, it may be stated that the higher curvatures in Cells 506, 606 and 706 might have been influenced by the values of deflections in those cells, which was responsible for more voids underneath these cells, as reported in Figure 4-28 and Figure 4-29. Hence, it can be said that higher fiber dosage in Cell 806 helped keeping the variation in slab curvatures low and also resulted in less slab deflections. As a result, this cell also witnessed least probability of voids among all the test cells as discussed earlier in section 4.1.4.

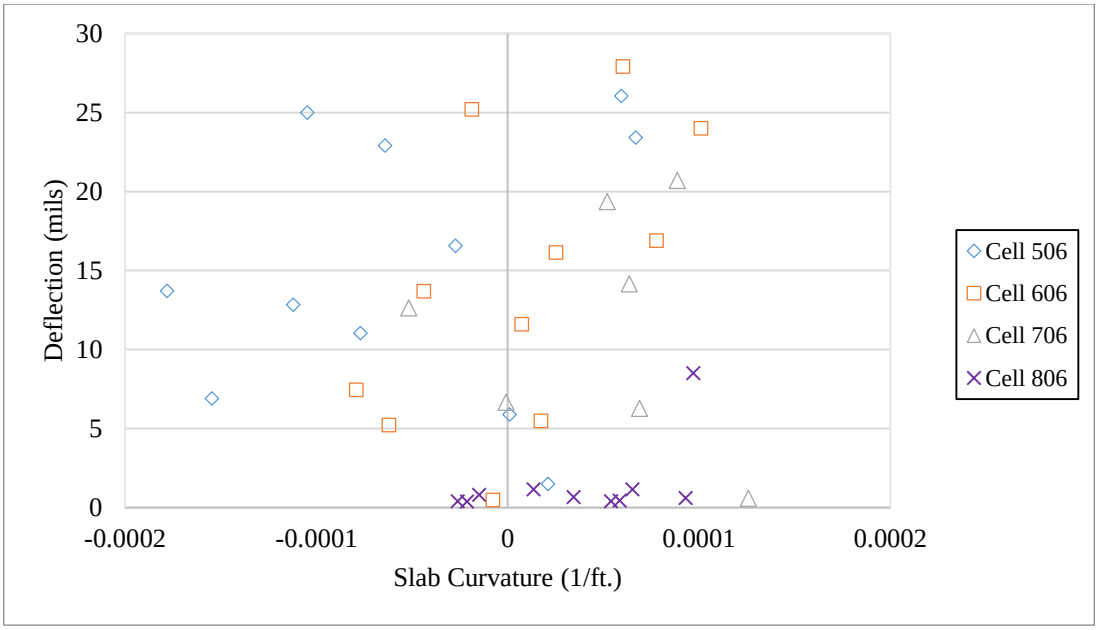

Figure 4-40: Deflection vs slab curvature for the test cells.

4.4. Summary

This chapter discussed the results related to pavement structural responses. The joint performance results indicated a clear benefit of synthetic macro-fiber reinforcement in thin concrete pavements. Comparison between plain concrete test cell (Cell 506) and FRC test cells (Cell 606, 706 and 806) showed that addition of fibers helped in improving load transfer for an extended service life of thin concrete pavements. It also showed lower differential displacement and loaded-side displacement as the fiber volume increased in the concrete mix. Next, it was also found that as the fiber dosage increased, the chances of voids present under the thin concrete pavement slab reduced. Highly fiber reinforced test cells also showed less variation in LTE when exposed to daily and seasonal temperature difference. It was also observed that the maximum positive strain was measured at the longitudinal bottom sensor of the non-FRC Cell 506. This strain maybe responsible for bottom-up cracks in future with considerable amount of traffic load. The environmental strain values were utilized to plot slab curvature data with respect to time for the test cells. As expected, higher dosage of fibers resulted in less daily and seasonal variation of slab curvature. In response to this observation, a relationship between the slab curvature and LTE of the test cells was established. It was evident from this study that higher dosage of fibers, as observed in Cell 806 resulted in less variation in daily and seasonal slab curvature which in turn helped to keep the LTE high for an extended period of pavement service life.

5. Transverse Joint Faulting and Fatigue Cracking

In this chapter, the transverse joint faulting and fatigue crack data analysis results are discussed. Furthermore, a transverse joint faulting prediction equation is proposed based on the MnROAD FRC test cells' data (Cell 506-806). Next, faulting index is computed for the test cells and analysed with respect to pavement roughness parameter IRI (International Roughness Index). Finally, fatigue crack percentage was plotted with respect to ESALs for the test cells.

5.1. Joint Faulting – Age

Figure 5-1 shows the faulting data from the spring of 2018, until spring of 2020. Data collected throughout this above-mentioned time shows that Cell 506 (no fiber) reported the highest faulting consistently, whereas, Cell 806 (maximum fiber dosage) showed the lowest overall joint faulting. Cell 706 having more fiber dosage compared to Cell 606, occasionally showed more faulting than Cell 606 but it should be noted that Cell 606 was 1 in. thicker than Cell 706. Also, it may be reiterated that any faultmeter readings less than 0.04 in. (1 mm) was not considered as the notable joint faulting. As a result, from Figure 5-1, it can be said that the FRC cells (Cell 606-806) did not show considerable joint faulting until the spring of 2019. This could also be a result of delayed joint deployment in some of the transverse joints.

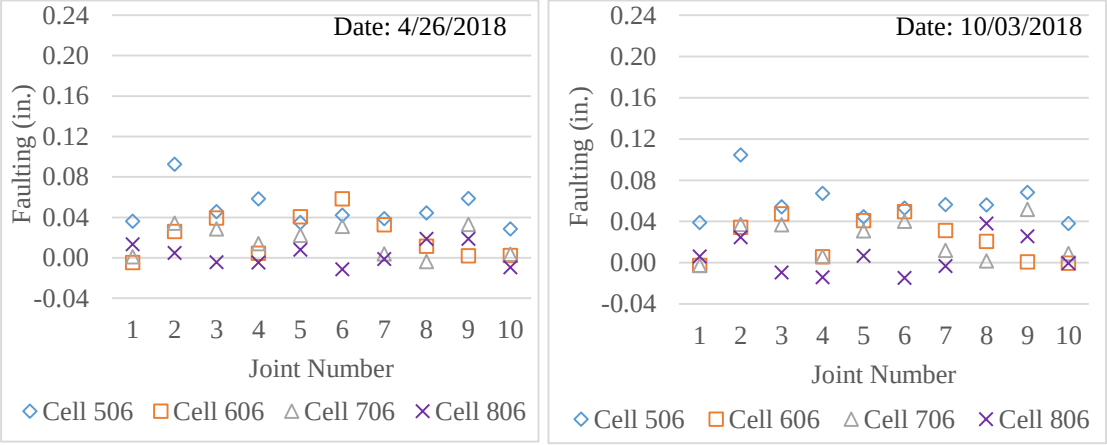

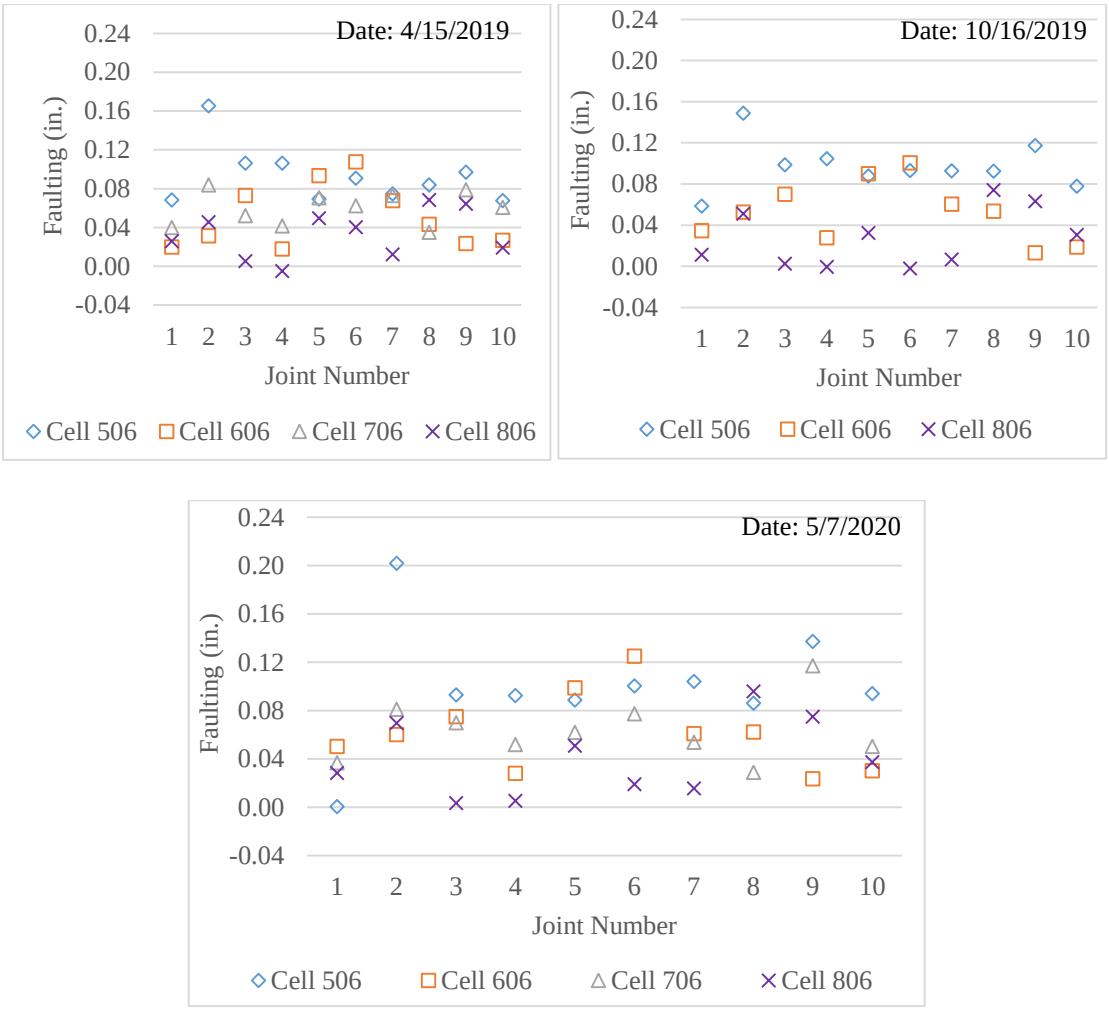

Figure 5-1: Faulting summary of Cells 506 through 806 until May, 2020.

5.2. Joint Faulting – ESAL

As mentioned earlier, Cells 506 to 806 were constructed on the high traffic volume segment of MnROAD, which consists of two lanes running parallel to the original westbound interstate highway I-94. Figure 5-2 shows the variation of average faulting for Cells 506 to 806 with respect to ESAL. This figure also shows the significant contribution of fibers in Cell 806. The sudden increase of faulting at 1.8 million ESALs (during spring 2019) for all the thinner cells indicates a weakening of the joint conditions during the springtime when the underlying layers were relatively weak. There is no significant difference between the measured average faulting values for Cell 606 and 706. This might be reasonable because even though Cell 706 (5-in.) is one in. thinner than Cell 606 (6-in.); it contains 3 lbs./cy more fibers than Cell 606. Also, the residual strength of Cell 606 concrete is lower at 124.16 psi compared to 156.4 psi for the Cell 706.

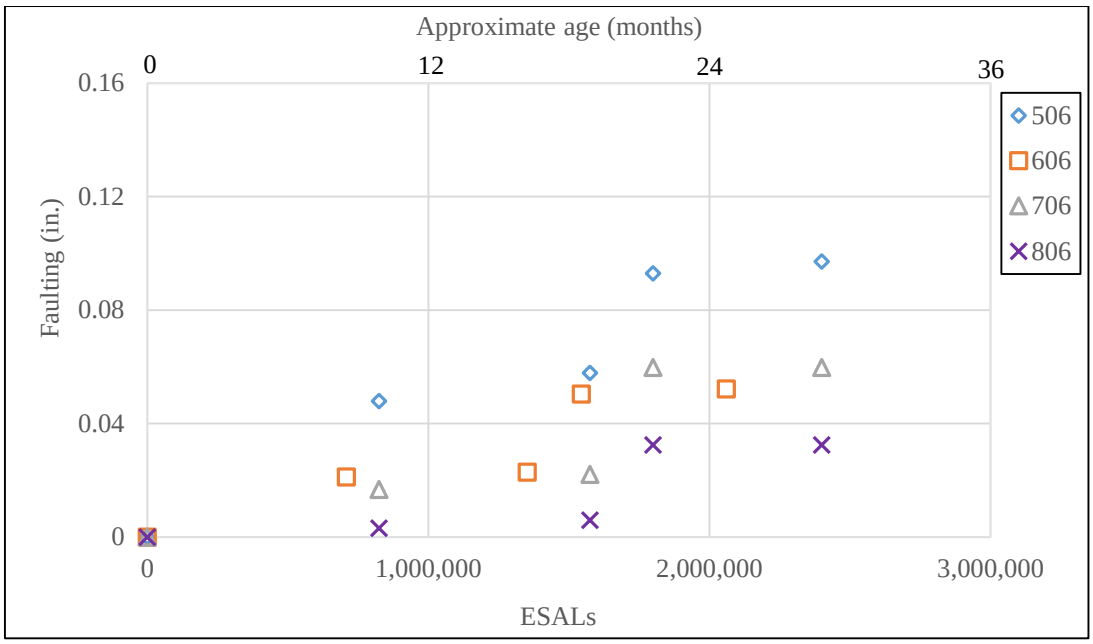

Figure 5-2: Faulting vs. ESALs for cells 506, 606, 706, and 806.

5.3. Faulting Prediction Equation

Faulting data for all four test cells under consideration (Cell 506-806) were collected and used to develop a suitable faulting prediction equation. Statistical software Minitab 2019 was used to develop the equation. Numerous trial equations were developed and validated to finally find the best prediction equation for the present faulting data and field conditions at MnROAD. The proposed faulting prediction equation is as follows:

$$FAULT = ESAL^{0.54} * (A + B * h + C * RS + D * k_{comb}) \quad \text{(Equation 5)}$$

Where,

FAULT = Predicted faulting, in.

ESAL = Equivalent number of 18-kip standard axles

h = Slab thickness, in.

RS. = Residual strength of concrete, psi.

k_{comb} = Combined modulus of subgrade reaction, psi/in.

A, B, C, and D are parametric constants; A= 0.000055, B= -0.0000033, C = -0.000000096, and D= -0.0000000107. The R^2 and SSE for this equation is 0.9117 and 0.0019 in., respectively. The one tailed p-value for ESAL, slab thickness, RS, and k_{comb} were 1.8E-8, 2.4E-37, 7.8E-8, and 8.4E-17 respectively. This indicated that the variables considered were statistically significant (p less than or equal to 0.05). Figure 5-3 (a) shows the comparison between the Equation 2 predicted and measured faulting values for thin pavement cells (Cells 506 - 806). Figure 5-3 (b) shows the predictability of (Equation 5).

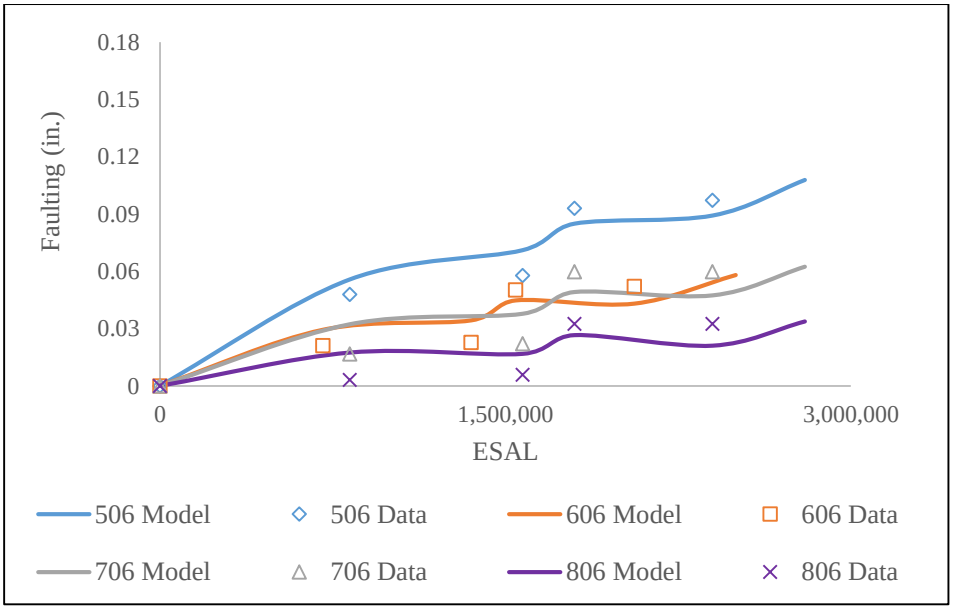

(a)

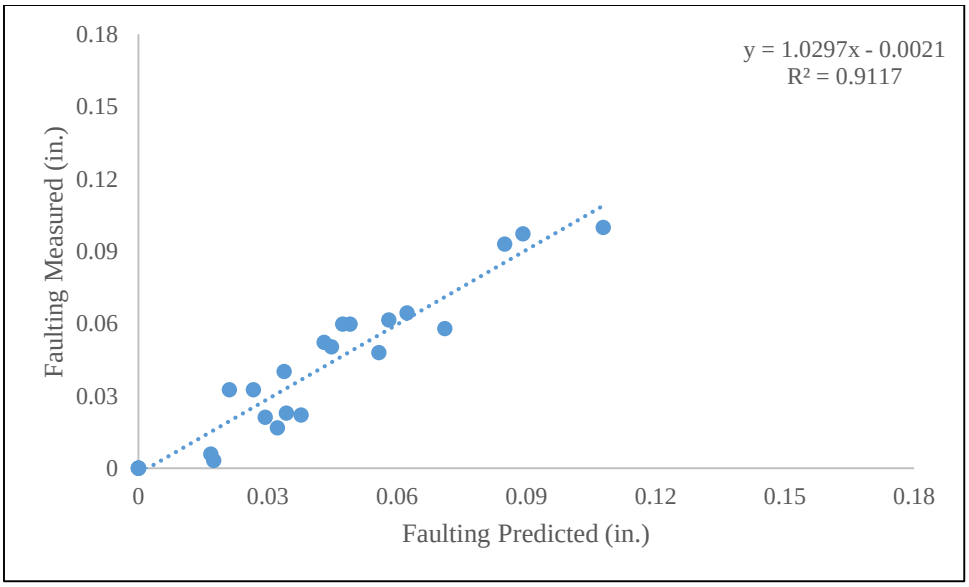

(b)

Figure 5-3: (a) Comparison of the measured faulting and predicted faulting, (b) Predictability of the proposed faulting prediction equation.

5.3.1. Validation of the Faulting Prediction Equation

The proposed faulting prediction equation was validated with the final faulting data set, recorded in May 2020. This set of data was not used in the statistical relationship development. Figure 5-4 shows the validation results for the prediction equation.

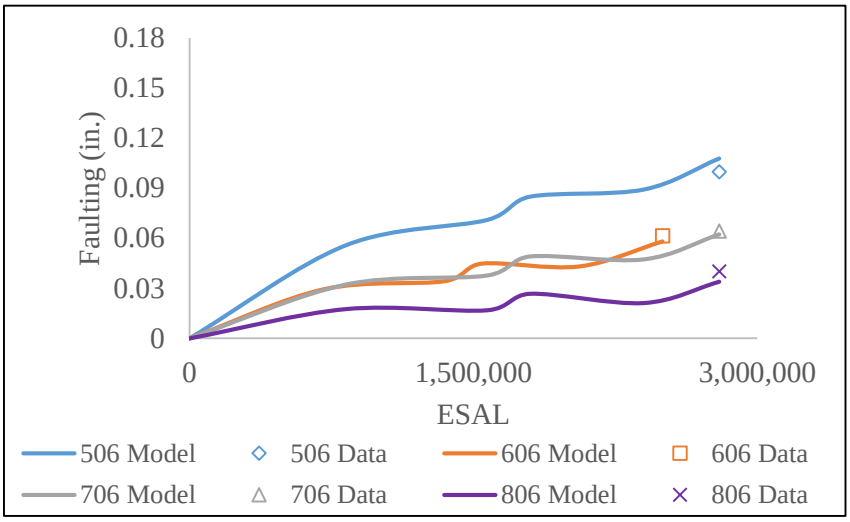

Figure 5-4: Validation of the proposed faulting prediction equation for the test cells.

5.4. Faulting Index and Pavement Roughness (IRI)

Figure 5-5 and Figure 5-6 show the comparison of Faulting Index (defined in section 3.5.2) for driving lane and passing lane, respectively for Cells 506 through 806. As expected, the FI for driving lane was relatively higher than passing lane overall. Figure 5-5 shows that Cell 506 (no fiber) and Cell 806 (maximum fiber) experienced the highest and lowest FI values, respectively, throughout the years 2018 to 2020. The same trend was observed for the passing lane as well. Cell 506 had the maximum reported FI of appx. 7.5 in. which was almost 2.5 times higher than Cell 806 in the spring of 2020. Cell 606 and Cell 706 fell in between with the former having 5 lbs./cy fiber dosage but 6 in. thickness and the later having 8 lbs./cy fiber dosage but 5 in. thickness. Overall observation indicated that higher dosage of fibers resulted in less FI.

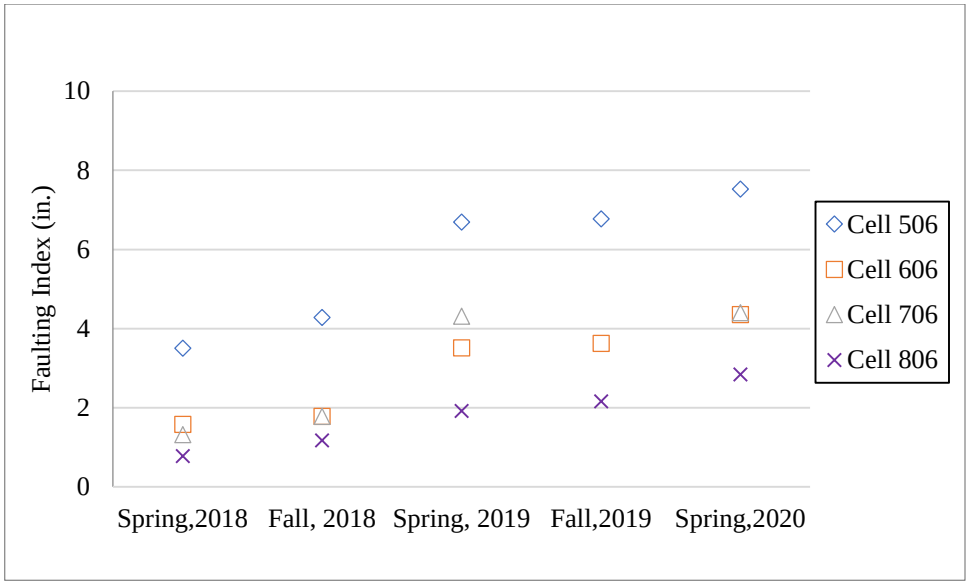

Figure 5-5: Comparison of faulting index for the driving lane of the test cells.

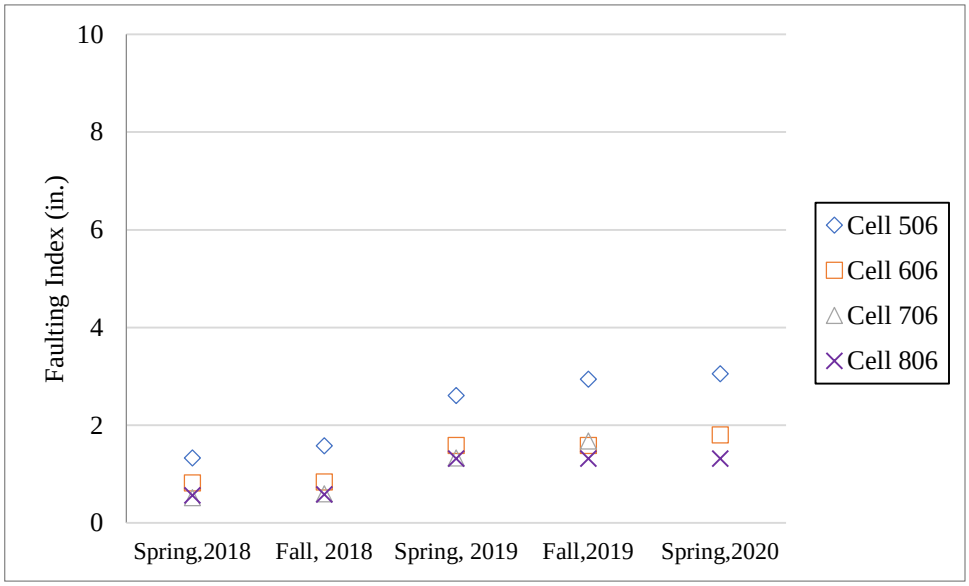

Figure 5-6: Comparison of faulting index for the passing lane of the test cells.

Figure 5-7 shows the variation of FI/mile with respect to ESAL for all the test cells. FI/mile was defined in section 3.5.2. and was introduced to draw a relationship between FI and IRI. Figure 5-7 shows that as the ESAL for all the four cells increased, the FI/mile increased as well. Cell 506 with no fiber showed maximum FI/mile with respect to ESAL whereas Cell 806 with maximum fiber dosage showed minimum FI/mile w.r.t ESALs. The occasional

jumps in the data at 1.5 million ESALs and 2.5 million ESALs was believed to be a result of the spring-thaw season and a weaker base resulting of that.

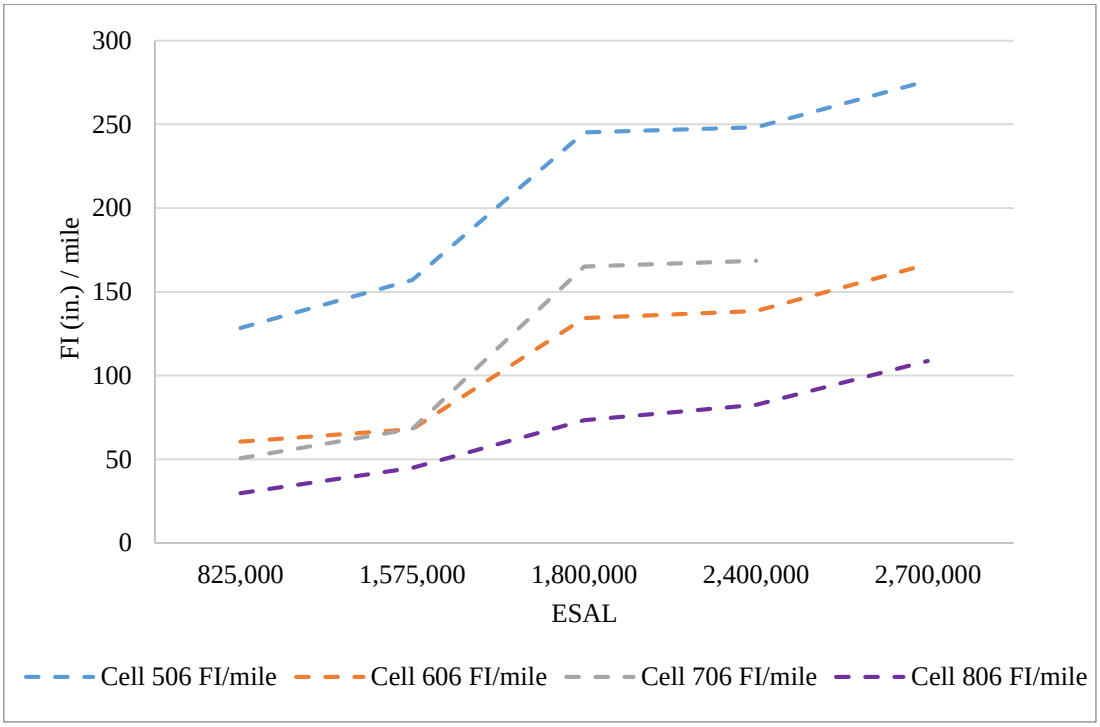

Figure 5-7: Variation of faulting index per mile with respect to ESALs for the test cells.

Figure 5-8 shows the variation of IRI with respect to ESAL for all the four test cells. Cell 506 having no fibers showed higher IRI values consistently. Cells 606, 706 and 806 showed lower IRI values compared to Cell 506. In the year 2018, at 825,000 ESALs, the IRI value for Cell 506 was 180 in. /mile which was already in the range of poor RQI rating. At the same time and same ESAL count, Cell 806 having maximum fiber dosage was having an IRI value of 139 in./mile which was well within the fair RQI rating. However, after 2.4 million ESALs, Cell 806 also reported poor RQI rating. This suggests that thin concrete pavements having fiber reinforcement helps keeping the pavement roughness within an acceptable range for a given repetition of traffic load unlike non-fiber reinforced thin concrete pavements.

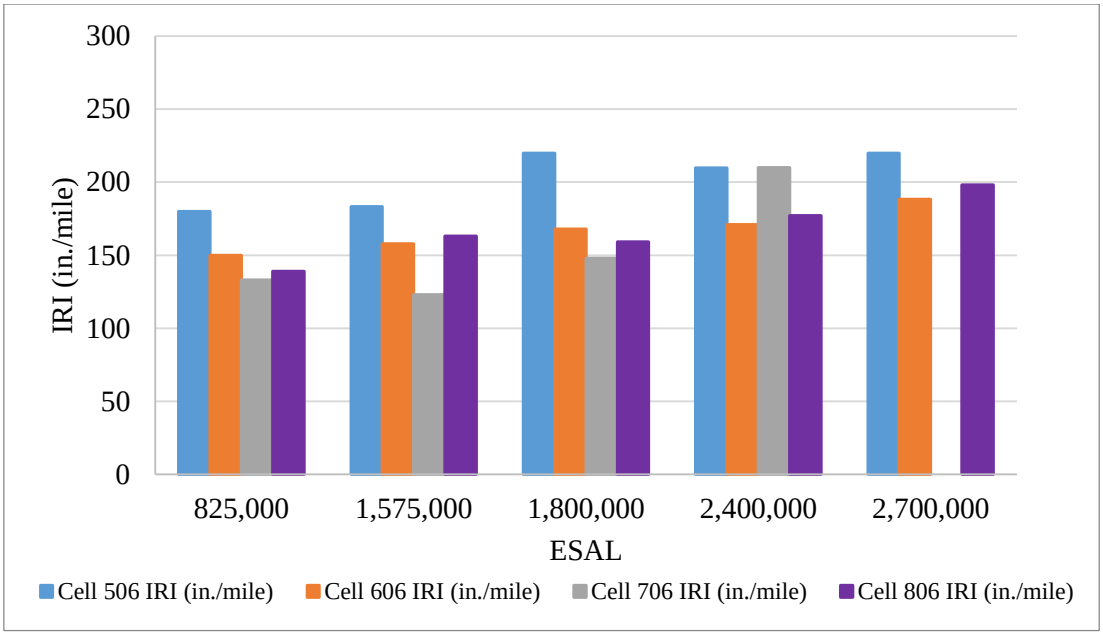

Figure 5-8: Variation of International Roughness Index (IRI) with respect to ESAL.

Figure 5-9 shows the IRI and FI/mile with respect to ESALs for the test cells. It can be seen that with increasing ESAL, as FI/mile increases, the pavement roughness parameter IRI also increases. The overall trend of the available data shows that there is a certain relationship between FI/mile and IRI. In other words, as the faulting increases in thin test cells, the IRI or pavement roughness also increases. Also it should be noted that due to the smaller dimension (6 ft. x 6 ft.) of the test cells, compared to the conventional concrete pavement slabs, the influence of faulting maybe higher on the pavement roughness. Figure 5-10 shows the relationship between FI/mile and IRI for the Cells 506-806. An R^2 value of 0.67 suggests that there is moderate correlation between pavement roughness (IRI) and transverse joint faulting (FI/mile).

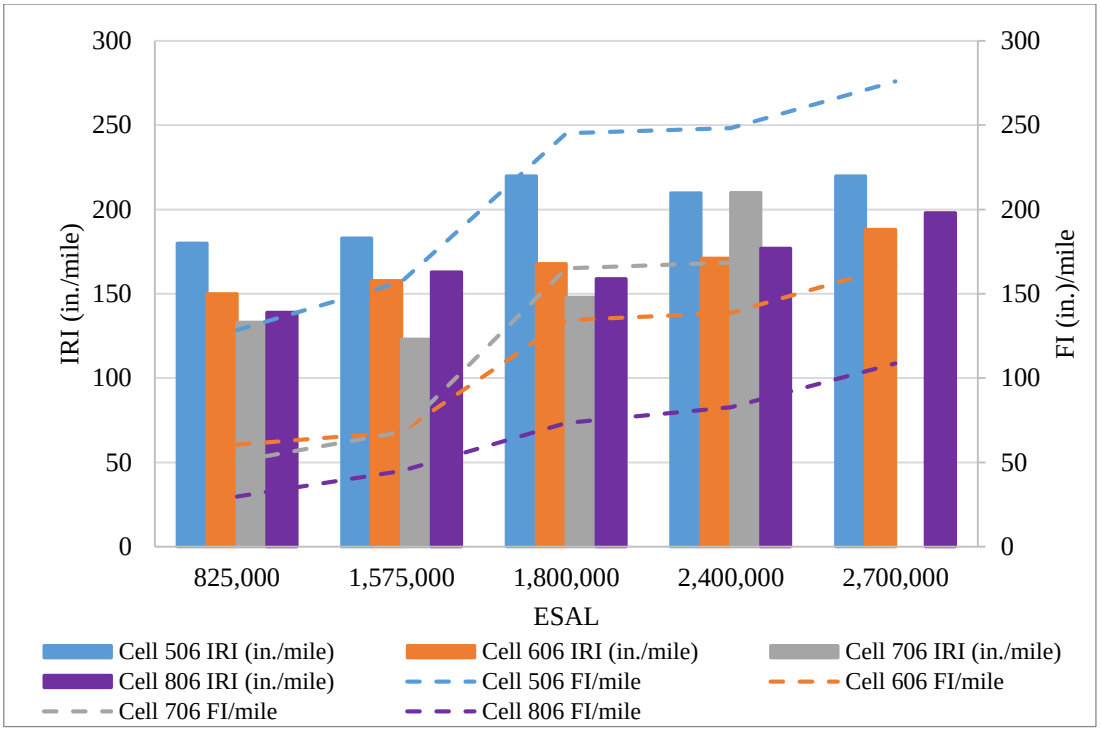

Figure 5-9: Variation of International Roughness Index (IRI) and Cumulative Faulting Index with respect to ESAL.

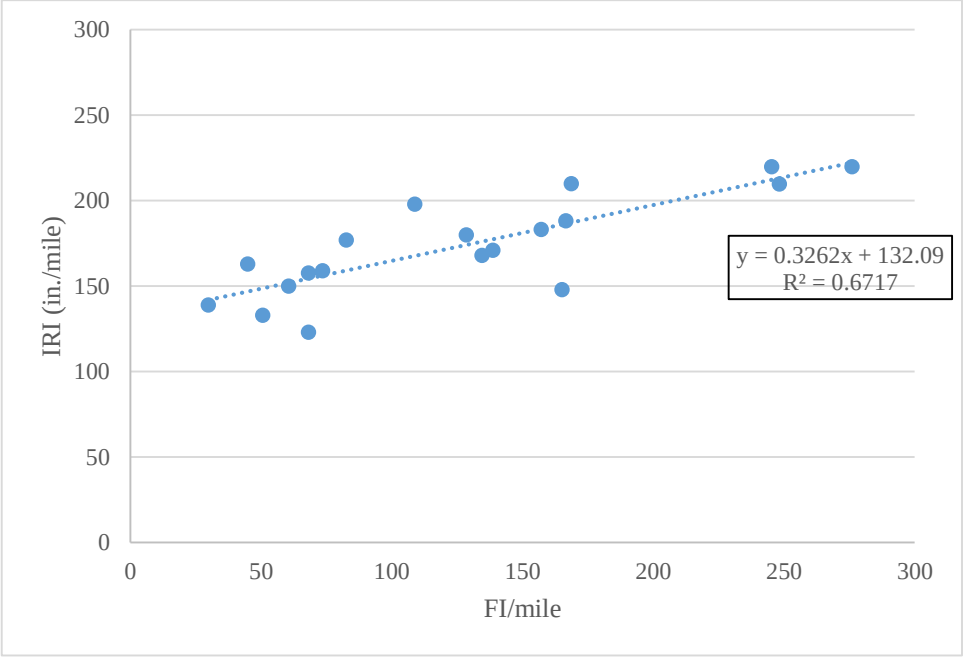

Figure 5-10: Relationship between IRI and FI/mile.

5.5. Fatigue Cracking

Crack survey was periodically conducted by MnDOT using pavement distress survey sheets, which were then used to generate consolidated color-coded distress maps. Cell 506, which was the control cell (no fibers), experienced transverse and diagonal cracks in some slabs. Figure 5-11 shows a photograph of three distressed slabs of Cell 506 before they were replaced in June 2020. Figure 5-12 shows the color-coded distress maps for Cells 506 and 606. Cells 706 and 806 did not show any visible crack and hence not showed in this thesis.

Figure 5-11: Cracks observed in Cell 506 (replaced in the summer of 2020).

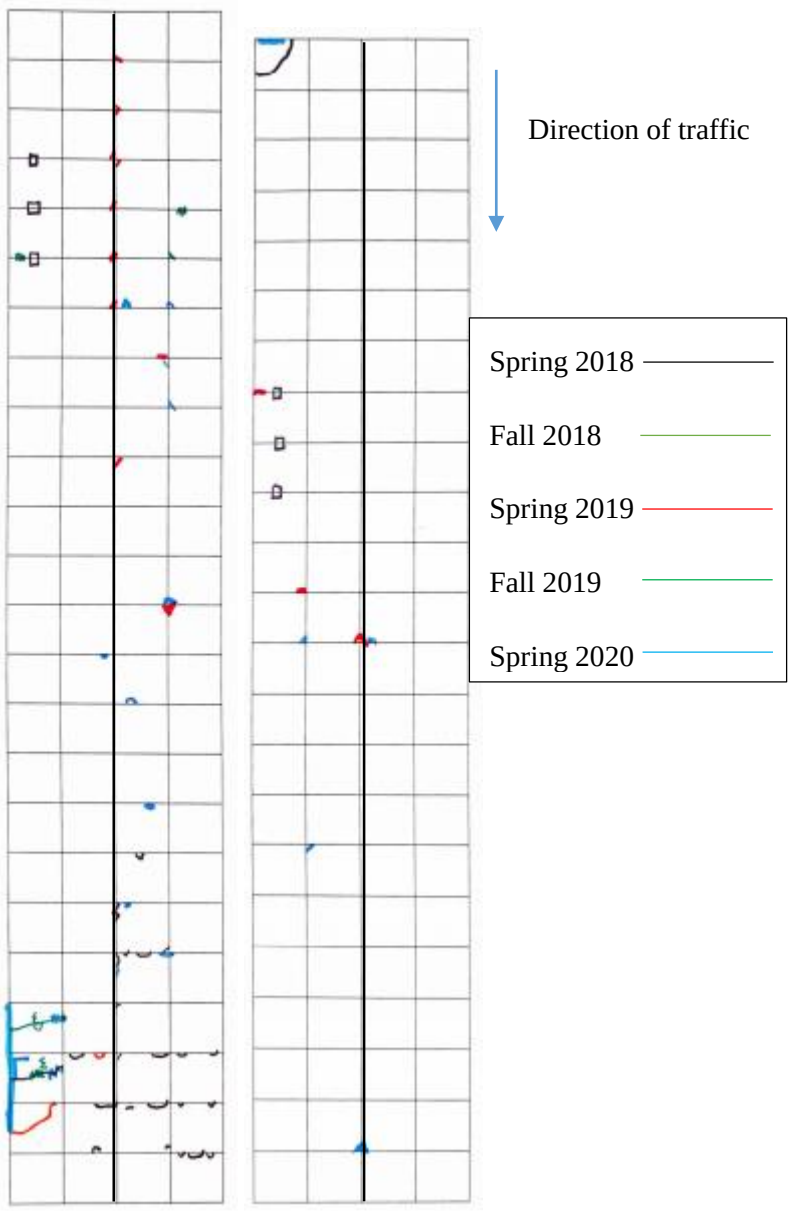

Figure 5-12: Distress Maps (a) Cell 506 (b) Cell 606.

Cell 506 experienced the maximum number of cracks among all the test cells. Most of the diagoanal and transverse cracks were observed in the driving lane whereas passing lane which was exposed to environmental loads did not develop transverse or corner cracks but a significant number of joint spalling was observed. Cell 606, which was constructed with 5 lbs./cy (20% residual strength) of fibers and 6 in. thickness, experienced one corner crack

prior to April 2018. The severity of that crack did not change with age and ESALs. This crack is also located in the last panel next to a cell transition joint, so it can be assumed that this crack is not a typical fatigue-related crack and it occurred because of a construction issue. The distress survey conducted on March 2020 found one joint spalling and two additional low severity corner cracks in this cell which again is negligible compared to the number of joint spalling and corner cracks in the plain cement concrete Cell 506. Cells 706 and 806, which were constructed with fiber dosages of 8 and 11.66 lbs./cy, respectively, did not experience any crack until March 2020 except for a couple of narrow cracks in Cell 806 that originated at the location of a joint opening sensor. Figure 5-12 shows that 5-in. thick Cell 506 with no fibers experienced fatigue cracks but 6-in. thick Cell 606 (with 5 lbs./cy fibers), 5-in. thick Cell 706 (8 lbs./cy), and 5-in. thick Cell 806 (11.66 lbs./cy) did not develop any considerable fatigue related crack.

5.5.1. Crack Percentage

Figure 5-13 shows the percentage of cracked slabs with respect to age (months) and ESAL for both lanes combined of Cells 506 through 806. Approximately, 12% of the slabs of Cell 506 cracked at 2.8 million ESALs; neither of the FRC cells did experience that many cracked slabs after the same number of ESALs. Figure 5-14 shows the percentage of cracked slabs only in the driving lanes. As much as 9% of the slabs in the driving lanes for Cell 506 cracked after 2.8 million ESALs. Whereas, for Cell 706 and 806, zero percent slabs cracked.

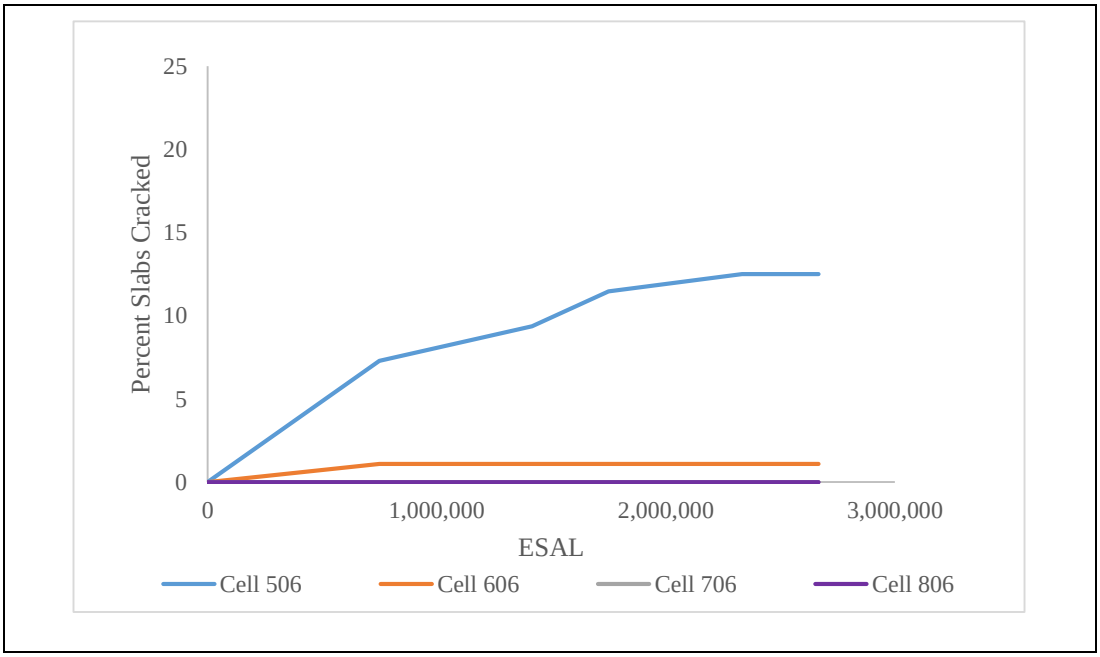

Figure 5-13: Percentage Crack vs. ESAL for both lanes 506,606,706, and 806.

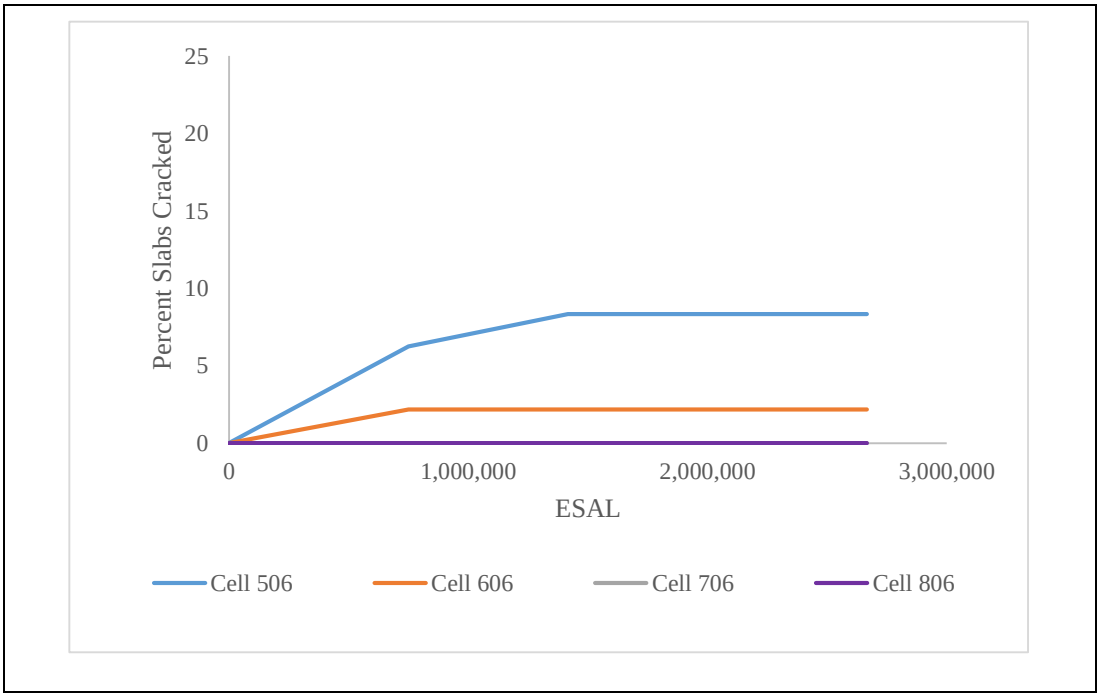

Figure 5-14: Percentage Crack vs. ESAL for the driving Lane of Cells 506, 606, 706, and 806.

Even after 2.8 million ESALs, the FRC test cells at the MnROAD test facility did not undergo a lot of cracks. A finite element study may be required to understand the influence of macro-fibers on fatigue life of thin FRC pavements in more detail.

5.6. Summary

This chapter included the two major distresses (joint faulting and fatigue cracking) as measured for the test cells, their analysis results and discussion. At first, the joint faulting results showed that it increased in all the test cells with respect to time and ESALs. Such plots also indicated that the non-FRC Cell 506, consistently had higher faulting at a given date or ESAL when compared to the FRC cells and Cell 806 having the highest fiber dosage reported the least faulting throughout. At this stage, a faulting prediction equation was proposed for the test cells at a given fiber type/material. The predicted faulting was expressed as a function of traffic loading, slab thickness, residual strength of the concrete and combined modulus of subgrade reaction. The equation was then validated with available field faulting data. After that, a relationship between faulting index and pavement roughness (IRI) was established and it was found that faulting in thin concrete pavement slabs significantly influenced the pavement roughness. A higher fiber dosage was helpful to keep the faulting values less which in turn kept the IRI values within limits. The crack survey data indicated that non-fiber Cell 506 developed the most number of cracks and spalling whereas Cells 706, 806 having higher fiber dosage did not generate any cracks or spalling. The very few number of cracks in the test cells did not help in developing any conclusive results and a finite element study was recommended to identify the effects of fiber reinforcement on thin concrete test cells.

6. Recommendations and Conclusions

The objectives of this study were to identify the contribution of synthetic macro-fibers in improving joint performance and mitigating distresses like transverse joint faulting and fatigue cracking in thin concrete pavements. The pavement roughness was also studied for the test cells under consideration. The field section selected for this study was a part of MnROAD test facility on I-94 Westbound. The test cells were equipped with different pavement sensors among which, the vibrating wire sensor was included in the scope of this study. Alongside sensor data, FWD test, transverse joint faulting and distress survey data were also reported and analyzed in this thesis work. The different conclusions that can be drawn from this study is presented in the following:

- Joint performance is significantly affected by the inclusion of fibers. More fiber dosage resulted in higher LTE, lower differential displacement, and lower loaded-side displacement. Cell 806 with 11.66 lbs./cy fiber dosage (highest) performed best among all the test cells. Cell 506 with no fiber (control cell) indicated poor joint performance compared to the fiber reinforced cells.
- Greater fiber content in thin test cells showed lesser probability of voids underneath the thin test cells.
- The magnitude and variation in environmental strain was also less in the fiber reinforced test cells. Cell 806 with highest fiber dosage resulted in higher negative strains at the top whereas Cell 506 with no fibers showed maximum environmental strain at the bottom of the slabs.
- The variation in slab curvature resulting due to daily and seasonal variation of environmental strain at the top and bottom of the slabs were more in Cell 506 (0 lbs./cy fiber) as compared to Cell 806 (11.66 lbs./cy fiber). Moreover, a plot between slab curvature-LTE indicated that a higher fiber dosage resulted in less variation in slab curvature which in turn kept the LTE high.
- Transverse joint faulting results showed that joint faulting increased with the increase in age and ESALs. Cell 506 with no fibers showed the highest faulting value throughout whereas Cell 806 with highest fibers showed the lowest faulting value among the test cells.
- A comparison between faulting index per mile and pavement roughness parameter (IRI), indicated that higher fiber dosage helps in keeping the IRI value within limits

for a longer duration. There is a considerable relationship between faulting index and pavement roughness parameter (IRI). Higher faulting values in thin concrete cells resulted in higher pavement roughness.

- Distress data collected during the three years of study showed that there were very few cracks generated in the test cells. With the limited crack data, crack percentage comparison among all the test cells showed higher number of cracks in the Cell 506 (no fiber) and approximately no cracks in Cell 706 (8 lbs./cy) and 806 (11.66 lbs./cy).
- The crack analysis indicates that fatigue cracking may not be a dominant distress in the thin fiber reinforced test cells unlike transverse joint faulting.

Based on this thesis work following recommendations are made for future research work:

- The present study only considers three different dosage of one particular type of macro-fiber. Similar study should be conducted with different fiber types, texture or geometry in order to identify the best suited macro-fiber for the purpose.
- Distress survey data indicated limited number of cracks in the test cells. A finite element study may be beneficial in order to establish the effect of macro-fibers in mitigating fatigue cracking in thin fiber reinforced test cells.

Bibliography

AASHTO Guide for Design of Pavement Structures 1993, American Association of State Highway and Transportation Officials, Washington, D.C. 20001.

ACI 544.1R, (2009). *State-of-the-Art Report on Fiber Reinforced Concrete.* Farmington Hills, MI, American Concrete Institute.

ARA (2003). *Guide for Mechanistic-Empirical Design of New and Rehabilitated Pavement Structure: Appendix JJ Transverse Joint Faulting Model.* National Cooperative Highway Research Program, Transportation Research Board, Washington, DC.

Asbahan, R. E., & Vandenbossche, J. M. (2011). *Effects of temperature and moisture gradients on slab deformation for jointed plain concrete pavements.* Journal of Transportation Engineering, 137(8), 563-570.

ASTM International. (2012). *C1609/C1609M-12 Standard Test Method for Flexural Performance of Fiber-Reinforced Concrete (Using Beam With Third-Point Loading).* West Conshohocken, PA. doi: https://doi.org/10.1520/C1609_C1609M-12.

Barman, M. (2014). *Joint Performance Characterization of Bonded Whitetopping Overlays* (Doctoral dissertation, University of Pittsburgh), Pittsburgh, PA.

Barman, M., & Hansen, B. (2018). *Comparison of Performances of Structural Fibers and Development of a Specification for Using Them in Thin Concrete Overlays*. Minnesota Dept. of Transportation, St. Paul, MN.

Barman, M. Crick. C., Roy, S., Tiwai, A., and Burnham, T. (2020) *Performance Benefits of Fiber-reinforced Thin Concrete Pavement and Overlays. Task-2: Second Year Annual Cell Performance Report (2018-2019),* MnDOT, St. Paul. MN.

Barman, M. Tiwari, A., Roy, S., and Burnham, T. (2021) *Performance Benefits of Fiber-reinforced Thin Concrete Pavement and Overlays. Task-3 & 5: Analysis to determine contribution of fibers in reducing panel fatigue cracking*, MnDOT, St. Paul. MN.

Birely, A. C., Park, P., McMahon, J. A., Shi, X., & Rew, Y. (2018). *Fiber reinforced concrete for improved performance of transportation infrastructure* (No. FHWA/AZ-18-705). Arizona Dept. of Transportation, Littlefield, AZ.

Burnham, T., Worel, B., & Izevbekhai, B. (2020). *Contribution of MnROAD Research to Improvements in Concrete Pavement Technology from 1994–2019.* Transportation Research Record, 2674(7), 56–66. https://doi.org/10.1177/0361198120920874

Cerventes, V. and Roesler, J. (2009). *Performance of Concrete Pavements with Optimized Slab Geometry. Final Report ICT-09-053.* Urbana, IL. 61801.

Chorzepa, M.G., Johnson, C., Kim, S.S. and Durham, S. (2019). *Forensic Investigation of Distresses Found in Jointed Plain Concrete Pavements.* Journal of Transportation Engineering, Part B: Pavements, 145(1), ASCE.

Colley, B. E., & Humphrey, H. A. (1967). *Aggregate interlock at joints in concrete pavements.* Highway Research Record 189, pp 1-18, Highway Research Board, Washington D.C.

Delatte, N. (2008). *Concrete Pavement Design, Construction, and Performance.* Taylor & Francis. 2 Park Square, Milton Park, Abingdon, Oxon OX14 4RN.

Evangelista, F., Roesler, J., & Paulino, G. (2009). *Numerical Simulations of Fracture Resistance of Functionally Graded Concrete Materials.* Transportation Research Record, 2113(1), pp. 122–131. https://doi.org/10.3141/2113-15

Fiber Reinforced Concrete Pavements. (2003). *R&T Update Concrete Pavement Research & Technology.* Number 4.10 November 2003. American Concrete Pavement Association. Skokie, IL 60077.

Harrington, D. S. (2008). *Guide to concrete overlays for resurfacing & rehabilitating existing pavements*: seminar. Iowa Department of Transportation. Ames, IA.

Harrington, D., Fick, G., & Taylor, P. (2014). *Preservation and Rehabilitation of Urban Concrete Pavements Using Thin Concrete Overlays: Solutions for Joint Deterioration in Cold Weather States* (No. InTrans Project 09-361). Iowa State University, Ames, IA

Hoerner, T.E., M.I. Darter, L. Khazanovich, L. Titus-Glover, and K.L. Smith. (2000). *Improved Prediction Models for PCC Pavement Performance-Related Specifications*, Volume I: Final Report, Publication No. FHWA-RD-00-130, Federal Highway Administration. McLean, VA.

Janisch, D. (2015). *An overview of Mn/DOT's pavement condition rating procedures and indices.* Minnesota Department of Transportation, Saint Paul, MN.

Khazanovich, L., & Yu, H. T. (2001). *Modeling of jointed plain concrete pavement fatigue cracking in Pavespec 3.0.* Transportation research record, 1778(1), 33-42.

Khazanovich, L., Darter, M. I., & Yu, H. T. (2004). *Mechanistic-empirical model to predict transverse joint faulting.* Transportation Research Record, 1896(1), 34-45.

Lee, M.K. and Barr, B.I.G., 2004. *An overview of the fatigue behaviour of plain and fibre reinforced concrete*. Cement and Concrete Composites, *26(4),* pp.299-305.

Li, Z., Dufalla, N., Mu, F. and Vandenbossche, J.M. (2013). *Bonded concrete overlay of asphalt pavements mechanistic-empirical design guide (BCOA-ME)—Theory manual.* Univ. of Pittsburgh, Pittsburgh, PA.

Manual-MnDOT Pavement Design (2007), Chapter 5, Minnesota Department of Transportation, St. Paul, MN.

Miller, J. S., & Bellinger, W. Y. (2003). *Distress identification manual for the long-term pavement performance program* (No. FHWA-RD-03-031). United States. Federal Highway Administration. Office of Infrastructure Research and Development. McLean, VA.

MnDOT Pavement Distress Identification Manual. (2011). Minnesota Department of Transportation, St. Paul, MN. https://www.dot.state.mn.us/materials/manuals/pvmtmgmt/Distress_Manual.pdf

Owusu-Antwi, E.B., L. Titus-Glover, L. Khazanovich, and J.R. Roesler. (1997) *Development and Calibration of Mechanistic-Empirical Distress Models for Cost Allocation.* Final Report, Federal Highway Administration, Washington D.C.

Papagiannakis, A., & Masad, E. (2008). *Pavement Design and Materials.* JohnWiley&Sons. Hoboken, New Jersey.

Peterson, E., (2011). *Traffic & ESAL summary for the MnROAD mainline (July 1994- June 2011).* Minnesota Department of Transportation. St. Paul, MN. https://www.dot.state.mn.us/mnroad/files/mainline-traffic-summary.pdf.

Roesler, J.R., Bordelon, A.C., Ioannides, A., Beyer, M. and Wang, D. (2008). *Design and concrete material requirements for ultra-thin whitetopping*. ISSN: 0197-9191. Illinois Center for Transportation. Rantoul, IL.

Roesler, J., Bordelon, A., Brand, A. S., & Amirkhanian, A. (2019). *Fiber-Reinforced Concrete for Pavement Overlays: Technical Overview*. *Final Report*. Iowa State University, Ames, IA.

Sachs, S., Vandenbossche, J.M., Alland, K., DeSantis, J., and Khazanovich, L. (2016). *Effects of Interlayer Systems on Reflective Cracking in Unbonded Overlays of Existing Concrete Pavements.* Transportation Research Record: Journal of the Transportation Research Board, No. 2591, pp. 33–41. Transportation Research Board, Washington, D.C.

Simpson, A.L., J.B. Rauhut, P.R. Jordahl, E. Owusu-Antwi, M.I. Darter, and R. Ahmad. (1994). *Early Analysis of LTPP General Pavement Studies Data, Volume 3: Sensitivity Analyses for Selected Pavement Distresses, Report SHRP-P-393,* Strategic Highway Research Program, National Research Council, Washington D.C.

Smith, K. D., H. T. Yu, and D. G. Peshkin (2002). *Portland cement Concrete Overlays: State of the Technology Synthesis*. Report No. FHWA-IF-02-045. Federal Highway Administration, U.S. Department of Transportation, Washington D.C.

Stone, J. (1991). *Georgia Digital Faultmeter*, Report No. FHWA-GA-91-SP9010, Federal Highway Administration, Washington, DC.

Thin and Ultra-thin Whitetoping. NCHRP Synthesis 338. (2004). Transportation Research Board. The National Academies Press. Washington, D.C.

Titus-Glover, L., E. Owusu-Antwi, and M I. Darter. *Design and Construction of PCC Pavements, Volume III: Improved PCC Performance.* Report No. FHWA-RD-98-113, Federal Highway Administration, Washington, D.C.

Tsai, Y. J. (2016). *Enhancing GDOT's Jointed Plain Concrete Pavement (JPCP) Rehabilitation Program Using Emerging 3D Sensing Technology and Historical Concrete Condition Survey Data* (No. FHWA-GA-17-1319). Georgia. Department of Transportation. Office of Performance-Based Management & Research. Atlanta, GA.

Tsai, Y. J., & Wu, Y. C. (2019). *Developing a Comprehensive Pavement Condition Evaluation System for Rigid Pavements in Georgia* (No. FHWA-GA-19-1502). Georgia. Dept. of Transportation. Atlanta, GA.

Van Deusen, D. A., Burnham, T. R., Dai, S., Geib, J., Hanson, C., Izevbekhai, B. I., & Worel, B. (2018). *Report on 2017 MnROAD Construction Activities* (No. MN/RC 2018-16). Minnesota. Dept. of Transportation. Research Services & Library. St. Paul, MN.

Vandenbossche, J. M. (2007). *Effects of slab temperature profiles on use of falling weight deflectometer data to monitor joint performance and detect voids.* Transportation research record, 2005(1), 75-85.

Vandenbossche, J.M. and Barman, M., (2010). *Bonded whitetopping overlay design considerations for prevention of reflection cracking, joint sealing, and the use of dowel bars.* Transportation research record, 2155(1), pp.3-11.

Vandenbossche, J. M., Barman, M., Li, Z., & Adams, T. S. (2012). *Development of Innovative Techniques for the Instrumentation of Composite and Wet on Wet Pavement Sections at MnROAD.* In 10th International Conference on Concrete Pavements International Society for Concrete Pavements, Holcim (Canada) Transports Quebec.

Weinmann, T. L., Lewis, A. E., & Tayabji, S. D. (2004). *Pavement sensors used at accelerated pavement test facilities.* In Proceedings of the second international conference on accelerated pavement testing. Minneapolis, MN. pp. 1–30.

Wells, S. A., Phillips, B. M., & Vandenbossche, J. M. (2006). *Quantifying built-in construction gradients and early-age slab deformation caused by environmental loads in a jointed plain concrete pavement.* International Journal of Pavement Engineering, 7(4), 275-289.

Wu, C.L., J.W. Mack, P.A. Okamoto, and R.G. Packard. (1993). *Prediction of Faulting of Joints in Concrete Pavements*, Proceedings, Fifth International Conference on Concrete Pavement Design and Rehabilitation, Vol. 2., Purdue University, West Lafayette, IN.

Yu, H.T., M.I. Darter, K.D. Smith, J. Jiang and L. Khazanovich. (1996). *Performance of Concrete Pavements Volume III - Improving Concrete Pavement Performance.* Final

Report, Contract DTFH61-91-C-00053, Federal Highway Administration, McLean, VA.

Appendix A: Sensor Layouts - MnROAD

(Courtesy: MnDOT)

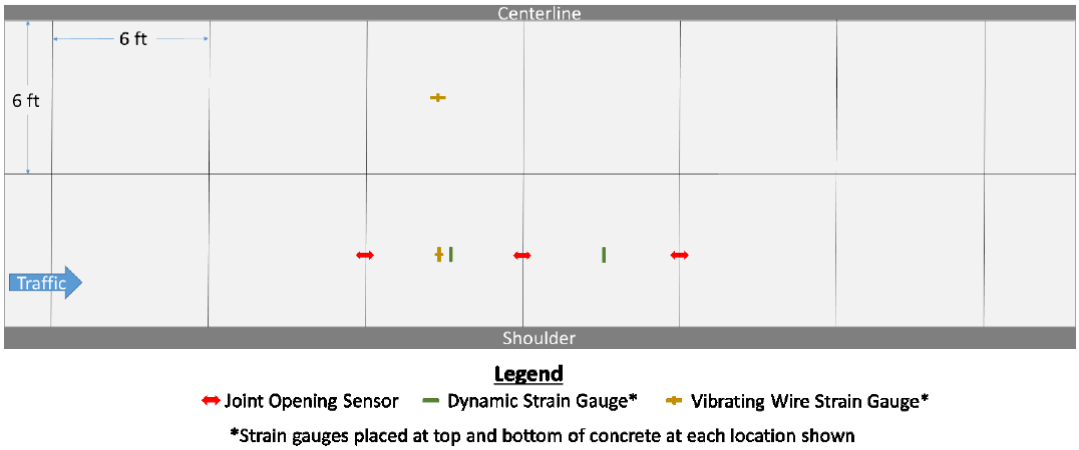

Figure A- 1: Sensor plan for Cell 506.

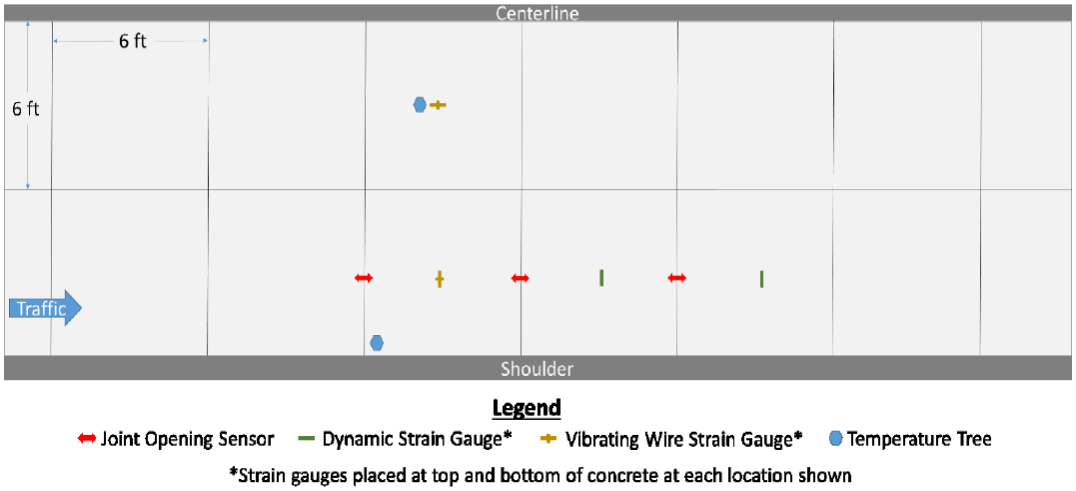

Figure A- 2: Sensor plan for Cell 606.

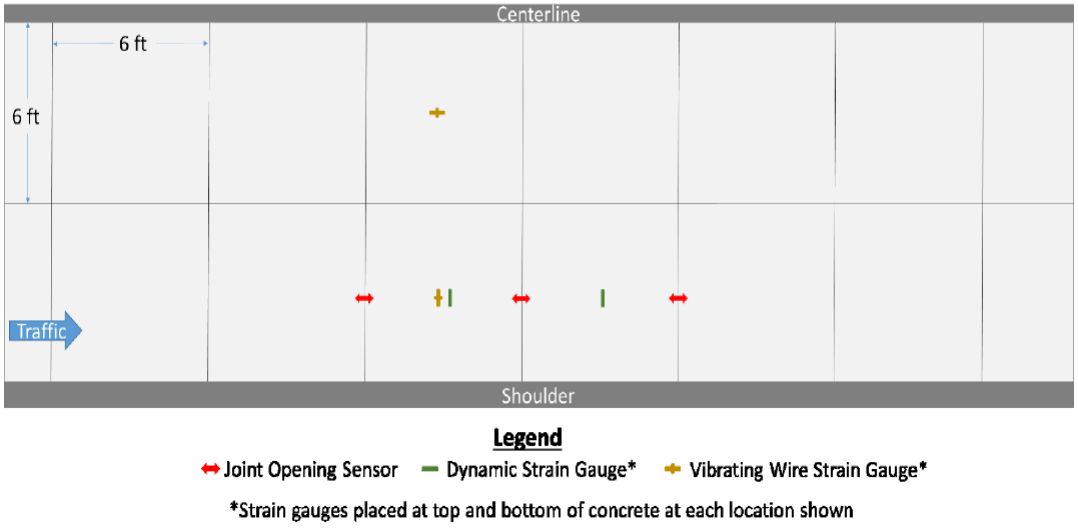

Figure A- 3: Sensor plan for Cell 706.

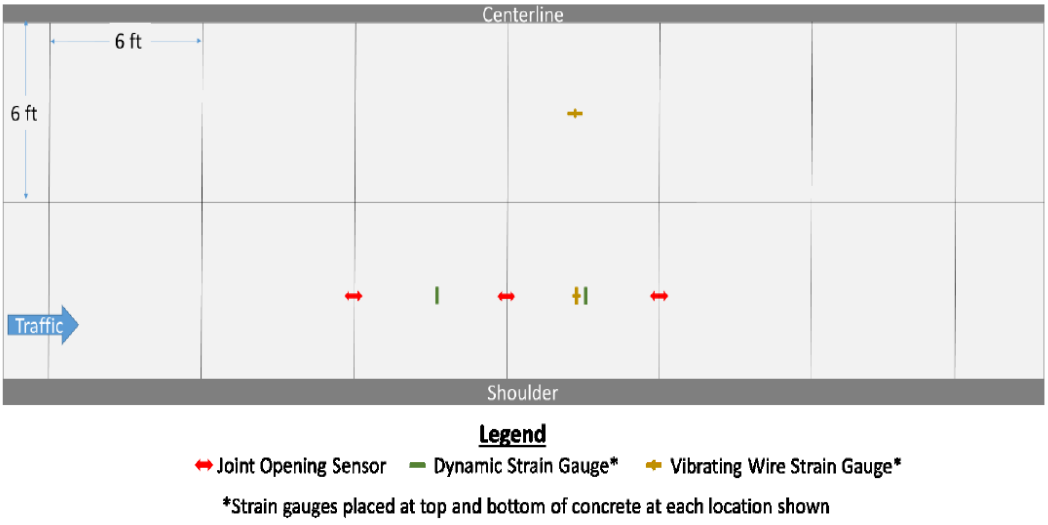

Figure A- 4: Sensor plan for Cell 806.

Appendix B: FWD test plans – MnROAD

(Courtesy: MnDOT)

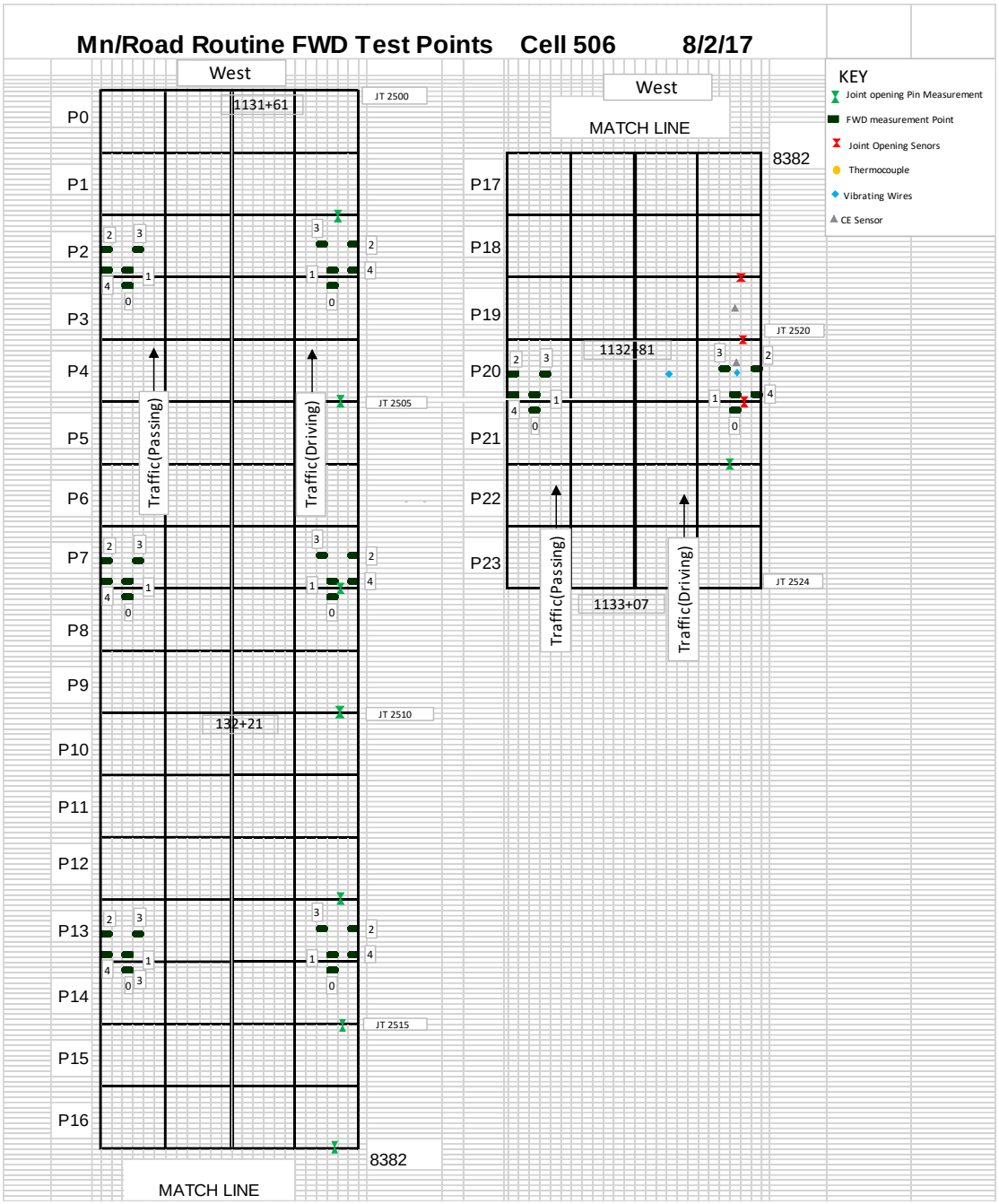

Figure B- 1: FWD test plan for Cell 506.

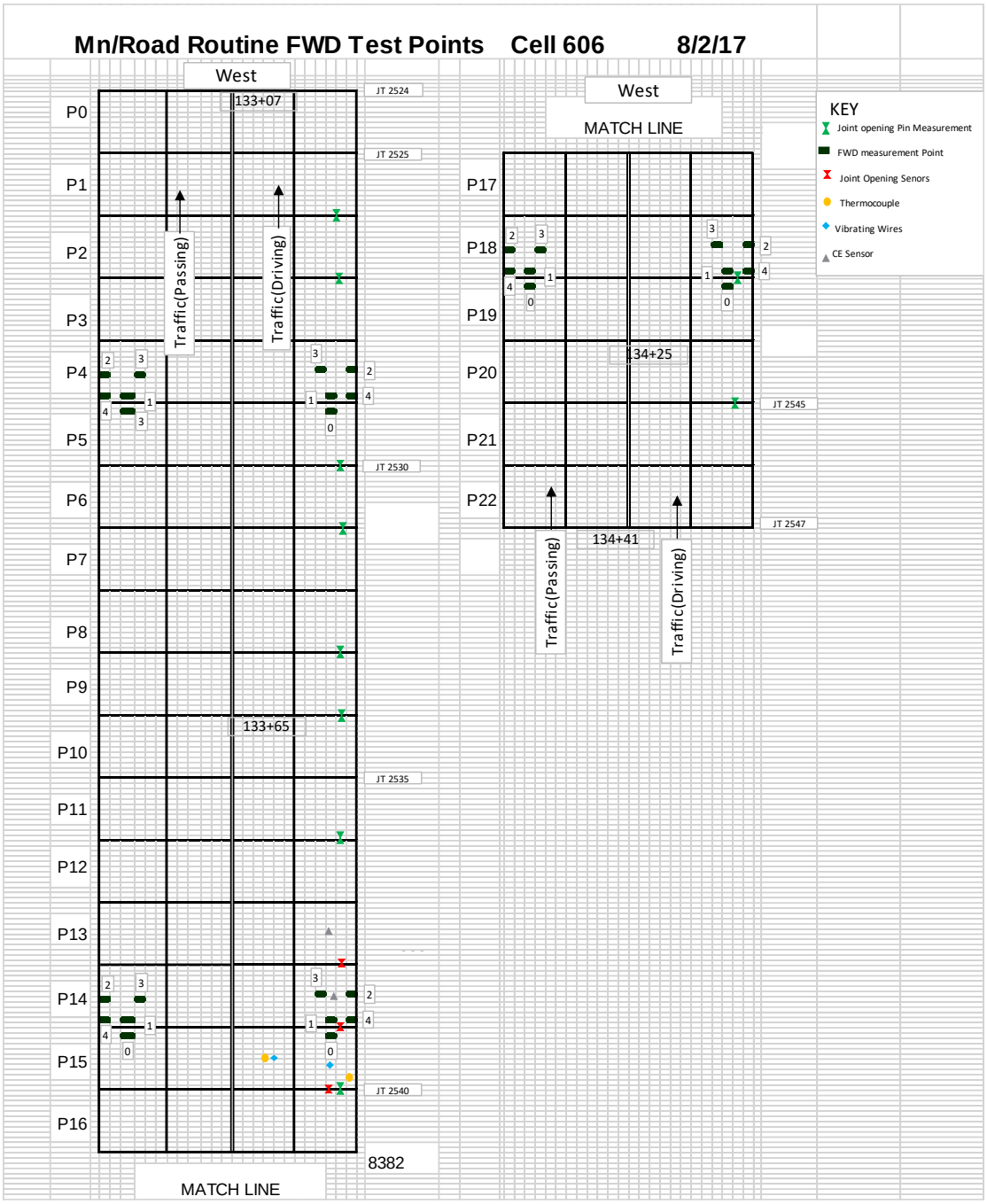

Figure B- 2: FWD test plan for Cell 606.

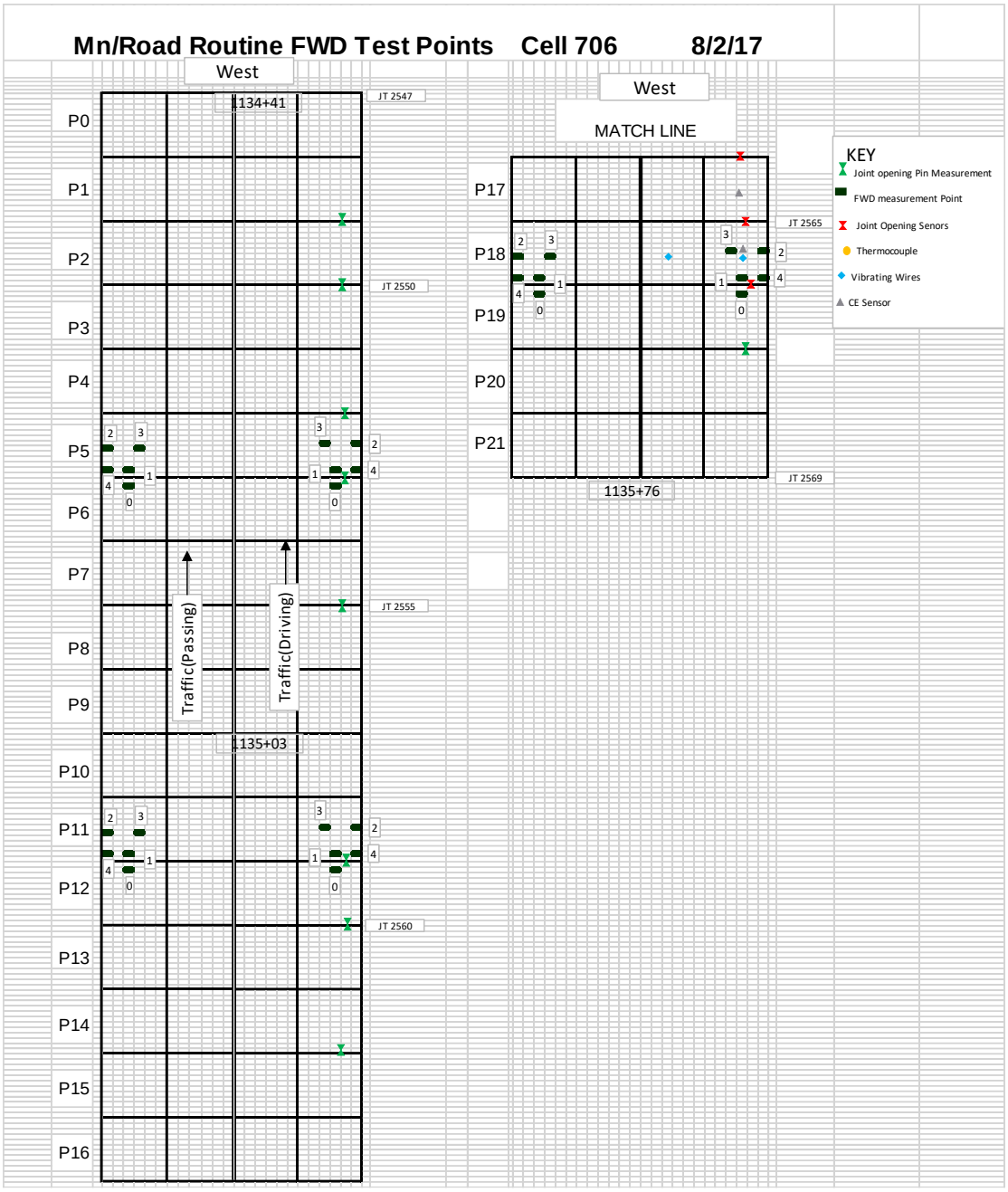

Figure B- 3: FWD test plan for Cell 706.

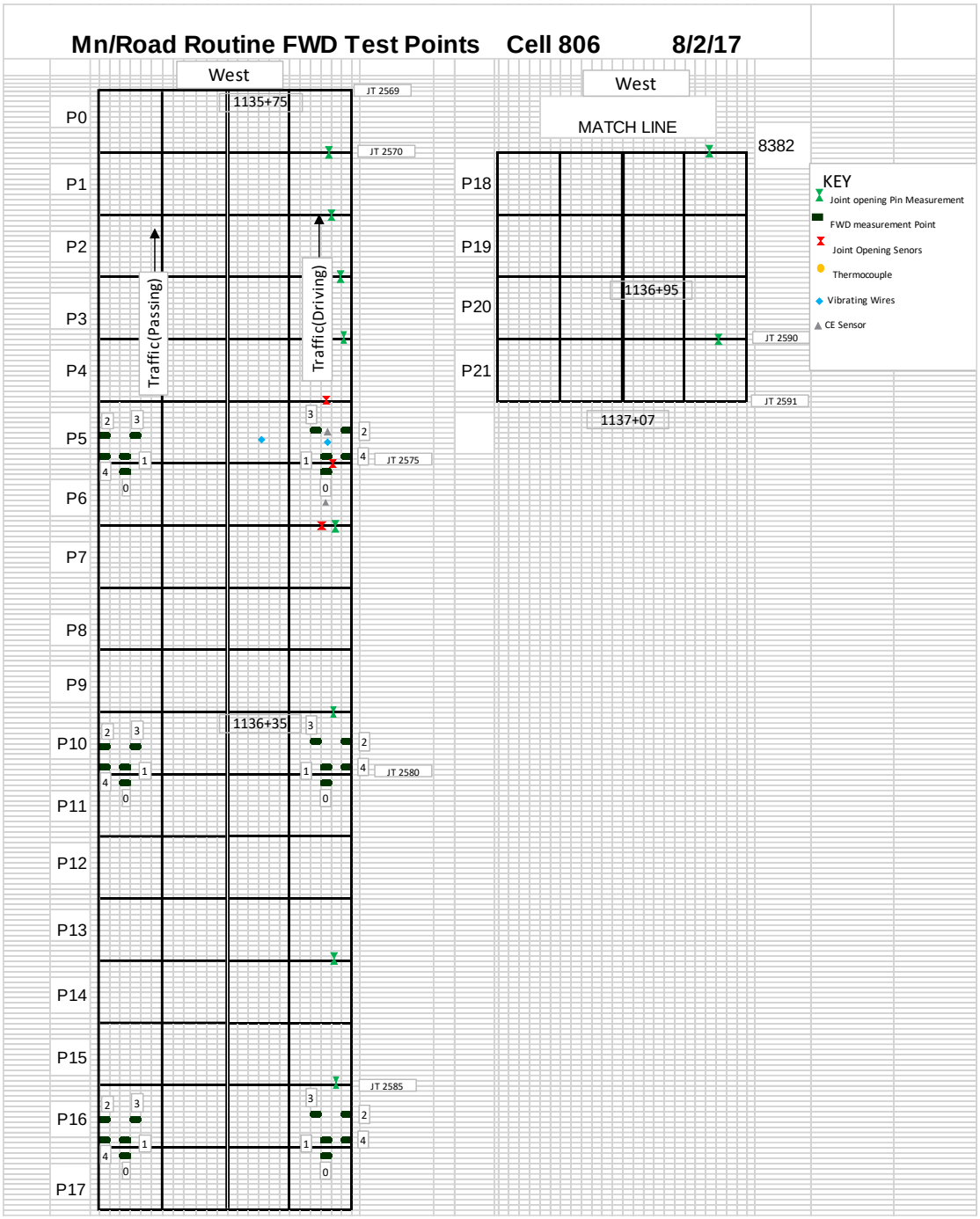

Figure B- 4: FWD test plan for Cell 806.